NASA Contractor Report 145366

SHOCK CAPTURING FINITE-DIFFERENCE AND CHARACTERISTIC REFERENCE PLANE TECHNIQUES FOR THE PREDICTION OF THREE-DIMENSIONAL NOZZLE-EXHAUST FLOWFIELDS

(NASA-CR-145366) SHOCK CAPTURING FINITE-DIFFERENCE AND CHARACTERISTIC REFERENCE PLANE TECHNIQUES FOR THE PREDICTION OF THREE-DIMENSIONAL NOZZLE-EXHAUST (General Applied Science N78-25355

Unclas
G3/34 21560

S. Dash and P. Del Guidice

GENERAL APPLIED SCIENCE LABORATORIES INC.
Westbury, NY 11590

NASA Contract NAS1-12726

May 1978

National Aeronautics and Space Administration

Langley Research Center
Hampton, Virginia 23665

PREFACE

This final report summarizes the work completed under Contract No. NAS1-12726 towards the development of models and associated computer codes for the analysis of three-dimensional supersonic nozzle-exhaust flowfields. The contract was monitored by Mr. Manuel Salas of NASA Langley who provided comparison flowfield results and constructive suggestions during the course of this effort. The authors additionally acknowledge the benefit of many fruitful discussions with the late Dr. Antonio Ferri and the programming assistance provided by Mr. Paul Kalben in the development of computer codes BIGMAC and CHAR3D.

TABLE OF CONTENTS

LIST OF FIGURES

LIST OF FIGURES (Continued)

LIST OF SYMBOLS

a_e	equilibrium sound speed, ft/sec (m/sec)
C_v	specific heat at constant volume
E(k)	conservation variables (k=1 to 6) defined in text
F(k)	conservation variables (k-1 to 6) defined in text
G(k)	conservation variables (k=1 to 6) defined in text
H(k)	conservation variables (k=1 to 6) defined in text
H	stagnation enthalpy, $ft^2/sec^2 (m^2/sec^2)$
h	static enthalpy, $ft^2/sec^2 (m^2/sec^2)$
h_1, h_2, h_3	metric coefficients, defined in text
I	index of data point in reference plane
J	index of reference plane
K	index of marching step
M	Mach number in reference plane, q/a_e
$\hat{n}$	unit normal to surface
P	pressure, lb/ft^2 (N/m^2)
q	magnitude of velocity in reference plane, ft/sec (m/sec)
S	entropy, $ft^2/sec^2\text{-}^oR$ $(m^2/sec^2\text{-}k)$
T	temperature, ^oR (K)
$\bar{V}$	flow velocity vector
u	velocity component in marching direction in reference plane, ft/sec (m/sec)
v	velocity component normal to reference plane, ft/sec (m/sec)
w	velocity component in reference plane normal to marching direction, ft/sec (m/sec)
x,y,z	Cartesian coordindate
r,θ,z	line source coordinates
x,θ,r	cylindrical coordinates

ORIGINAL PAGE IS
OF POOR QUALITY

I. INTRODUCTION

This report summarizes work accomplished under Contract No. NAS1-12726 towards the development of computational procedures and associated numerical codes for three-dimensional nozzle-exhaust flow fields. The flow fields considered are those associated with airbreathing hypersonic aircraft which require a high degree of engine/airframe integration in order to achieve optimized performance. The exhaust flow, due to physical area limitations, is generally underexpanded at the nozzle exit; the vehicle afterbody undersurface is used to provide additional expansion to obtain maximum propulsive efficiency. This results in a three-dimensional nozzle flow, initialized at the combustor exit, whose boundaries are internally defined by the undersurface, cowling and walls separating individual modules, and externally, by the undersurface and slipstream separating the exhaust flow and external stream. A typical exhaust nozzle is depicted in Figure (1), characterized by multiple rectangular nozzle modules.

The numerical models developed in this analysis address the following characteristic features of these exhaust flows:

(1) The flow properties at the combustor exit are highly nonuniform. Burning and mixing in the combustor yield regions of highly varying composition, temperature, and stagnation properties. In addition, shock waves are produced in the vicinity of the injectors. Although the strength of these waves decays rapidly as they propagate through the burner, they are generally present at the burner exit and must be accounted for.

(2) The exhaust gas mixture consists of hydrogen-air combustion products and significiant burning may still occur in the initial regions of nozzle expansion.

(3) The flow field geometry is quite complex. The engine modules consist of multiple surfaces with sharp interior corners, and flow fences, to contain the external exhaust flow, may be present.

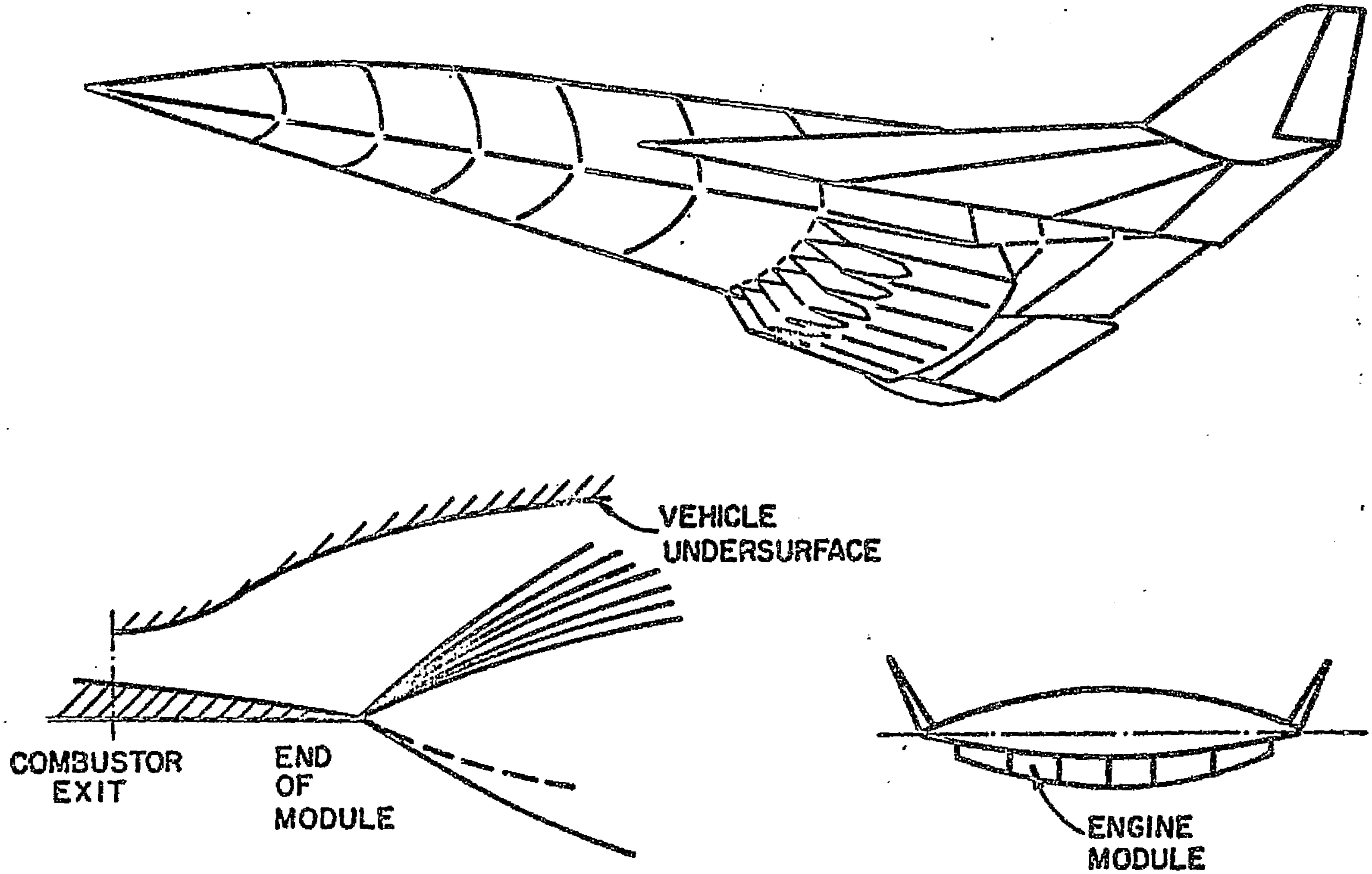

Figure 1.- Hypersonic research airplane.

(4) The interior nozzle flow field is dominated by complex wave interactions with waves generated and reflected off multiple surfaces. In addition, sharp interior corner regions must be accounted for.

(5) The nozzle exhaust flow interacts with the nonuniform vehicle external flow field. This complex interaction for underexpanded exhaust flows results in an expansion system propagating toward the vehicle undersurface from the cowl trailing edge and a spanwise expansion generated by the sidewall interaction. An underexpansion shock propagates outward into the nonuniform vehicle external flow, and the exhaust and external flow are separated by a plume boundary. In addition, pressure and flow deflection mismatch between adjacent modules may occur, resulting in a spanwise multiple shock system.

To accommodate the varied,complex geometric configurations entailed in this analysis, a reference plane approach has been utilized, with respect to several coordinate systems. This approach involves the definition of a reference plane system in which the three-dimensional volume under consideration is spanned by an appropriately selected series of planes which intersect the boundaries of the considered volume. The equations of motion within the reference planes are expressed in a quasi-streamline coordinate system, where quasi-streamlines are the projections of the actual stream surfaces onto these reference planes. Such a system accommodates the calculation of highly rotational, variable composition flow fields by minimizing streamline interpolation procedures which can produce significant errors, as discussed by Sedney in Reference (1).

Reference plane systems in cartesian, line source and cylindrical coordinates are illustrated in Figures (2), (3) and (4) respectively. The configuration of the reference planes is chosen to best accommodate the overall flow field geometry by having primary flow variations occur within the reference planes. A more complex flow field situation is depicted in Figure (5) for the flow downstream of the cowl exit. For this calculation, a combination of several reference plane systems is employed and provisions are included in the numerical codes for automatic switching from one system to another as the

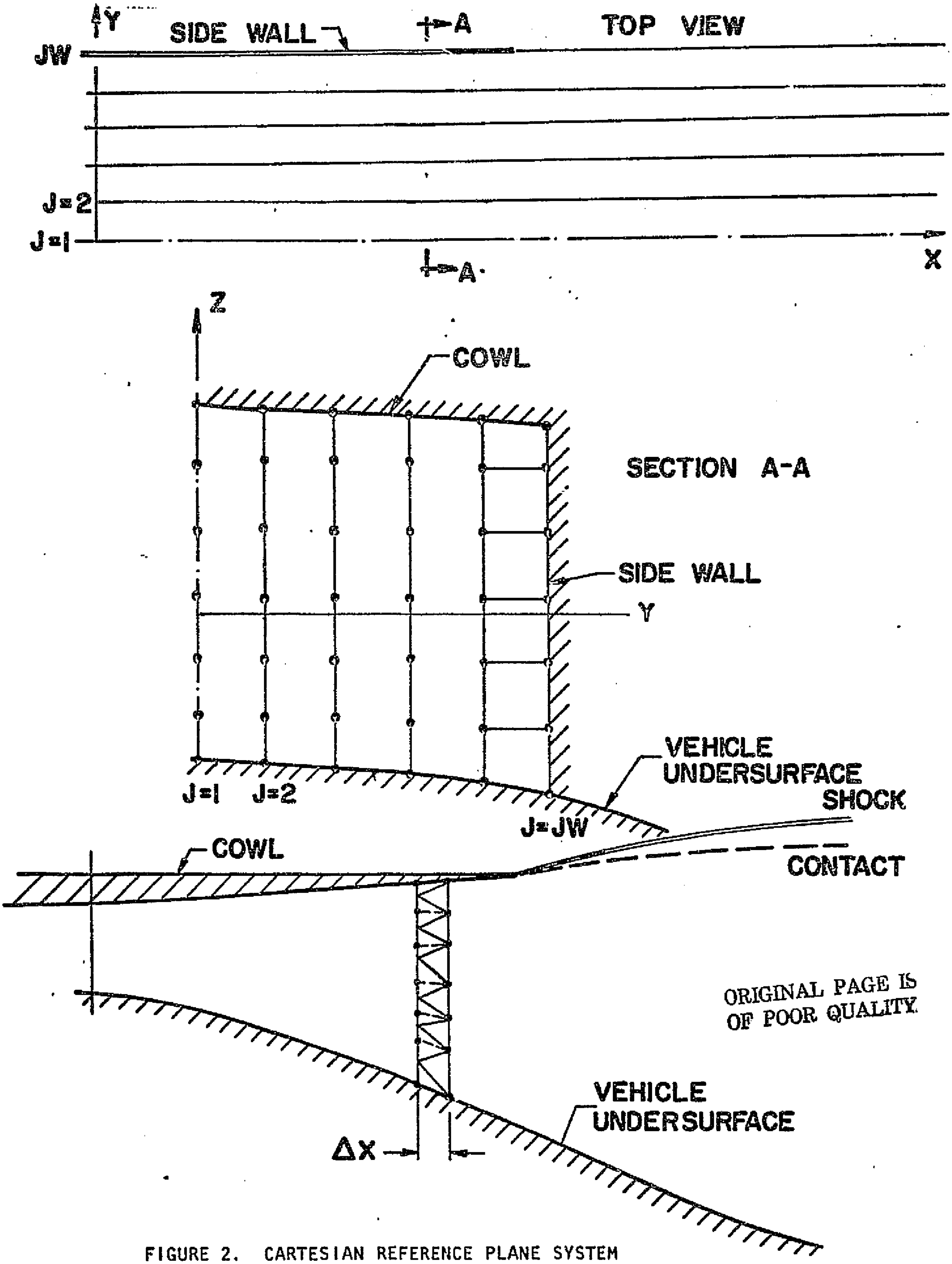

ORIGINAL PAGE IS
OF POOR QUALITY

FIGURE 2. CARTESIAN REFERENCE PLANE SYSTEM

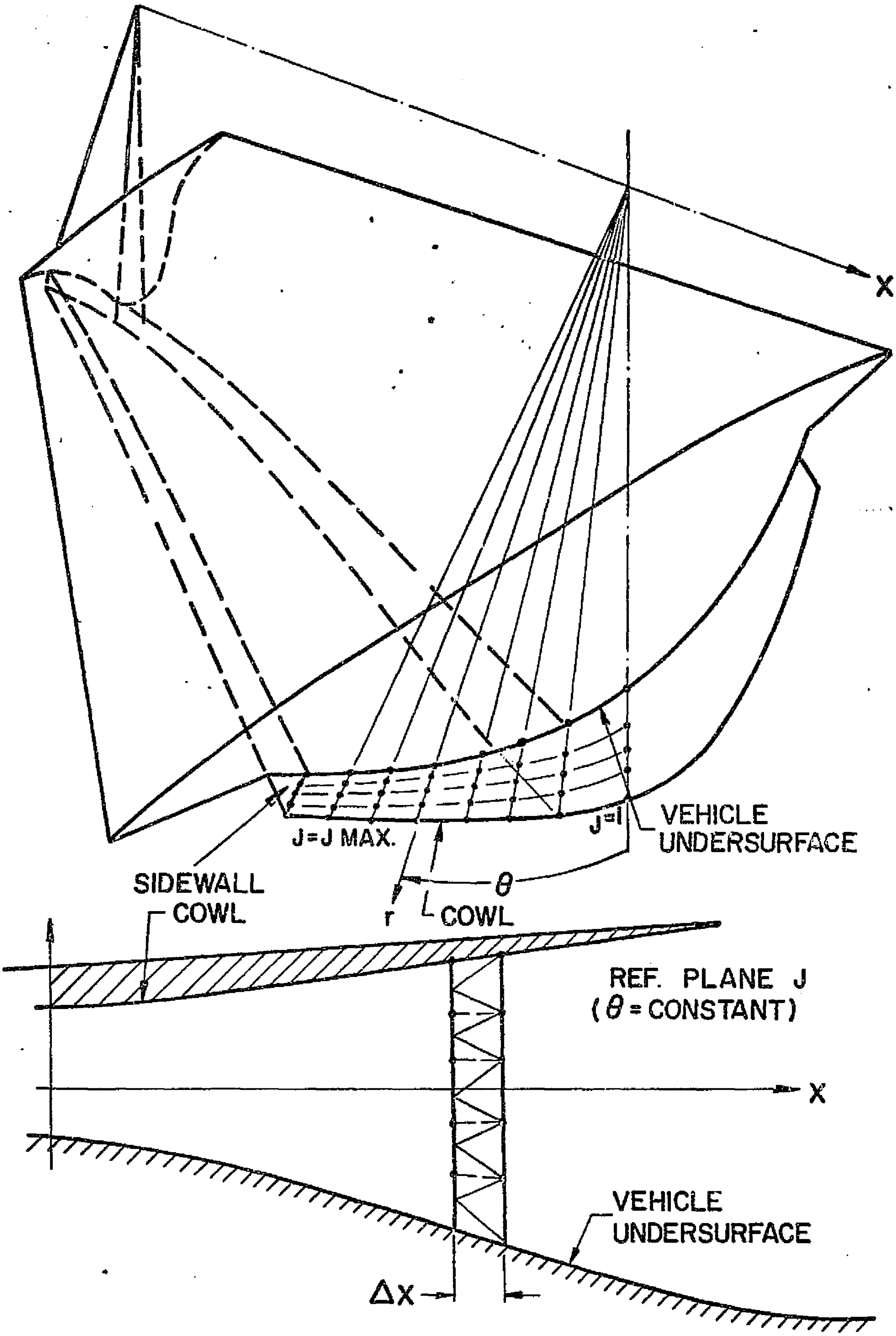

FIGURE 3. CYLINDRICAL REFERENCE PLANE SYSTEM

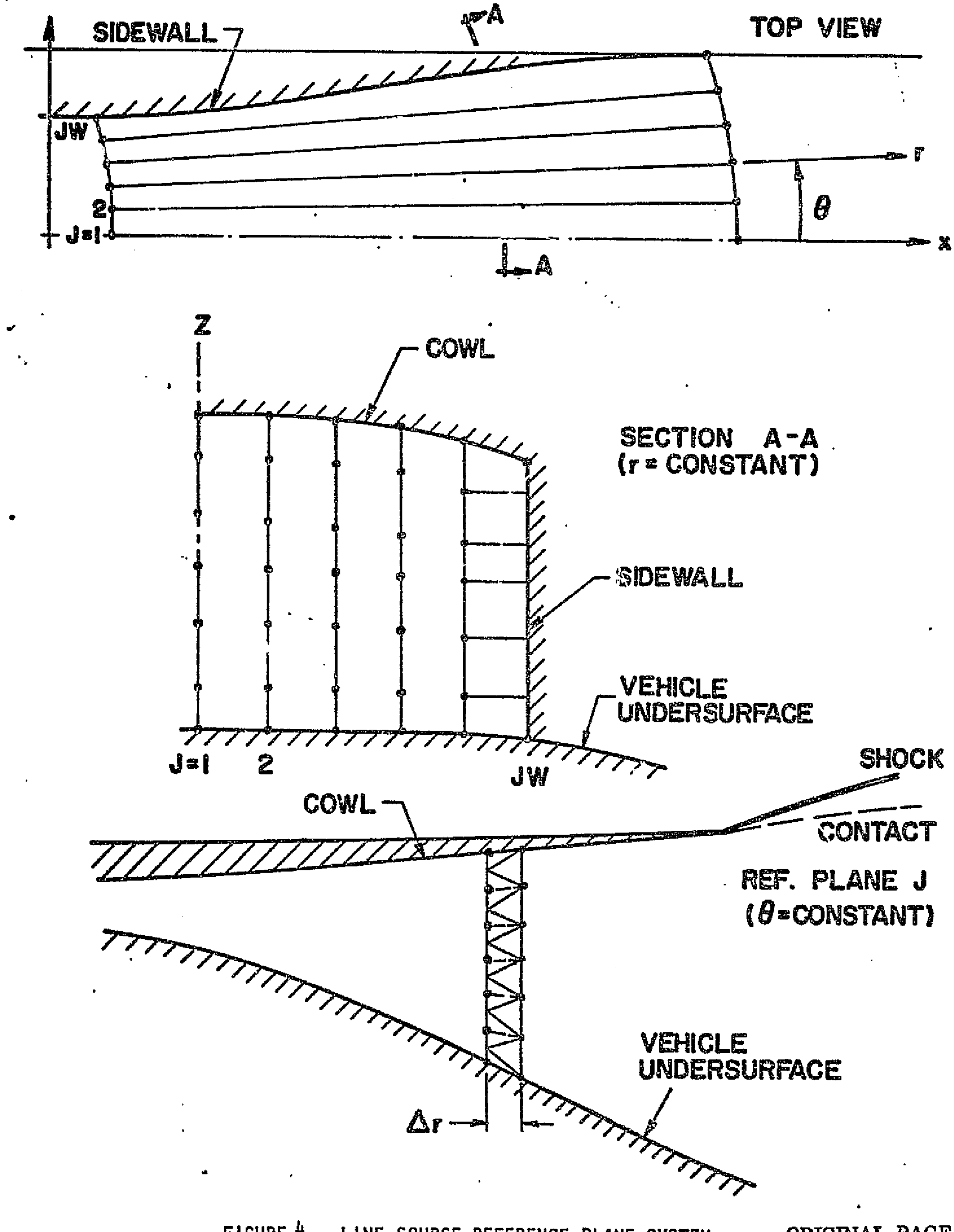

FIGURE 4. LINE SOURCE REFERENCE PLANE SYSTEM

ORIGINAL PAGE IS
OF POOR QUALITY

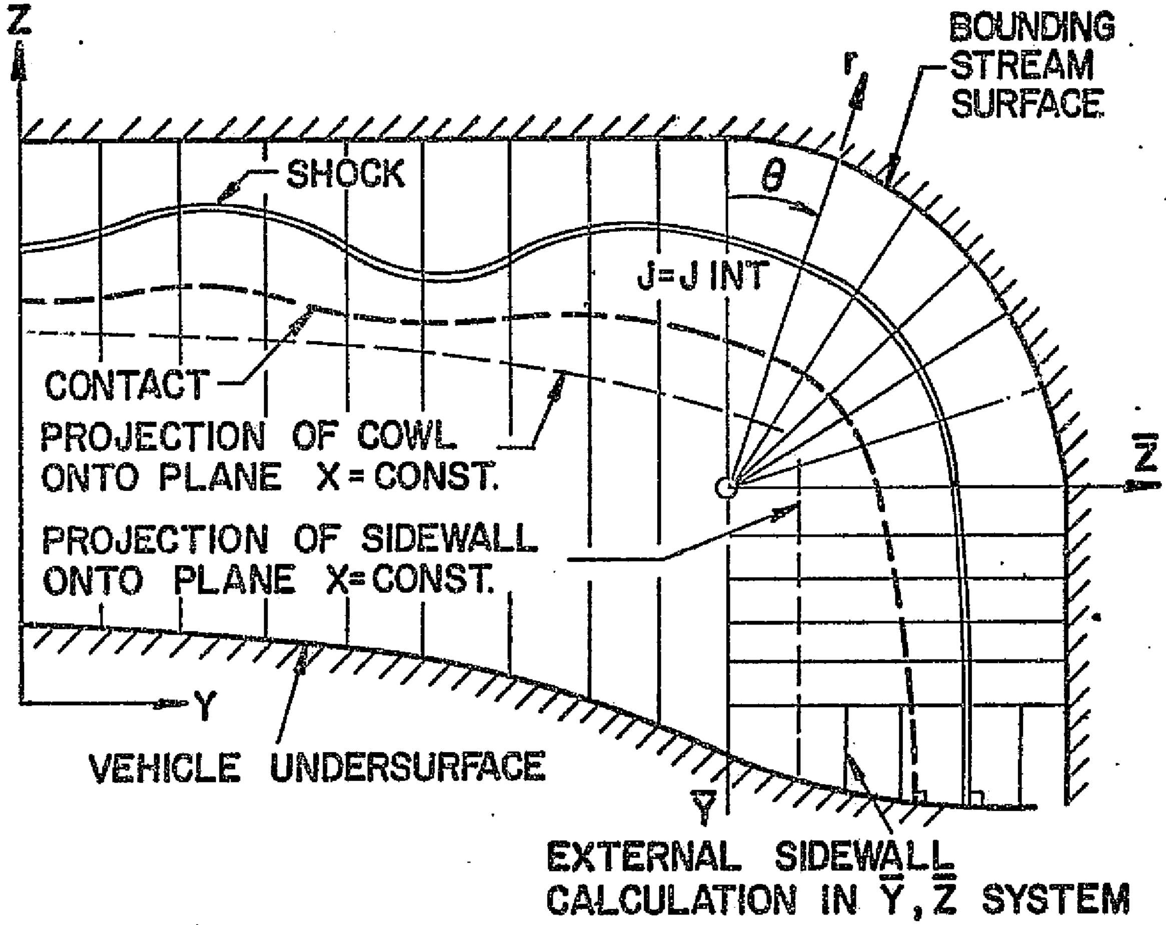

FIGURE 5. REFERENCE PLANE SYSTEM FOR EXHAUST/EXTERNAL FLOW

character of the boundary surfaces changes. The reference plane system also caters to the usage of reference plane characteristics at all boundary points. This approach is generally recognized as the most accurate boundary calculational procedure (Reference 2). However, it proves cumbersome when employed in conjunction with nonreference plane networks due to the complex interpolation procedures then required.

The reference plane characteristic technique has been widely used for the calculation of three-dimensional supersonic flow fields, and the authors had previously developed a program employing this technique for the calculation of nozzle exhaust flow fields (References 3 and 4), which is in current usage at NASA Langley Research Center (References 5, 6 and 7). That program, as well as most reference plane characteristic (refchar) codes in common usage (References 8 and 9), employs an inverse scheme wherein interpolations are performed to obtain data at the intersection of the quasi-characteristics with a noncharacteristic initial data surface. Comparisons of such refchar codes with shock capturing finite difference codes (Reference 10) have led to the general conclusion that difference codes are better able to analyze complex flow fields with multiple secondary shocks. From experience gained with the authors' original refchar code, it was felt that the inability to successfully analyze such flow fields was primarily due to the inverse interpolation procedures employed. Such procedures tend to ignore the presence of weak waves by allowing the quasi-characteristic lines to arbitrarily cross each other. The numerical diffusion associated with these interpolations can become significant, particularly when the local Courant number (ratio of overall marching step to local maximum allowable marching step) is much less than one. The smearing of these weak waves is enhanced by resorting to higher order interpolations on the initial data line.

To treat complex multiwave flow fields and still retain the advantages that reference plane methods afford, two new numerical codes have been developed. Program CHAR3D is based upon a quasi-characteristic calculational procedure employing a novel wave preserving network, as compared to previous standard inverse networks. In addition, a nonisentropic pressure-density relation applied along streamlines, permits the estimation of shock entropy losses while, the usage of conservation variables in the construction of cross-flow derivatives has facilitated the analysis of flow fields containing cross stream discontinuities. Program BIGMAC is a reference plane finite difference code utilizing the described quasi-streamline grid within reference planes. Shock capturing capabilities are provided via the usage of conservation variables in conjunction with a one-sided difference algorithm.

While the numerical algorithms and logical procedures employed in CHAR3D and BIGMAC differ, both codes employ a newly developed geometry package (Reference 11) for a description of boundary contours, calculate boundary points by reference plane characteristic procedures, and incorporate the same thermodynamic fits for describing the hydrogen-air gas mixture in chemical equilibrium.

The governing flow field equations are presented in Section II while computational procedures for CHAR3D and BIGMAC are presented in Section III. Section IV contains a description of sample calculations performed with both these codes. Conclusions drawn from this study and recommended procedures in extending this analysis are presented in Section V. For completeness, a summary of the equilibrium curve fits are presented in Appendix I while a description of the geometry package is presented in Appendix II.

II. GOVERNING EQUATIONS

A. Characteristic Analysis (CHAR3D) - The equations governing the steady flow of an inviscid gas mixture in chemical equilibrium may be written:

Continuity

$$\nabla \cdot (\rho \bar{V}) = 0 \tag{1}$$

Momentum

$$\rho (\bar{V} \cdot \nabla) \bar{V} + \nabla P = 0 \tag{2}$$

Energy

$$\bar{V} \cdot \nabla H = 0 \tag{3}$$

Equivalence Ratio Constancy Along Streamlines

$$\bar{V} \cdot \nabla \Phi = 0 \tag{4}$$

This system is supplemented by the relation

$$\bar{V} \cdot \nabla S = 0 \tag{5}$$

expressing constancy of entropy along streamlines in continuous regions of the flow field. The equation of state may be written

$$\left(\frac{\partial P}{\partial \rho}\right)_S = \frac{\Gamma P}{\rho} = a^2 \tag{6}$$

where curve fits for the isentropic exponent Γ, from Reference (4),

$$\Gamma = f(h, P, \Phi) \tag{7}$$

are described in Appendix I. The continuity equation, employing Equations (5) and (6) may be written:

$$\bar{V} \cdot \nabla P + a^2 \rho \nabla \cdot \bar{V} = 0 \tag{8}$$

The scalar forms of the modified continuity equation (Equation 8) and the momentum equations (Equation 2) in general orthogonal coordinates are:

Modified Continuity

$$\rho a^2 \left(\frac{u_{x_1}}{h_1} + \frac{w_{x_3}}{h_3}\right) + \frac{u\, P_{x_1}}{h_1} + \frac{w\, P_{x_3}}{h_3} = \frac{-a^2}{h_1 h_2 h_3} \left[h_1 h_3 \left(\frac{v}{a^2} P_{x_2} + \rho v_{x_2}\right) + h_{2_{x_1}} h_3 \rho u + h_1 h_{2_{x_3}} \rho w\right] \tag{9}$$

x_1 Momentum

$$\frac{u}{h_1} u_{x_1} + \frac{w}{h_3} u_{x_3} + \frac{1}{\rho h_1} P_{x_1} = -\frac{v}{h_2} u_{x_2} + \frac{v^2}{h_1 h_2} h_{2_{x_1}} \tag{10}$$

x_2 Momentum

$$\frac{u}{h_1} v_{x_1} + \frac{w}{h_3} v_{x_3} + \frac{1}{\rho h_2} P_{x_2} = -\frac{v}{h_2} v_{x_2} - \frac{uv}{h_1 h_2} h_{2_{x_1}} - \frac{vw}{h_2 h_3} h_{2_{x_3}} \tag{11}$$

x_3 Momentum

$$\frac{u}{h_1} w_{x_1} + \frac{w}{h_3} w_{x_3} + \frac{1}{\rho h_3} P_{x_3} = -\frac{v}{h_2} w_{x_2} + \frac{v^2}{h_2 h_3} h_{2_{x_3}} \tag{12}$$

The identification of metric coefficients and coordinate directions for the three coordinate systems under consideration is provided below.

System	x_1	x_2	x_3	h_1	h_2	h_3
Cartesian	x	y	z	1	1	1
Cylindrical	x	θ	r	1	r	1
Line Source	r	θ	z	1	r	1

Note that $h_{2_{x_1}}$ is unity for the line source system and zero for other systems while $h_{2_{x_3}}$ is unity for the cylindrical system and zero for other systems.

ORIGINAL PAGE IS
OF POOR QUALITY

These terms will be replaced by the indices J_1 and J_2 where $J_1 = 1$ for the line source system and $J_2 = 1$ for the cylindrical system. Both indices are zero otherwise.

In writing Equations (9) - (12), the source terms and terms involving derivatives normal to the reference planes x_2 = constant have been put on the right-hand side. Then, the left-hand side of these equations corresponds to that of the two-dimensional system in the x_1, x_3 plane. Reference plane characteristic relations are readily obtained by algebraic manipulation of the modified continuity equation and the x_1 and x_3 momentum equations. These relations are listed below, where the velocity vector

$$\bar{V} = u\ \hat{i}_{x_1} + v\ \hat{i}_{x_2} + w\ \hat{i}_{x_3} \tag{13}$$

is expressed in terms of its magnitude in the reference plane, q, quasi-streamline angle, ϕ, and cross flow angle, ψ, employing the geometric relations

$$q = (u^2 + w^2)^{\frac{1}{2}} \tag{14a}$$

$$\phi = \tan^{-1} (w/u) \tag{14b}$$

$$\psi = \tan^{-1} (v/q) \tag{14c}$$

as depicted in Figures (6), (7) and (8). Along the reference plane characteristics

$$\lambda^{\pm} = \frac{dx_3}{dx_1} = \frac{M^2\cos\phi\sin\phi\pm\beta}{M^2\cos^2(\phi-1)} \tag{15}$$

the compatibility relation may be written:

$$d\phi \pm \frac{\beta}{\Gamma M^2}\, d(\ell n\ P) = F^{\pm}\ d\tilde{x} \tag{16}$$

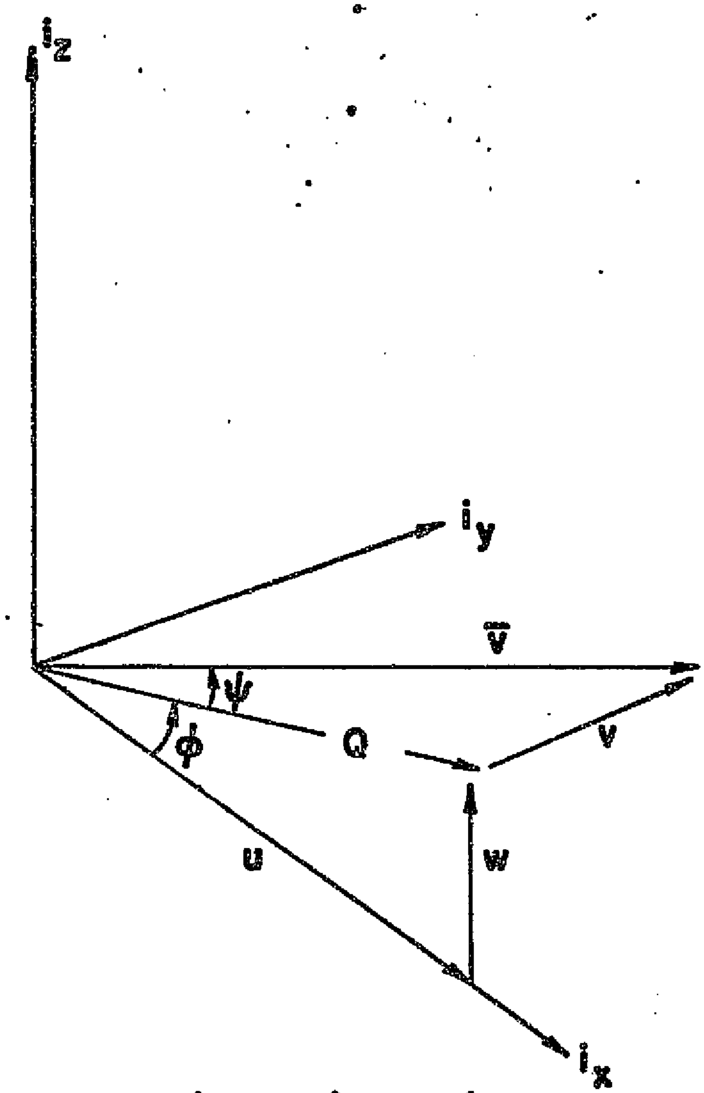

$$\overline{V} = u\,\hat{i}_x + v\,\hat{i}_y + w\,\hat{i}_z$$

$$Q = V\cos\psi \qquad Q = (u^2+w^2)^{1/2}$$

$$u = Q\cos\phi \qquad \phi = \tan^{-1}(w/u)$$

$$v = Q\tan\psi \qquad \psi = \tan^{-1}(v/Q)$$

$$w = Q\sin\phi$$

ORIGINAL PAGE IS OF POOR QUALITY

FIGURE 6. VELOCITY VECTOR IN CARTESIAN SYSTEM

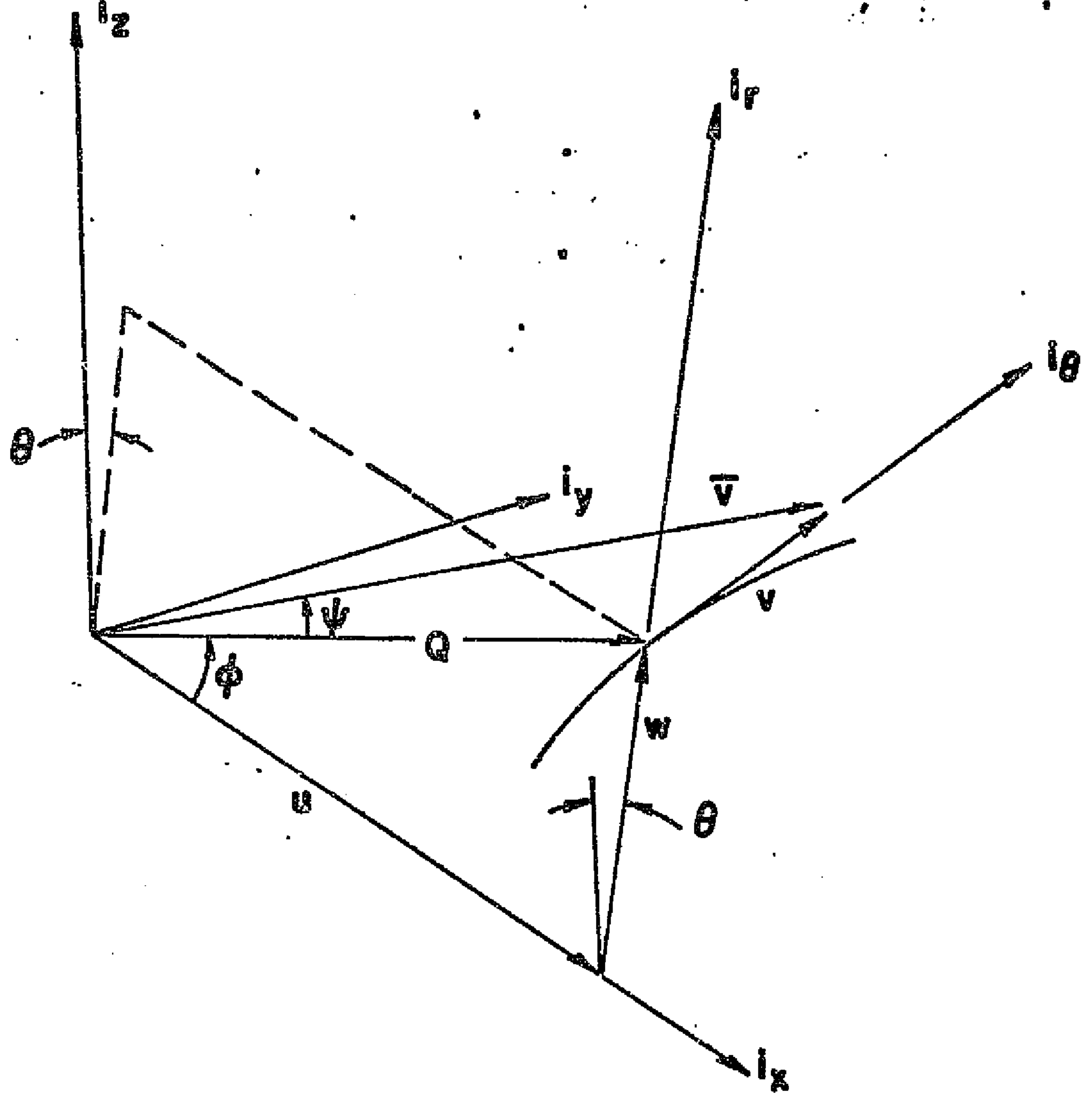

$$V = u\ \hat{i}_x + v\ \hat{i}_\theta + w\ \hat{i}_r$$

$$Q = V\cos\psi \qquad Q = (u^2+w^2)^{1/2}$$

$$u = Q\cos\phi \qquad \phi = \tan^{-1}(w/u)$$

$$v = Q\tan\psi \qquad \psi = \tan^{-1}(v/Q)$$

$$w = Q\sin\phi$$

FIGURE 7. VELOCITY VECTOR IN CYLINDRICAL SYSTEM

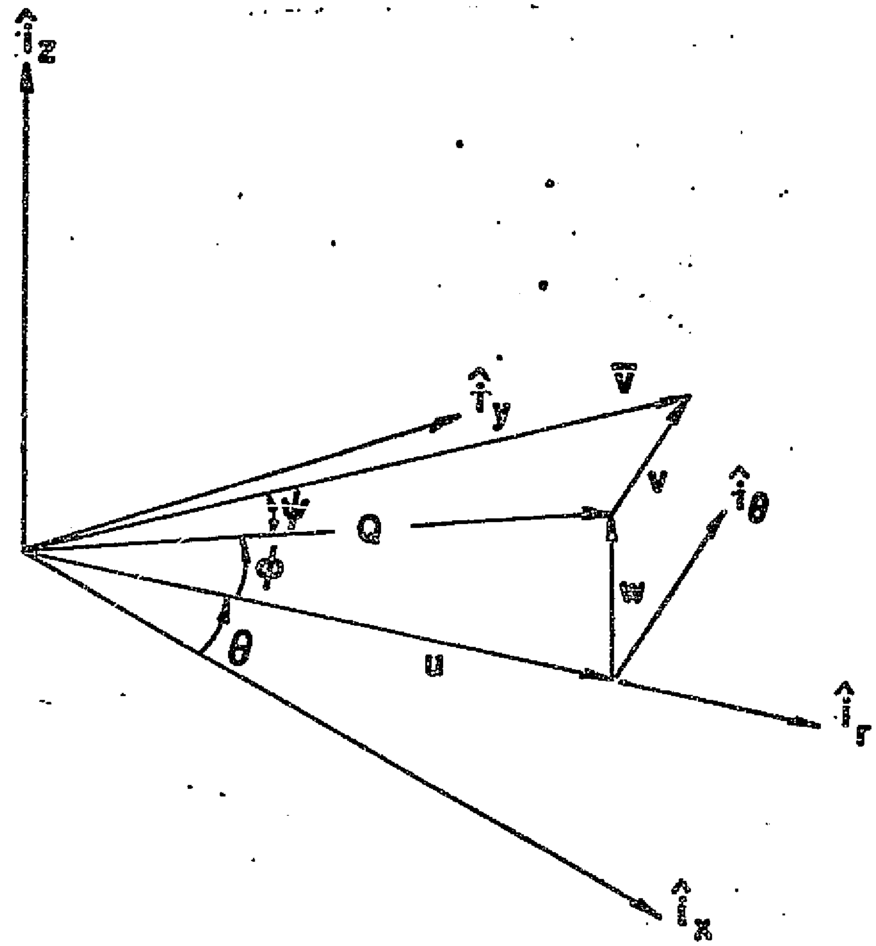

$$V = u\,\hat{i}_r + v\,\hat{i}_\theta + w\,\hat{i}_z$$

$$Q = V\cos\psi \qquad Q = (u^2+w^2)^{1/2}$$

$$u = Q\cos\phi \qquad \phi = \tan^{-1}(w/u)$$

$$v = Q\tan\psi \qquad \psi = \tan^{-1}(v/Q)$$

$$w = Q\sin\phi$$

FIGURE 8. VELOCITY VECTOR IN LINE SOURCE SYSTEM

where

$$M^2 = q^2/a^2, \quad \beta^2 = M^2 - 1$$

$$F^{\pm} = (\sin\phi - \lambda^{\pm}\cos\phi)\ [(\tan\psi)_{x_2} + \frac{\tan\psi}{\Gamma}(\ln P)_{x_2}]$$
$$- \phi_{x_2} \tan\psi\ (\cos\phi + \lambda^{\pm}\sin\phi) + (J_2 - \lambda^{\pm}J_2)\ \tan^2\psi \tag{17}$$

and

$$dx = \frac{dx_1}{\frac{J_2}{x_3}} + J_1\ d\ \ln x_1$$

The streamline projections onto the reference planes

$$\lambda_{SL} = \frac{dx_3}{dx_1} = \tan\phi \tag{18}$$

are also characteristic directions for this system. Along the quasi-stream λ_{SL}, the relation between cross flow angle, ψ, and pressure, P, may be written

$$d(\tan\psi) = \frac{\tan\psi}{\Gamma M^2} d(\ln P) + G\ d\tilde{x} \tag{19}$$

where

$$G = \frac{-1}{\cos\phi}\ [\frac{(\ln P)_{x_2}}{\Gamma M^2} + \tan\psi(\tan\psi)_{x_2}$$
$$+ \tan\psi(1 + \tan^2\psi)\ (J_1\cos\phi + J_2\sin\phi)] \tag{20}$$

B. Finite Difference Analysis (BIGMAC) - The analogous inviscid flow equations in conservation form may be written:

Continuity

$$\nabla\cdot(\rho\bar{V}) = 0$$

Momentum

$$\nabla\cdot(\rho\bar{V}\bar{V}) + \nabla P = 0 \tag{21}$$

Energy

$$\nabla\cdot(\rho\bar{V}H) = 0 \tag{22}$$

Equivalence Ratio Constancy Along Streamlines

$$\nabla\cdot(\rho\bar{V}\Phi) = 0 \tag{23}$$

The scalar form of these equations in the x_1, x_2, x_3 reference plane system may be written:

$$\bar{E}_{x_1} + \bar{F}_{x_2} + \bar{G}_{x_3} + \bar{H} = 0 \tag{24}$$

where for k = 1 to 6

$$\bar{E}(k) = h_2h_3\begin{pmatrix} \rho u \\ P + \rho u^2 \\ \rho uv \\ \rho uw \\ \rho uH \\ \rho u\Phi \end{pmatrix} \quad \bar{F}(k) = h_1h_3\begin{pmatrix} \rho v \\ \rho uv \\ P + \rho v^2 \\ \rho vw \\ \rho vH \\ \rho v\Phi \end{pmatrix}$$

$$\bar{G}(k) = h_1h_2\begin{pmatrix} \rho w \\ \rho uw \\ \rho vw \\ P + \rho w^2 \\ \rho wH \\ \rho w\Phi \end{pmatrix} \quad \bar{H}(k) = \begin{pmatrix} 0 \\ -J_1h_3(P + \rho v^2) \\ (J_1h_3u + J_2h_1w)\rho v \\ -J_2h_1(P + \rho v^2) \\ 0 \\ 0 \end{pmatrix}$$

In performing the numerical integration of this system of equations, a quasi-streamline grid network is employed wherein one follows the projections of streamlines on the reference planes and one to one correspondence is made between "corresponding" streamlines on adjacent reference planes. Then Equation (24) may be written

$$\bar{E}_{\tilde{x}_1} + \bar{F}_{\tilde{x}_2} + \bar{G}_{x_3} + \bar{H} - \frac{h_1}{h_3}\frac{w}{u}\bar{E}_{x_3} - \tan\alpha\,\frac{h_2}{h_3}\bar{F}_{x_3} = 0 \qquad (25)$$

where $\partial/\partial\tilde{x}_1$ denotes the partial derivative along the quasi-streamline, in the reference plane x_2 = constant while $\partial/\partial\tilde{x}_2$ denotes the partial derivative along the line connecting "corresponding" streamline points on adjacent reference planes at the marching station, x_1 = constant. Thus,

$$\left(\frac{\partial}{\partial x_1}\right)_{x_2,x_3} = \left(\frac{\partial}{\partial\tilde{x}_1}\right)_{x_2,\eta} - \frac{h_1}{h_3}\frac{w}{u}\left(\frac{\partial}{\partial x_3}\right)_{x_1,x_3}$$

and

$$\left(\frac{\partial}{\partial x_2}\right)_{x_1,x_3} = \left(\frac{\partial}{\partial\tilde{x}_2}\right)_{x_1,\xi} - \frac{h_2}{h_3}\tan\alpha\left(\frac{\partial}{\partial x_3}\right)_{x_1,x_3}$$

where $\tan\alpha$ is the slope made by the line connecting "corresponding" grid points in adjacent reference planes with respect to the x_2 coordinate direction, at x_1 = constant.

III. COMPUTATIONAL PROCEDURES

A. Reference Plane Grid Networks - Both CHAR3D and BIGMAC employ reference plane grid networks following the trace of streamline projections onto the reference planes as illustrated in Figure (9). Note that the grid network utilized for CHAR3D (Figure 9a) differs from that of the author's previous characteristic method (References 3 and 4) as well as from that of other popular reference plane characteristic methods (References 9 and 10). Previous methods employ a standard inverse scheme (i.e., Figure 9b) wherein interpolations are performed along a non-characteristic initial data surface. Such interpolation procedures ignore the advantages affordable by a reference plane characteristic method by failing to utilize information contained along already calculated quasi-characteristic surfaces. By interpolating along such surfaces, rather than along non-characteristic initial data surfaces, two distinct advantages accrue:

(1) The wave nature of the flow field within the reference planes is preserved.

(2) Linear interpolation procedures along such surfaces is compatible with a scheme of second order accuracy (see Reference 12, appendix).

The application of linear interpolation procedures along a non-characteristic initial data surface does not produce results accurate to second order, while, implementation of higher order interpolative procedures tends to result in excessive numerical diffusion (see Reference 1).

While both CHAR3D and BIGMAC employ the same quasi-streamline reference plane network, the computational sequence differs substantially. Let I designate a grid point in reference plane J; for the calculation of an internal module such as that in Figure (2) each reference plane J contains IMAX grid points where I = 1 represents the lower boundary surface (i.e., vehicle undersurface) while I = IMAX represents the upper boundary (i.e., cowl). In this example J = 1 is a plane of symmetry while J = JW indicates the module sidewall. In CHAR3D, the lower boundary point I = 1 is first calculated for

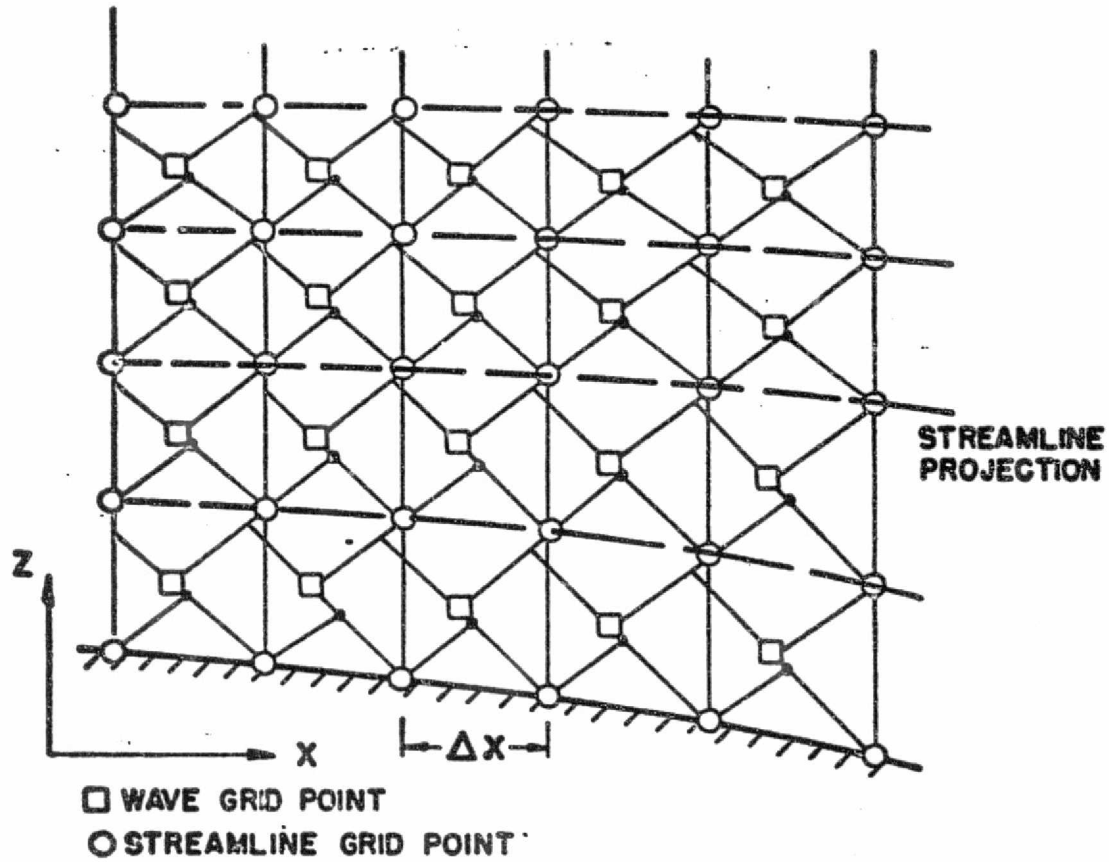

(a) Reference plane grid network for CHAR3D.

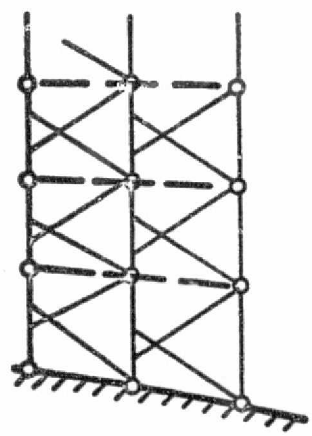

(b) Standard reference plane characteristic network.

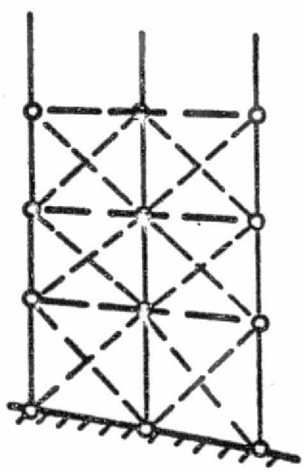

(c) Finite difference network.

Figure 9. Reference plane networks.

all reference planes J = 1 to JW, then the grid points I = 2 for J = 1 to JW, etc., proceeding to the upper boundary point I = IMAX. This provides a quasi-characteristic initial data surface comprised of the downrunning reference plane characteristics passing through the points I for J = 1 to JW for the calculation of the points I + 1 for J = 1 to JW.

Program BIGMAC proceeds in the opposite fashion. Predictor values are calculated for all grid points I = 1 to IMAX in a particular reference plane J starting with J = 1 and proceeding to J = JW. The process is repeated for corrector values.

Both programs employ internal disc storage to provide for the usage of a large number of grid points without exceeding the small core memory allocations of the CDC 7600. Thus, CHAR3D provides storage for all reference plane locations J = 1 to JW ($JW \leq 43$) at 5 levels of I while BIGMAC provides storage for all reference plane grid points I = 1 to IMAX ($IMAX \leq 40$) for 10 reference planes J. In both programs, reference planes are deleted or added in the proximity of sidewalls according to the following criterion. Let Δ represent the spacing between reference planes and Δ_w the spacing between the last reference plane and the sidewall. Then, the reference plane adjacent to the wall is deleted when $\Delta_w < .6$ while a plane is added between the last reference plane and sidewall when $\Delta_w > 1.6$.

B. Interior Point Calculational Procedure - Properties are desired at the grid point ($\bar{I}$,J,K) shown in Figure (10) for a cartesian system. The allowable step size Δx is determined by satisfying the CFL condition. For BIGMAC, this requires that the intersection of the Mach cone from ($\bar{I}$,J,K) with the initial data surface falls within the numerical domain as depicted (i.e., the quadrilateral (I, J + 1), (I - 1, J), (I, J - 1), (I + 1, J)). Note that the effective numerical domain for the characteristic calculation includes the points I + 1 and I - 1 on planes J - 1 and J + 1; hence, a larger step may be taken with CHAR3D ($\Delta x_{CHAR3D} \approx \sqrt{2}\, \Delta x_{BIGMAC}$).

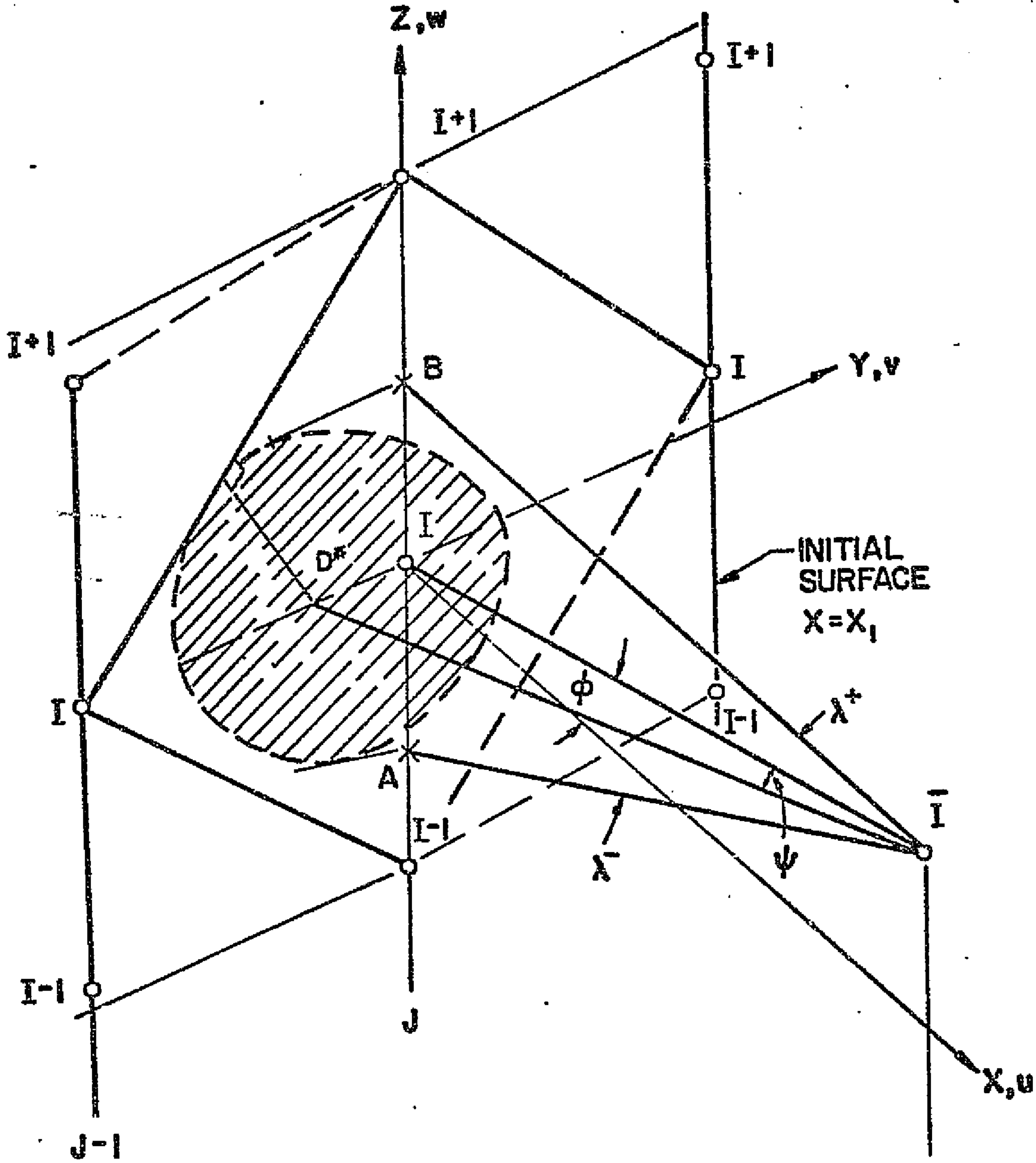

FIGURE 10. CFL STABILITY CRITERION

ORIGINAL PAGE IS OF POOR QUALITY

Referring to Figure (11), for a cartesian system, the grid point $\bar{I}$ is located along the quasi-streamline through grid point I by the difference approximation to Equation (18).

$$z_{\bar{I},J} = z_{I,J} + (a \tan\phi_{I,J} + b \tan\phi_{\bar{I},J})\, \Delta x \tag{26}$$

where a = 1, b = 0 in the predictor step and $a = \frac{1}{2}$, $b = \frac{1}{2}$ in the corrector step. In this new wave preserving network, the calculation proceeds upward from the lower boundary where points ($\bar{I}$ - 1, J) are calculated for <u>all</u> reference planes J to second order prior to calculating points ($\bar{I}$,J). In addition to the standard initial data array (the points (I,J)), an extra array ($\hat{I}$,J) is required. To calculate properties at ($\bar{I}$,J), the standard initial data grid in the reference plane (I - 1, J), (I,J), and (I + 1, J) is employed to calculate the forcing function terms involving derivatives normal to the reference planes. Properties are known at points H_1, G_1, and $\bar{I}$ - 1 from the calculation of point ($\bar{I}$ - 1, J) to second order.

Point A is located between H_1 and G_1 on the quasi-characteristic $\lambda^{\pm}(A\bar{I})$ where $\lambda^{\pm}$ is defined in Equation (15). All properties (including forcing functions) are obtained via <u>linear interpolation</u> between H_1 and G_1. Then, H_2 is located between $\hat{I}$ and I + 1 such that the downrunning quasi-characteristic from G_2 (or B) passes through ($\bar{I}$,J). To first order, properties at ($\bar{I}$,J) are calculated using points B and A, where P_B and ϕ_B are determined using compatibility relations (Equation 16) along IB and H_2B.

Then $P_{\bar{I}}$ and $\phi_{\bar{I}}$ are calculated employing the compatibility relations

$$(\phi_{\bar{I}} - \phi_A) + \left[a \left(\frac{\beta}{\Gamma M^2}\right)_A + b \left(\frac{\beta}{\Gamma M^2}\right)_{\bar{I}} \right] \ln \left(\frac{P_{\bar{I}}}{P_A}\right) = (aF_A^{+} + bF_{\bar{I}}^{+})\, \Delta\tilde{x}_{\bar{I}A}$$

and

$$(\phi_{\bar{I}} - \phi_B) - \left[a \left(\frac{\beta}{\Gamma M^2}\right)_B + b \left(\frac{\beta}{\Gamma M^2}\right)_{\bar{I}} \right] \ln \left(\frac{P_{\bar{I}}}{P_B}\right) = (aF_B^{-} + bF_{\bar{I}}^{-})\, \Delta\tilde{x}_{\bar{I}B} \tag{27}$$

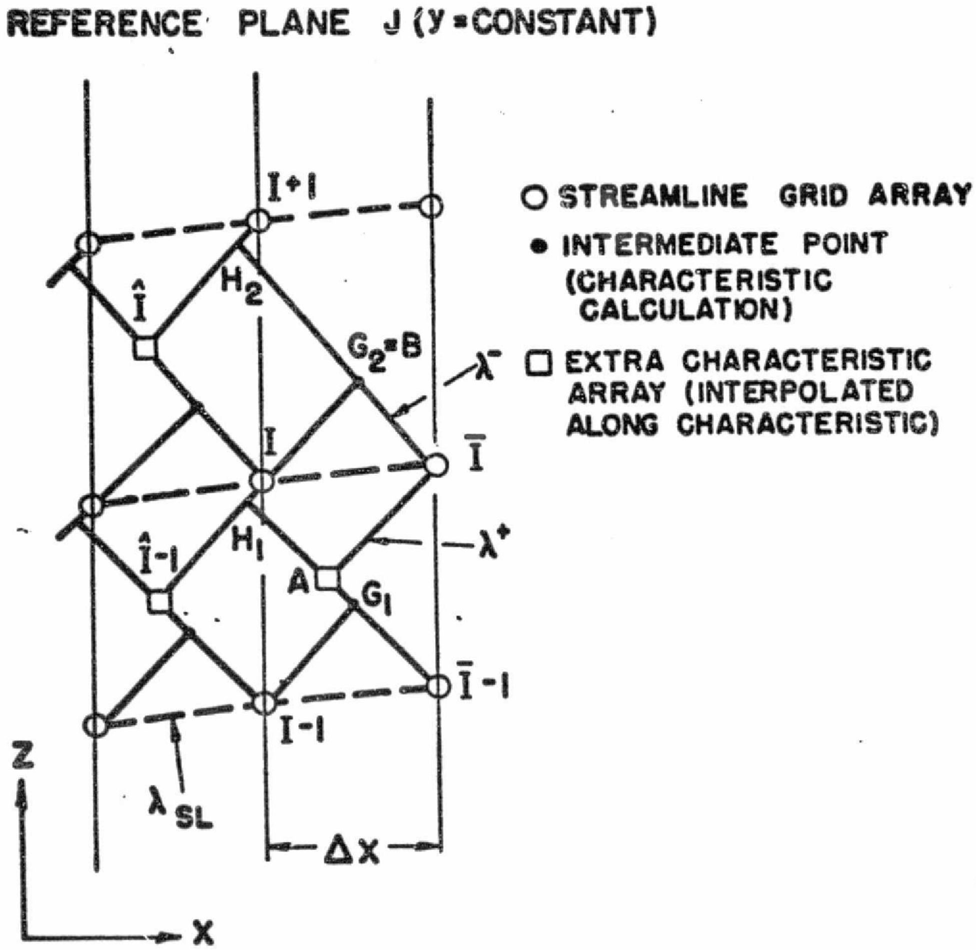

Figure 11. CHAR3D interior point grid.

Remaining properties are determined at $\bar{I}$ via the following streamline relations:

$$(\tan\psi)_{\bar{I}} = (\tan\psi)_{I} + \left[a \left(\frac{\tan\psi}{\Gamma M^2}\right)_{I} + b \left(\frac{\tan\psi}{\Gamma M^2}\right)_{\bar{I}} \right] \ln \left(\frac{P_{\bar{I}}}{P_{I}}\right) + (aG_{I} + bG_{\bar{I}})\, \Delta\tilde{x}_{I\bar{I}} \tag{28}$$

$$H_{\bar{I}} = H_{I} - \left[a \left(\frac{\tan\psi}{\cos\phi} H_y\right)_{I} + b \left(\frac{\tan\psi}{\cos\phi} H_y\right)_{\bar{I}} \right] \Delta\tilde{x}_{I\bar{I}} \tag{29}$$

$$\phi_{\bar{I}} = \phi_{I} - \left[a \left(\frac{\tan\psi}{\cos\phi} \phi_y\right)_{I} + b \left(\frac{\tan\psi}{\cos\phi} \phi_y\right)_{\bar{I}} \right] \Delta\tilde{x}_{I\bar{I}} \tag{30}$$

and in continuous regions of the flow

$$(P/\rho^{\Gamma})_{\bar{I}} = (P/\rho^{\Gamma})_{I} - \left[a \left[\frac{\tan\psi}{\cos\phi} (P/\rho^{\Gamma})_y\right]_{I} + b \left[\frac{\tan\psi}{\cos\phi} (P/\rho^{\Gamma})_y\right]_{\bar{I}} \right] \Delta x_{I\bar{I}} \tag{31}$$

The following three parameter curve fits (based on data from Reference 13) are incorporated into this code and are described in detail in the appendix extracted from Reference (4).

$$h = h\ (P,\Phi,T) \tag{32a}$$

$$\rho = \rho\ (P,\Phi,T) \tag{32b}$$

$$\Gamma = \Gamma\ (P,\Phi,T) \tag{32c}$$

The flow velocity is obtained via the relation

$$V_{\bar{I}} = \sqrt{2}\ [H_{\bar{I}} - h\ (P_{\bar{I}},\ \Phi_{\bar{I}},\ T_{\bar{I}})]^{\frac{1}{2}} \tag{33}$$

where $T_{\bar{I}}$ is obtained via an inversion of Equation (32b) (with $\rho_{\bar{I}}$, $P_{\bar{I}}$, and $\Phi_{\bar{I}}$ known) and $h_{\bar{I}}$ is obtained employing Equation (32a). Then, $\Gamma_{\bar{I}}$ is obtained from Equation (32c) and $a^2 = \Gamma_{\bar{I}}P_{\bar{I}}/\rho_{\bar{I}}$.

This calculation is performed for points $\bar{I}$ in <u>all</u> reference planes to first order. Then, cross derivatives $\partial/\partial y$ are evaluated at $\bar{I}$ employing the relation

$$\left(\frac{\partial f}{\partial y}\right)_{x,z} = \left(\frac{\partial f}{\partial y}\right)_{x,\eta} - \tan\alpha \left(\frac{\partial f}{\partial z}\right)_{x,y} \tag{34}$$

where

$$\left(\frac{\partial f}{\partial y}\right)_{x,\eta} = \frac{f_{\bar{I},J+1}\left(\frac{\Delta y_1}{\Delta y_2}\right) + f_{\bar{I},J}\left(\frac{\Delta y_2}{\Delta y_1} - \frac{\Delta y_1}{\Delta y_2}\right) - f_{\bar{I},J-1}\left(\frac{\Delta y_2}{\Delta y_1}\right)}{(\Delta y_1 + \Delta y_2)}$$

$$\Delta y_1 = y_{\bar{I},J} - y_{\bar{I},J-1} \qquad \Delta y_2 = y_{\bar{I},J+1} - y_{\bar{I},J}$$

$$\tan\alpha = \left(\frac{\partial z}{\partial y}\right)_{x,\eta}$$

$$\left(\frac{\partial f}{\partial z}\right)_{x,y} = \frac{f_{\bar{I},J} - f_{\bar{I}-1,J}}{z_{\bar{I},J} - z_{\bar{I}-1,J}}$$

Derivatives are made the same way at the initial station I, except here $\partial f/\partial z$ is evaluated by

$$\left(\frac{\partial f}{\partial z}\right)_{x,y} = \frac{f_{I+1,J} - f_{I,J}}{z_{I+1,J} - z_{I,J}}$$

CHAR3D, in addition to the centered difference algorithm described above, has the option of evaluating cross derivatives via an alternating one-sided difference algorithm. For this option, derivatives are evaluated as described in the section for BIGMAC. Cross derivatives are required for the variables P, ϕ, ψ, H, Φ, and P/ρ^{Γ}. In evaluating cross derivatives for P, ϕ, and ψ, conservation variables are employed as follows:

$$P_y = F(3)_y - F(1)\ v_y - v\ F(1)_y$$

$$\phi_y = \frac{w_y \cos\phi - u_y \sin\phi}{q} \tag{35}$$

$$(\tan\psi)_y = \frac{q v_y - (u u_y + w w_y)\tan\psi}{q^2}$$

where

$$v_y = \frac{E(3)_y - v\ E(1)_y}{E(1)}$$

$$u_y = \frac{E(2)_y - h_2 h_3 P_y - u\ E(1)_y}{E(1)} \tag{36}$$

$$w_y = \frac{E(4)_y - w\ E(1)_y}{E(1)}$$

The conservation variables E(k) and F(k) are given by Equation (24). The use of conservation variables in the construction of these cross derivatives has tended to suppress oscillations that occurred when employing physical variables to difference across shock waves. However, the use of a one-sided difference algorithm in conjunction with CHAR3D has tended to produce spurious results in regions of large cross flow.

In the characteristic reference plane algorithm, cross flow variations are expressed via the forcing function terms $F^{\pm}$ appearing in the right side of the compatibility relations (Equation 16). These terms are assumed to vary mildly within an integration step. When a one-sided algorithm is employed to evaluate cross derivatives in the vicinity of shocks, the values of the forcing function terms may vary greatly between the predictor and corrector steps. In addition, the numerical domain of dependence is somewhat vague for the characteristic reference plane approach in conjunction with one-sided differences, so that part of the problem encountered may be due to stability. The recommended approach for evaluating cross derivatives in CHAR3D is to employ conservation variables in conjunction with a centered difference algorithm, although this matter requires further study.

In CHAR3D, secondary shocks are captured as rapid changes spread over approximately three grid points. The entropy change associated with these shocks is evaluated employing a nonisentropic pressure-density relation (illustrated here for a perfect gas).

$$\bar{V}\cdot\nabla \ln (P/\rho^{\gamma}) = \bar{V} \cdot \frac{\nabla S}{C_v} \tag{37}$$

For a shock of strength ξ (pressure ratio across shock), this change is determined employing the relation (for perfect gas)

$$\frac{\Delta S}{C_v} = \ln \xi - \gamma \ln \left[\frac{(\gamma + 1)\xi + (\gamma - 1)}{(\gamma - 1)\xi + (\gamma + 1)}\right] \tag{38}$$

where ΔS is the entropy change along a streamline produced by the captured shock. This relation involves only the pressure distribution in the vicinity of the shock and is readily applied in regions of noninteracting shocks as follows. Let

$$F(\xi,\Gamma) = \frac{(\gamma + 1)\xi + (\gamma - 1)}{(\gamma - 1)\xi + (\gamma + 1)}$$

Assume a shock is spread over the marching interval K = 1 to 6 (Figure 12) for a typical quasi-streamline. Then 1 represents free stream conditions for this shock. The entropy change in the interval K - 1 to K is then expressed by

$$\left(\frac{\Delta S}{C_v}\right)_{K-1,K} = \left(\frac{\Delta S}{C_v}\right)_{1,K} - \left(\frac{\Delta S}{C_v}\right)_{1,K-1} = \ln \left[\frac{\xi_{1,K}}{\xi_{1,K-1}} \; \frac{F_{1,K-1}}{F_{1,K}}\right]^{\gamma}$$

where

$$\xi_{1,K} = P_K/P_1$$

Then

$$(P/\rho^{\gamma})_K = \left[(P/\rho^{\gamma})_{K-1} - \frac{\tan\psi}{\cos\phi} (P/\rho^{\gamma})_y \, \Delta\tilde{x}_{K-1,K}\right] \exp \left(\frac{\Delta S}{C_v}\right)_{K-1,K} \tag{39}$$

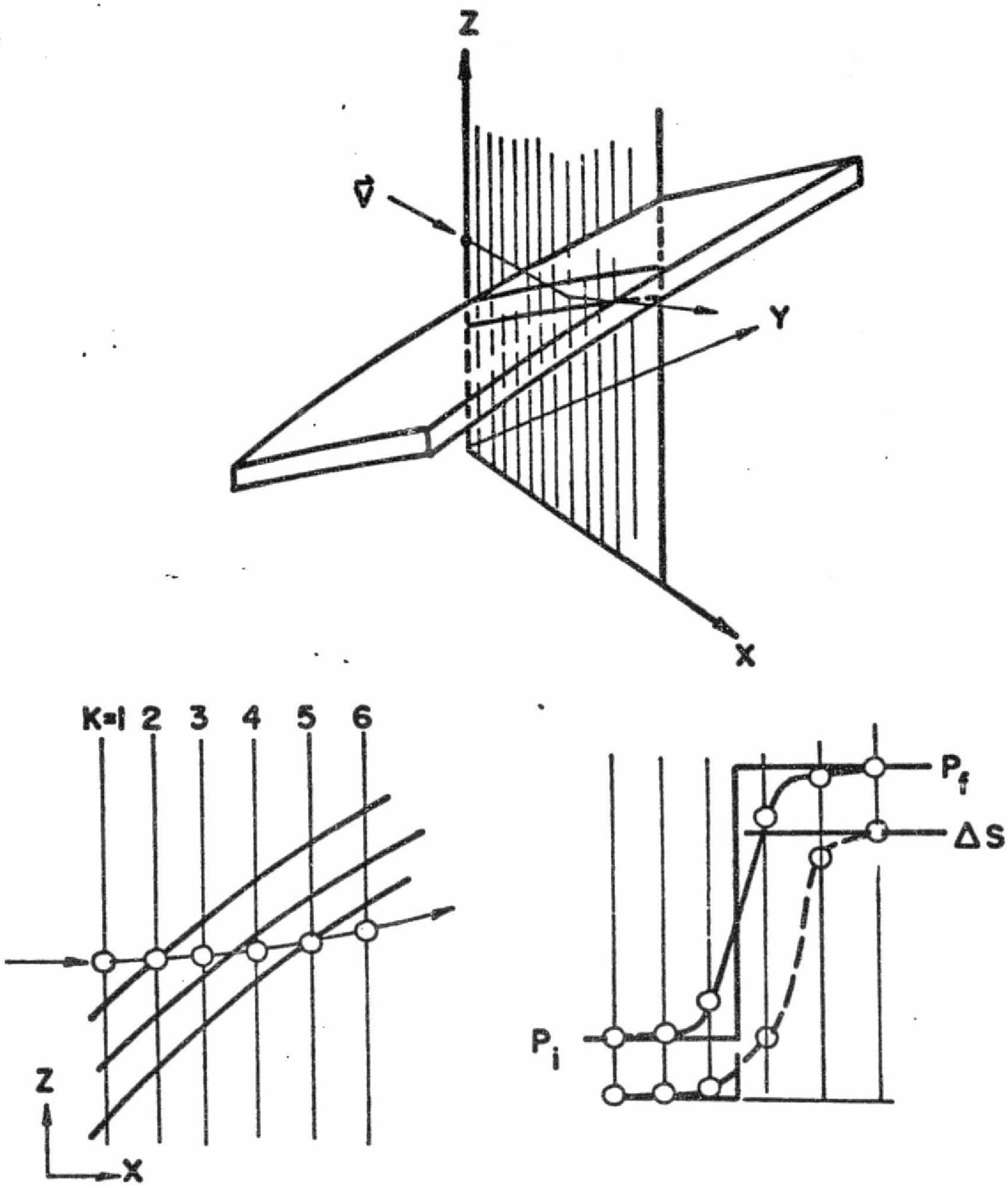

Figure 12. Entropy calculational procedure. P_i is initial pressure; P_f is final pressure.

Since the shock geometry does not appear in the entropy jump relation, the entropy rise associated with extremely complex three-dimensional shocks can be accurately obtained. Special provisions have been incorporated into the program for the computation of singular points at the juncture of intersecting shock waves and/or shock reflection points. At such points the streamline undergoes a discontinuous pressure rise corresponding to that through both shock waves. If the shock intensities are different, an entropy discontinuity occurs separating the different zones, and a vortex of infinite intensity results. Numerically, the entropy procedure described would predict an entropy rise associated with this pressure jump. Theoretically, this occurs in the limit of vanishing mass flow, while numerically the finite mass within this region would lead to unduly large entropy levels. Special coding has been incorporated at such singular points to suppress these "numerical" peaks.

BIGMAC

The MacCormack difference algorithm of Reference (14) is employed for the calculation of interior grid points in BIGMAC. Referring to Figures (13), (14) and (15) for grid index notation in the coordinate systems considered, this two step predictor-corrector scheme as applied to Equation (25) yields

Predictor Step

$$\tilde{E}_{\bar{I},J} = E_{I,J} - 2\,\Delta x_1 \left(F_{x_2} + G_{x_3} - \frac{h_1}{h_3}\frac{w}{u}E_{x_3} - \frac{h_2}{h_3}F_{x_3}\tan\alpha + \frac{H}{2}\right)_{I,J} \tag{40a}$$

where

$$\tan\alpha = \pm 2 \left(\frac{x_{3_{I,J\pm1}} - x_{3_{I,J}}}{d_1 + d_2}\right)\left(\frac{d_1}{d_2}\right)^{\pm1}\left(\frac{h_3}{h_2}\right)$$

$$\left.\frac{\partial f}{\partial y}\right|_{I,J} = \pm \left(\frac{f_{I,J\pm1} - f_{I,J}}{d_1 + d_2}\right)\left(\frac{d_1}{d_1}\right)^{\pm1}$$

$$\left.\frac{\partial f}{\partial z}\right|_{I,J} = \pm \left(\frac{f_{I\pm1,J} - f_{I,J}}{d_3 + d_4}\right)\left(\frac{d_3}{d_4}\right)^{\pm1}$$

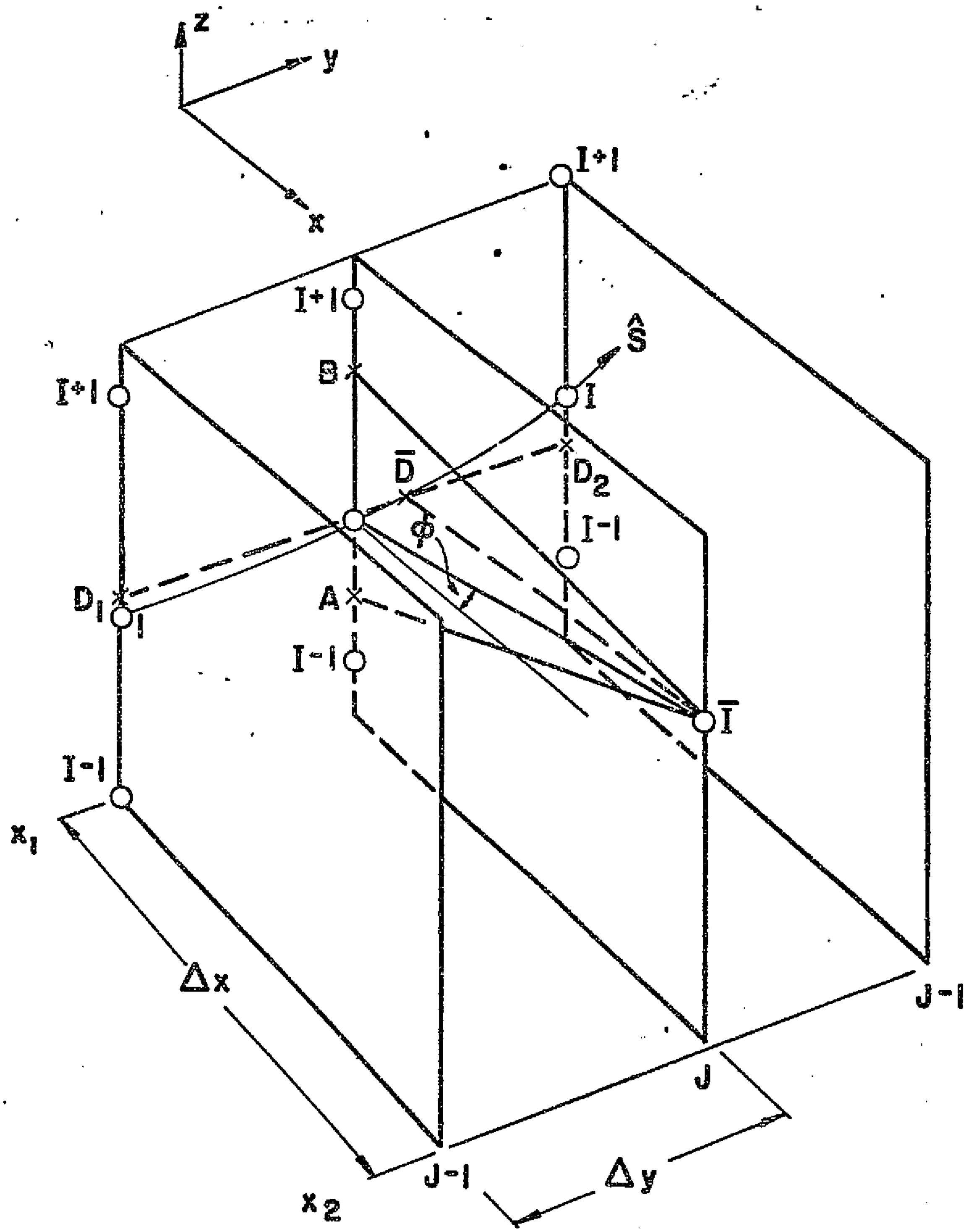

FIGURE 13. NUMERICAL GRID FOR CARTESIAN SYSTEM

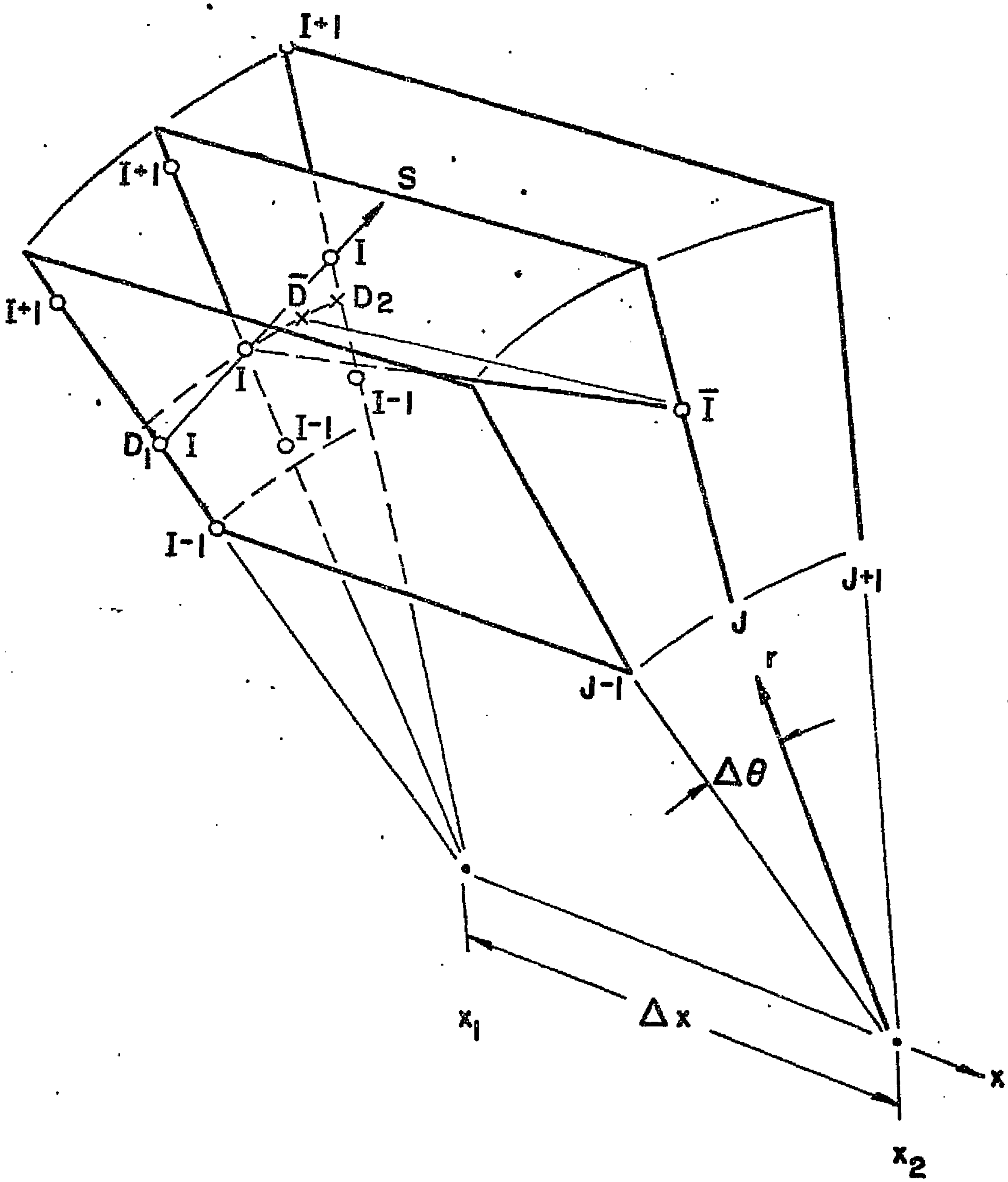

FIGURE 14. NUMERICAL GRID FOR CYLINDRICAL SYSTEM

ORIGINAL PAGE IS
OF POOR QUALITY

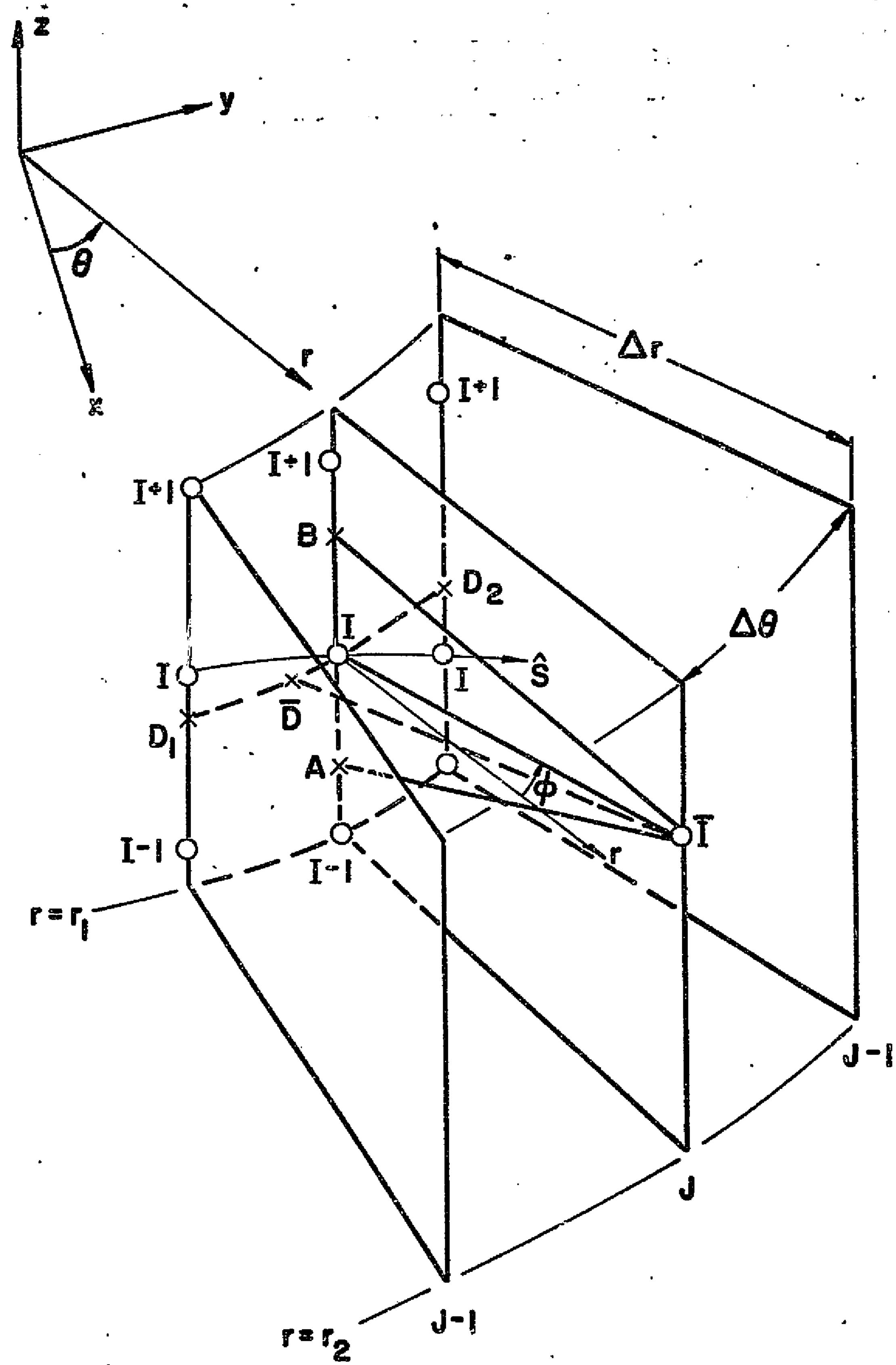

FIGURE 15. NUMERICAL GRID FOR LINE-SOURCE SYSTEM

$$d_1 = x_{2_{I,J}} - x_{2_{I,J-1}} \qquad d_2 = x_{2_{I,J+1}} - x_{2_{I,J}}$$

$$d_3 = x_{3_{I,J}} - x_{3_{I-1,J}} \qquad d_4 = x_{3_{I+1,J}} - x_{3_{I,J}}$$

for any variable f and

Corrector Step

$$E_{\bar{I},J} = \frac{1}{2} \left[(\tilde{E}_{\bar{I},J} + E_{I,J}) - 2\,\Delta x_1 \,[\tilde{F}_{x_2} + \tilde{G}_{x_3} - \frac{h_1}{h_3} (\frac{\tilde{w}}{\tilde{u}})\, \tilde{E}_{x_3} - \frac{h_2}{h_3} \tilde{F}_{x_3} \tan\tilde{\alpha} + \frac{\tilde{H}}{2}]_{\bar{I},J} \right] \tag{40b}$$

where

$$\tan\tilde{\alpha} = \mp 2 \left(\frac{\tilde{x}_{3_{I,J\mp1}} - \tilde{x}_{3_{I,J}}}{d_1 + d_2}\right) \left(\frac{\tilde{d}_2}{\tilde{d}_1}\right)^{\pm 1} \left(\frac{h_3}{h_2}\right)$$

$$\left.\frac{\partial \tilde{f}}{\partial y}\right|_{\bar{I},J} = \mp \left(\frac{\tilde{f}_{I,J\mp1} - \tilde{f}_{I,J}}{d_1 + d_2}\right) \left(\frac{\tilde{d}_2}{\tilde{d}_1}\right)^{\pm 1}$$

$$\left.\frac{\partial \tilde{f}}{\partial z}\right|_{\bar{I},J} = \mp \left(\frac{\tilde{f}_{I\mp1,J} - \tilde{f}_{I,J}}{d_3 + d_4}\right) \left(\frac{\tilde{d}_4}{\tilde{d}_3}\right)^{\pm 1}$$

for any variable $\tilde{f}$

$$\tilde{x}_{3_{\bar{I},J}} = x_{I,J} + \left(\frac{h_1}{h_3} \frac{w}{u}\right)_{I,J} \Delta x_1$$

$$x_{3_{\bar{I},J}} = x_{I,J} + \frac{1}{2} \left[\left(\frac{h_1}{h_3} \frac{w}{u}\right)_{I,J} + \left(\widetilde{\frac{h_1}{h_3} \frac{w}{u}}\right)_{\bar{I},J} \right] \Delta x_1$$

The physical variables are obtained by the following iterative decoding procedure. A value of u is assumed. Then,

$$\rho = E(1)/(h_2 h_3 u) \tag{41a}$$

$$P = (E(2) - E(1)\ u)/(h_2 h_3) \tag{41b}$$

$$v = E(3)/E(1) \tag{41c}$$

$$w = E(4)/E(1) \tag{41d}$$

$$H = E(5)/E(1) \tag{41e}$$

$$\Phi = E(6)/E(1) \tag{41f}$$

$$h = H - \frac{1}{2}\ (u^2 + v^2 + w^2) \tag{41g}$$

The value of h obtained in Equation (41g) yields T via an inversion of Equation (32a). Equation (32b) yields an alternate value of the density compared to that obtained in Equation (41a). The value of u is perturbed and the procedure repeated until the two values of density agree to within a specified tolerance. A linear error extrapolation is employed to speed convergence.

Note that both codes additionally provide for the calculation of a uniform composition, perfect gas mixture. For this option, the equilibrium sound speed, a, of Equation (6) is replaced by the frozen sound speed

$$a_f^2 = \left(\frac{\partial P}{\partial \rho}\right)_S = \frac{\gamma P}{\rho} \tag{42}$$

where the constant specific heat ratio of the frozen mixture γ, replaces the equilibrium isentropic exponent Γ in all relations. The static enthalpy is then expressed by

$$h\ (P,\rho) = \frac{\gamma}{\gamma - 1}\ P/\rho \tag{43}$$

and the iterative decoding procedure of Equations (41a-g) may be replaced by the direct determination of the u velocity component via solution of the quadratic (Reference 15)

$$u = [-B + (B^2 - 4AC)^{\frac{1}{2}}]/2A \tag{44}$$

where

$$A = (\gamma+1)/2\gamma$$

$$B = -E(2)/E(1)$$

$$C = \frac{\gamma-1}{2\gamma}(2H - v^2 - w^2)$$

C. Solid Surface Calculational Procedure - Surface geometry is prescribed via discrete contour data for all continuous surfaces comprising the nozzle/afterbody configuration. Thus, for rectangular modules, as depicted in Figure (1), contour data is provided for four surfaces, namely, the two sidewalls, vehicle undersurface and cowl. These surfaces are fit via the method of Reference (11) based on the use of partial cubic splines; a summary of this fitting technique is provided in Appendix II. Surface fitting is done external to programs CHAR3D and BIGMAC via program FIT3D, (Reference 11) which generates ordered surface coefficient arrays read in via tape to CHAR3D and BIGMAC and employed in these codes in conjunction with surface interpolation procedures also described in Appendix II.

Both CHAR3D and BIGMAC employ reference plane characteristic procedures in the performance of <u>all</u> boundary calculations. The calculational procedure for CHAR3D closely follows the step by step procedures detailed in Reference (4). Referring to Figure (16), which depicts a lower boundary calculation in cartesian coordinates, CD is the intersection of the reference plane $y = y_c$ with the lower surface $z = f(x,y)$. In CHAR3D, the following iterative procedure is entailed:

(a) The cross flow angle ψ_c is assumed equal to that at point D.

(b) The boundary condition $\bar{V}\cdot\hat{n} = 0$ applied at point c yields the relation

$$\sin\phi_c = (f_x)_c \cos\phi_c + (f_y)_c \tan\psi_c \tag{45}$$

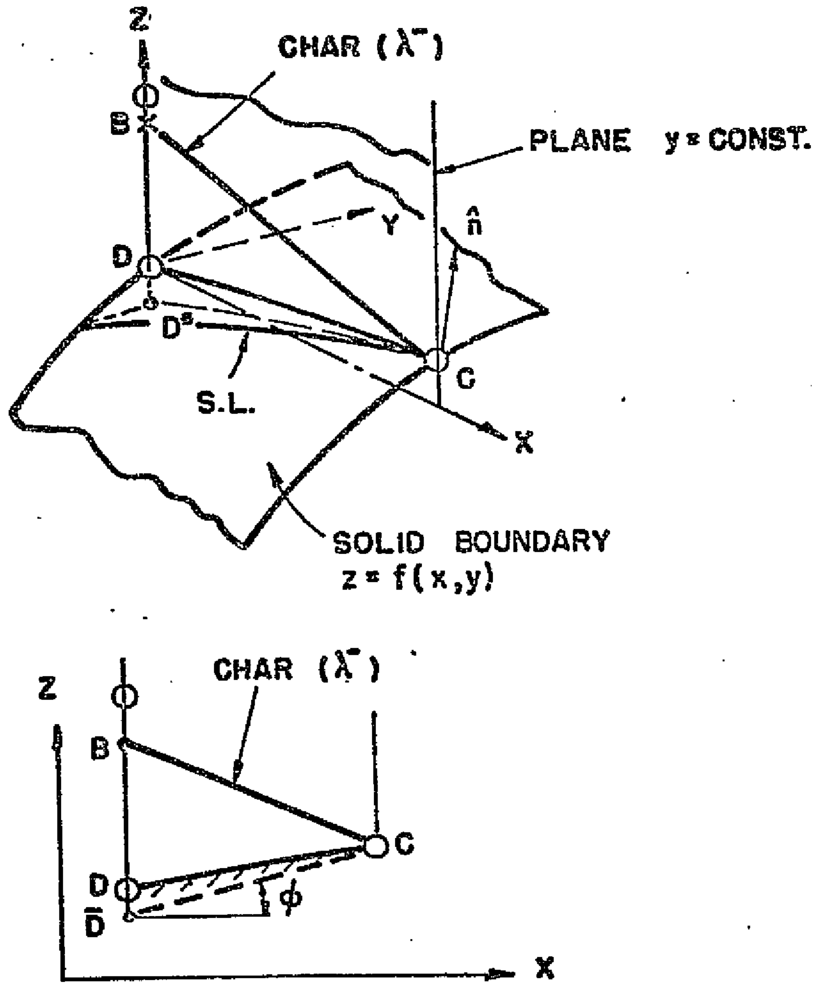

Figure 16. Solid boundary calculation.

(c) P_c is obtained employing the compatibility relation (Equation 27) along λ^- using the above value of ϕ_c.

(d) An alternate value of ψ_c is obtained employing the normal momentum relation (Equation 28) along CD.

This new value of ψ_c is then employed and steps (b), (c) and (d) are repeated. This self convergent procedure generally requires only 2 or 3 iterations, although more may be required in regions of strong cross flow. Upon convergence, streamline relations yield remaining properties at c and the entire process is repeated for second order accuracy.

In BIGMAC, this iterative procedure is eliminated by combining the normal momentum equation with the quasi-streamline momentum equation yielding the following system of equations for P_c, $(w/u)_c$ and $(v/u)_c$ in general coordinates for the boundary $x_3 = f(x_1, x_2)$:

$$\begin{pmatrix} (\rho u^2/\beta P)_{BC} & \pm 1 & 0 \\ 1 & 0 & \dfrac{-(f_{x_2})_c}{h_2} \\ (vw/q^2)_{CD} & \left(\dfrac{v}{u}\dfrac{P}{\rho q^2}\right)_{CD} & -1 \end{pmatrix} \begin{pmatrix} (w/u)_c \\ \ln P_c \\ (v/u)_c \end{pmatrix} = \begin{pmatrix} R_1 \\ R_2 \\ R_3 \end{pmatrix} \tag{46}$$

where

$$R_1 = -\frac{h_1}{\beta P\ h_1 h_2 h_3}\left[(\lambda^{\pm} u - w)\ A - \lambda^{\pm} B\right]_{BC} \Delta\tilde{x}_{BC} \pm \ln P_B + \left(\frac{\rho u^2}{\beta P}\right)\left(\frac{w}{u}\right)_B$$

$$R_2 = (f_{x_1})_c$$

$$R_3 = \frac{h_1}{\rho u^2\ h_1 h_2 h_3}\left[E_{SL} - \frac{v}{q^2}(Bu + Gw)\right]_{CD} \Delta\tilde{x}_{CD}$$

ORIGINAL PAGE IS OF POOR QUALITY

and

$$A = h_1 h_3 \left(\frac{vP_y}{a^2} + \rho v_y\right) + J_1 \frac{E(1)}{h_2} + J_2 \frac{G(1)}{h_2}$$

$$B = F(2)_y - u\ F(1)_y - J_1 \frac{v\ F(1)}{h_1}$$

$$C = F(4)_y - w\ F(1)_y - J_2 \frac{v\ F(1)}{h_3}$$

$$E_{SL} = F(3)_y - v\ F(1)_y + J_1 \frac{F(2)}{h_1} + J_2 \frac{F(4)}{h_3}$$

Note that in the above relations, v_y and P_y are evaluated in accordance with Equation (36).

An important consideration in the boundary procedure for BIGMAC is the determination of the entropy at point C. The entropy change along the wall from D^* to C is set equal to that along the streamline one mesh interval away from the wall. Thus, entropy changes associated with captured shocks as determined for interior grid points, are reflected in the wall point calculation. To accommodate this procedure, the lower wall point calculation must be deferred until after the calculation of the grid point one mesh interval from the wall and, the left sidewall calculations must be deferred until after the calculation of the adjacent reference plane. Then, predictor values are obtained at point C for P_c, $(w/u)_c$ and $(v/u)_c$ employing coefficients evaluated at the initial station. Streamline relations yield H_c and Φ_c and the density ρ_c, via Equation (39) where the entropy change is evaluated as described above. The velocity magnitude V_c is obtained via Equation (33) in conjunction with the equilibrium curve fits of Equation (32). Corrector values are evaluated with averaged values of the coefficients after predictor values have been obtained for the numerical domain under consideration.

The same general logic is applicable for the calculation of all solid boundaries. In particular, for the calculation of sidewalls, a local rotated reference plane system is established as indicated in Figures (2) - (4). The calculation is performed in the plane $x_3 = x_{3_c}$ for which geometric details are depicted in Figure (17) for a line source or cartesian system and in Figure (18) for a cylindrical system. Appropriate relations in the rotated system are provided via the transformations

$$\bar{x}_1 = x_1 \quad \bar{x}_2 = -x_3 \quad \bar{x}_3 = x_2 \tag{47a}$$

$$\bar{u} = u \quad \bar{v} = -w \quad \bar{w} = v \tag{47b}$$

The metric coefficients $\bar{h}_2$ then become

$$\bar{h}_1 = 1$$

$$\bar{h}_2 = 1$$

$$\bar{h}_3 = (J_1 x_1 - J_2 x_3) + (1 - J_1 + J_2)$$

Characteristic directions in the rotated system take the form:

$$\lambda^{\pm} = \frac{\bar{h}_3}{\bar{h}_1}\frac{d\bar{x}_3}{d\bar{x}_1} = \frac{\bar{u}\bar{w} \pm a\sqrt{\bar{u}^2+\bar{w}^2-a^2}}{\bar{u}^2 - a^2} \tag{48}$$

The compatibility relation along the characteristics may be written:

$$\frac{\rho\bar{u}^2}{\beta P}\, d\,(x\,\bar{w}/\bar{u}) \pm d\ell nP = \bar{D}^{\pm}\quad d\tilde{x}_{\lambda^{\pm}} \tag{49}$$

where

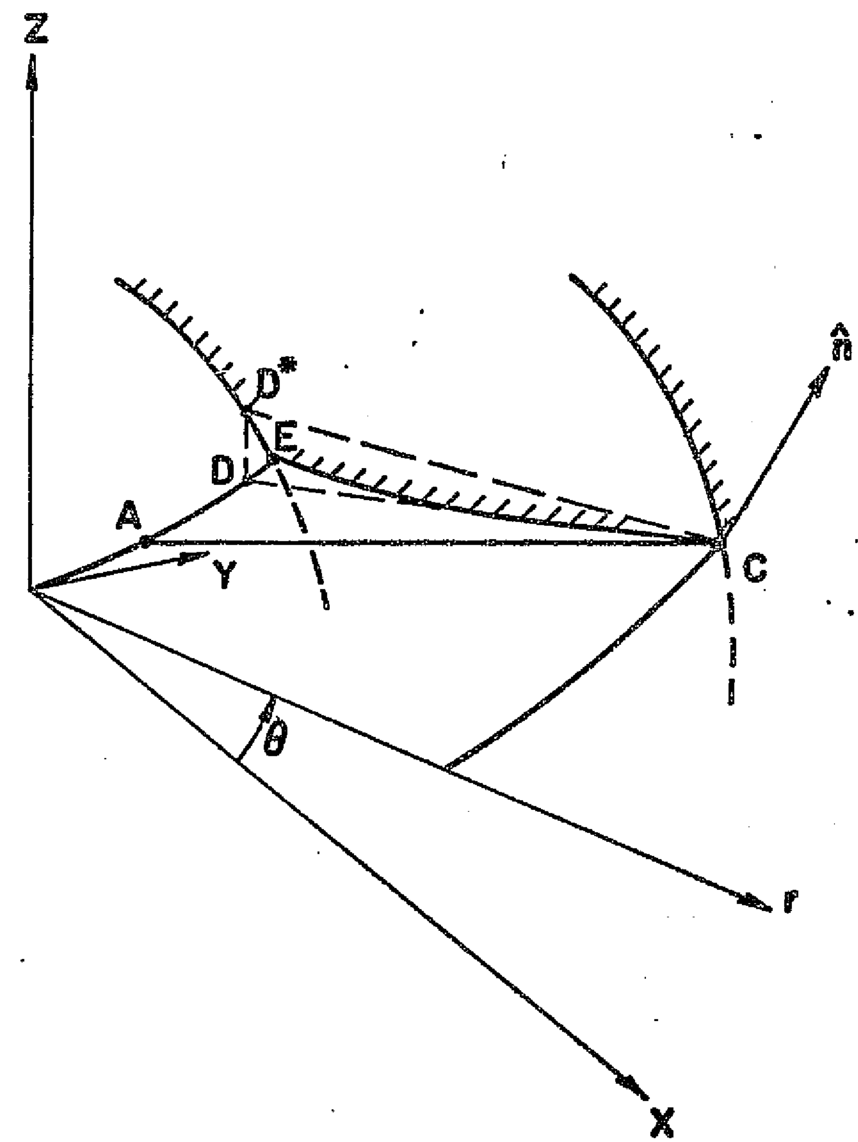

FIGURE 17. SIDEWALL CALCULATION, LINE SOURCE OR CARTESIAN SYSTEM.

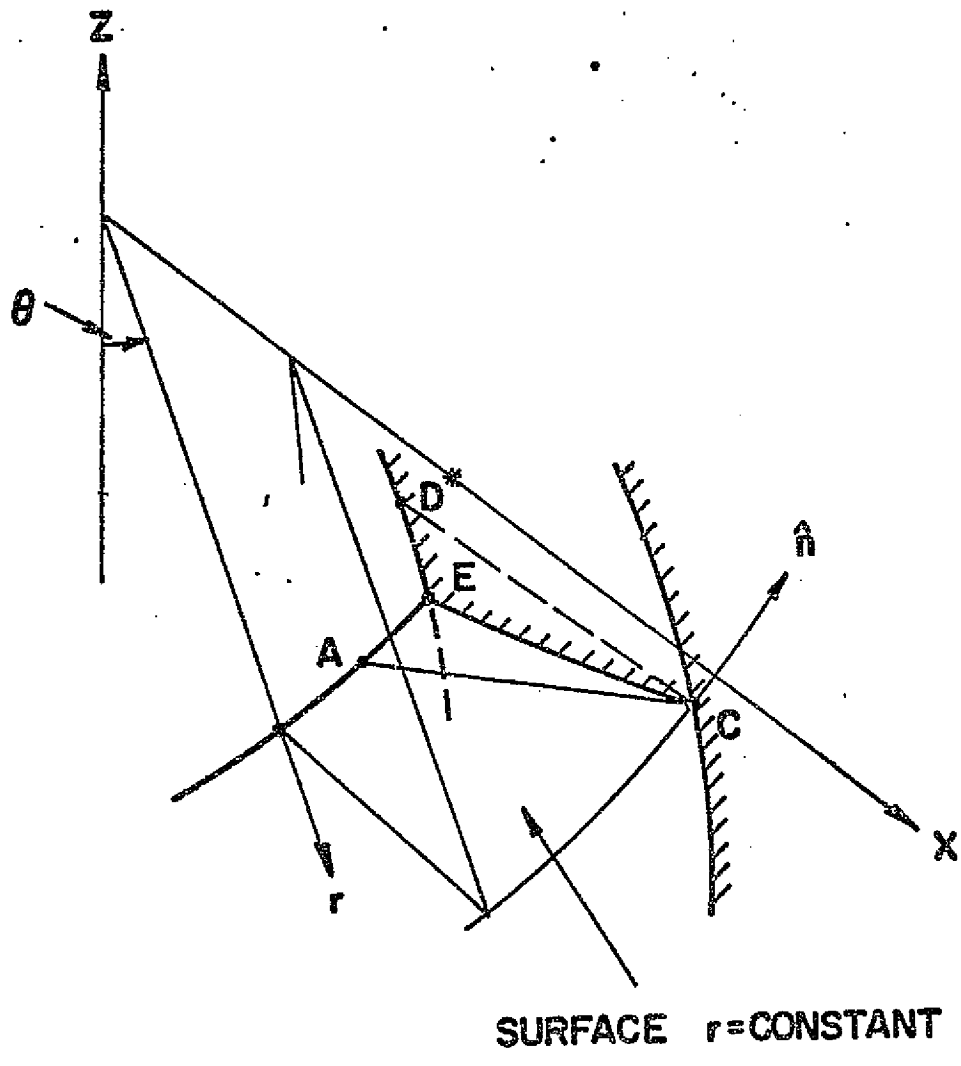

FIGURE 18. SIDEWALL CALCULATION, CYLINDRICAL SYSTEM

$$\bar{D}^{\pm} = -\frac{1}{\bar{h}_1\bar{h}_2\bar{h}_3}[(\lambda^{\pm}\,\bar{u} - \bar{w})\,\bar{A} - \lambda^{\pm}\,\bar{B} + \bar{C}]$$

$$\bar{A} = [\bar{h}_1\bar{h}_3\,(\frac{\bar{v}}{a^2}\,P_{\bar{x}_2} + \rho\,\bar{v}_{\bar{x}_2}) + J_1\bar{h}_2\rho\bar{u} - J_2\bar{h}_1\rho\bar{v}]$$

$$\bar{B} = [(\bar{h}_1\bar{h}_3\,\rho\bar{u}\bar{v})_{\bar{x}_2} - \bar{u}(\bar{h}_1\bar{h}_3\rho\bar{v})_{\bar{x}_2} - J_1\bar{h}_2\rho\bar{w}^2]$$

$$\bar{C} = [(\bar{h}_1\bar{h}_3\rho\bar{v}\bar{w})_{\bar{x}_2} - \bar{w}(\bar{h}_1\bar{h}_2\rho\bar{v})_{\bar{x}_2} + J_1\rho\bar{w}\bar{u}\bar{h}_2 - J_2\rho\bar{w}\bar{v}\bar{h}_1]$$

The combined momentum equation takes the form:

$$d(\frac{\bar{v}}{\bar{u}}) - (\frac{\bar{v}\bar{w}}{q^2})\,d(\frac{\bar{w}}{\bar{u}}) - \frac{\bar{v}}{\bar{u}}\,\frac{P}{\rho q^2}\,d(\ell nP) = \frac{1}{\rho u^2}\,[\bar{E}_{SL} - \frac{\bar{v}}{q^2}\,(B\bar{u} + C\bar{w})]\,d\tilde{x}_{SL} \quad (5$$

where.

$$\bar{E}_{SL} = -\frac{1}{\bar{h}_1\bar{h}_2\bar{h}_3}[(\bar{h}_1\bar{h}_3\,(P + \rho\bar{v}^2))_{\bar{x}_2} - \bar{v}(\bar{h}_1\bar{h}_3\rho\bar{v})_{\bar{x}_2} + J_2\bar{h}_1\,(P + \rho\bar{w}^2)]$$

The statement of the boundary condition $\bar{V}\cdot\hat{n} = 0$ on the sidewall $g = g(x_1, x_3)$ $= g(\bar{x}_1, \bar{x}_2)$ may be written:

$$\frac{\bar{w}}{\bar{u}} = h_3(g_{\bar{x}_1} + \frac{\bar{v}}{\bar{u}}\,g_{\bar{x}_2}) \quad (5$$

The system of Equations (49) - (51) is solved directly for the variables $\bar{w}/\bar{u}$, $\bar{v}/\bar{u}$ and P. The analogous boundary relations in rotated coordinates for CHAR3D are detailed in Reference (4) for the three coordinate systems incorporated in this analysis.

D. Corner Point Calculations Procedure - Interior corners occur in the internal modules and are discretely analyzed in both numerical codes by a redundant "weighted" characteristic procedure. For a cartesian system the corner results from the intersection of the surfaces $z = f(x,y)$ and $y = g(x,z)$.

Referring to Figure (19), the boundary condition $\bar{V}\cdot\hat{n} = 0$ applied to both intersecting surfaces at C (the point to be calculated) yields explicit expressions for the flow deflection angles in the reference plane $y = y_c$:

$$\left(\frac{w}{u}\right)_c = \tan\phi_c = \left(\frac{f_x + g_x\, f_y}{1 - g_z\, f_y}\right) \tag{52}$$

$$\left(\frac{v}{q}\right)_c = \tan\psi_c = \left(\cos\phi_c\, \frac{g_x + f_x\, g_z}{1 - f_y\, g_z}\right) \tag{53}$$

Then, a redundant procedure is employed wherein reference plane calculations for the pressure at C are performed in the reference planes $z = z_C$ and $y = y_C$. This yields two values of pressure P_{C_1} and P_{C_2} which differ due to evaluating the cross derivative forcing function terms in the compatibility relations via backward differences. A weighting of these pressures is performed by accounting for the relative wave strengths in each of these reference planes. This gives the stronger weighting to the calculation performed in the reference plane containing the dominant waves via the relation

$$P_C = \frac{\Delta\psi_{A_1C}}{\Delta\psi_{A_1C} + \Delta\phi_{A_2C}}\, P_{C_1} + \frac{\Delta\phi_{A_2C}}{\Delta\psi_{A_1C} + \Delta\phi_{A_2C}}\, P_{C_2} \tag{54}$$

In the line source system, the upper or lower walls are specified by relations of the form $z = f(r,\theta)$ while the sidewall by $y = g(x,z)$, as indicated in Figure (20). Application of the boundary condition $\bar{V}\cdot\hat{n}$ at both walls in conjunction with the transformation

$$\begin{pmatrix} \bar{u} \\ \bar{v} \\ \bar{w} \end{pmatrix} = \begin{pmatrix} \cos\theta & -\sin\theta & 0 \\ \sin\theta & \cos\theta & 0 \\ 0 & 0 & 1 \end{pmatrix} \begin{pmatrix} u \\ v \\ w \end{pmatrix} \tag{55}$$

from line source velocity components, u,v,w to cartesian components $\bar{u},\bar{v},\bar{w}$ yields

$$\tan\phi_c = \left(\frac{w}{u}\right)_c = \frac{f_r\,(1 + g_x \tan\theta) + \frac{f\theta}{r}\,(g_x - \tan\theta)}{\left(1 + g_x \tan\theta - g_z\,\frac{f\theta}{r}\right)} \tag{56}$$

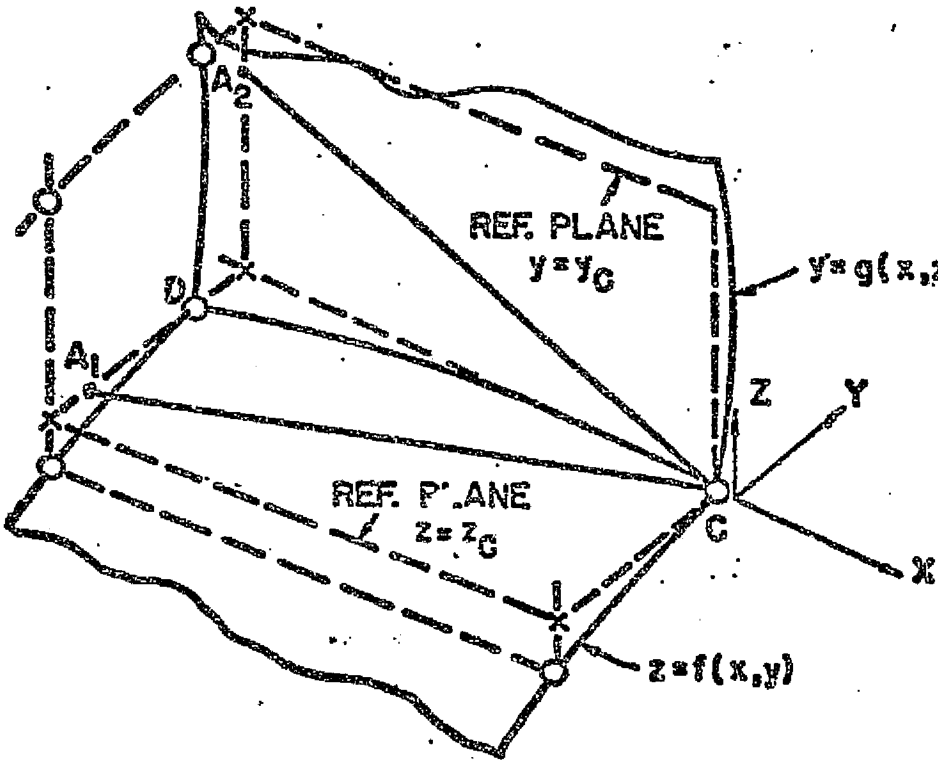

FIGURE 19. INTERNAL CORNER CALCULATION, CARTESIAN SYSTEM

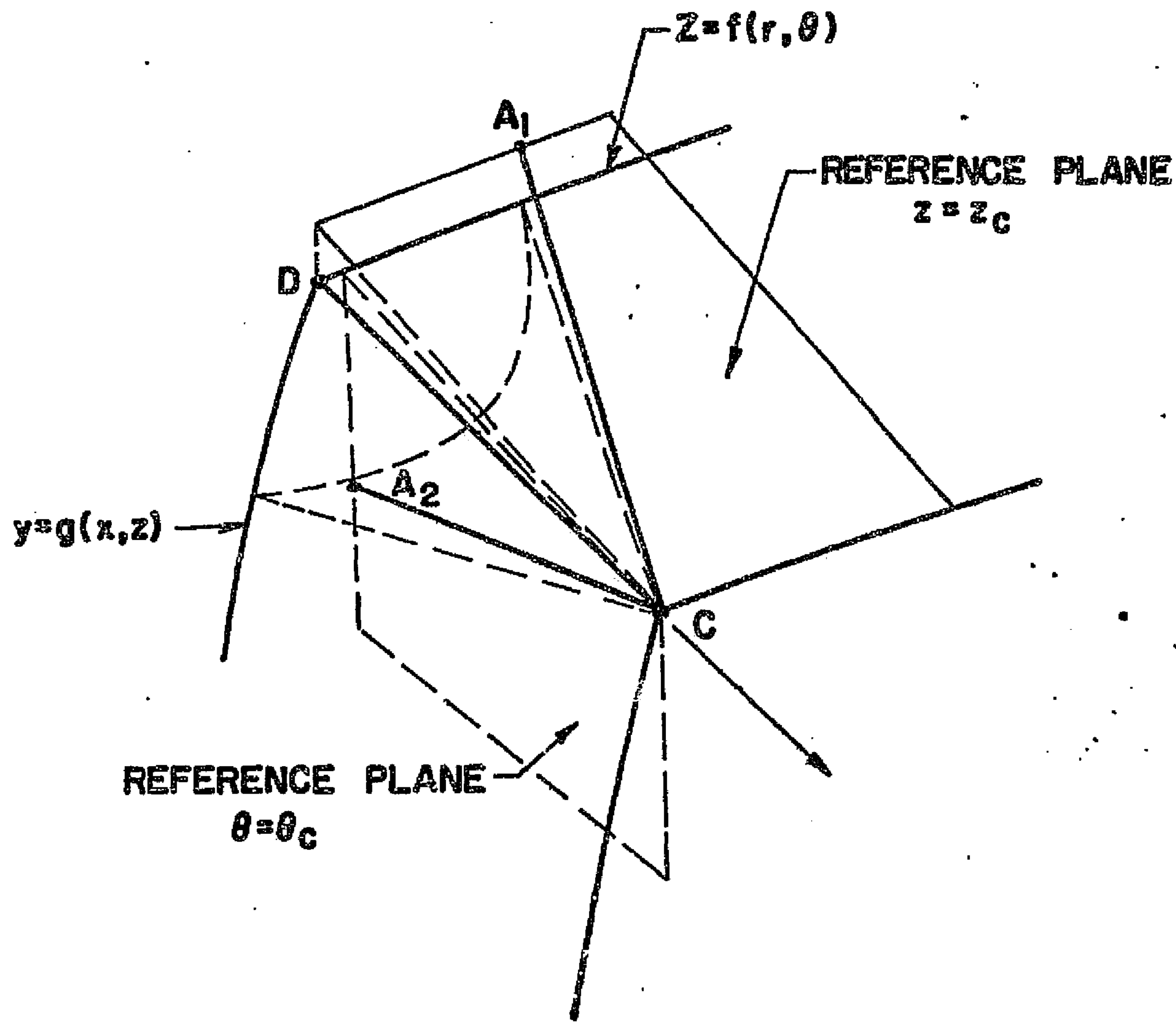

FIGURE 20. INTERNAL CORNER CALCULATION, LINE SOURCE SYSTEM

in the reference plane $\theta = \theta_c$, and the relation

$$\frac{\bar{v}}{\bar{u}} = \frac{g_x + [\cos\theta\, f_r - \sin\theta\, \frac{f\theta}{r}]\, g_z}{1 - [\sin\theta\, f_r + \cos\theta\, \frac{f\theta}{r}]\, g_z} \tag{57}$$

with respect to a cartesian system ($y = y_c$).

For a cylindrical system, the upper or lower wall is specified by an equation of the form $r = f(x,\theta)$ while the sidewall by $\theta = g(x,r)$. Expression of the boundary conditon $\bar{V}\cdot\hat{n} = 0$ on both surfaces at point C results in

$$\tan\phi_c = \left(\frac{w}{u}\right)_c = \frac{f_x + g_x \frac{f\theta}{r}}{1 - g_r \frac{f\theta}{r}} \tag{58}$$

and

$$\left(\frac{v}{u}\right)_c = \frac{g_x + f_x\, g_r}{1 - \frac{f\theta}{r}\, g_r} \tag{59}$$

In all systems, the pressure P_c is determined via the weighted characteristic technique, while streamline relations, applied along the corner streamline CD, are employed to generate remaining flow variables.

E. Calculation of Three-Dimensional Surfaces of Discontinuity - The numerical models described treat the plume interface (separating the nozzle exhaust flow from the vehicle external flow) and plume generated external shock wave as discrete surfaces of discontinuity. The overall approach closely follows that of Reference (4) and thus is summarized briefly in this report.

The orientation of a surface of discontinuity with respect to the x_1, x_2, x_3 coordinate system is depicted in Figure (21). The local surface orientation is specified by an ortho-normal triad of vectors consisting of the normal to the surface and two surface tangent vectors. With respect to the reference plane x_2 = constant, a tangent direction $\hat{t}$ with cosine director β is defined by the shock and reference plane intersection. The surface tangent $\hat{\ell}$ with cosine director α is normal to $\hat{t}$ and thus the normal to the shock $\hat{n}$ is given by the cross product $\hat{n} = \hat{t} \times \hat{\ell}$, which in terms of α and β may be written

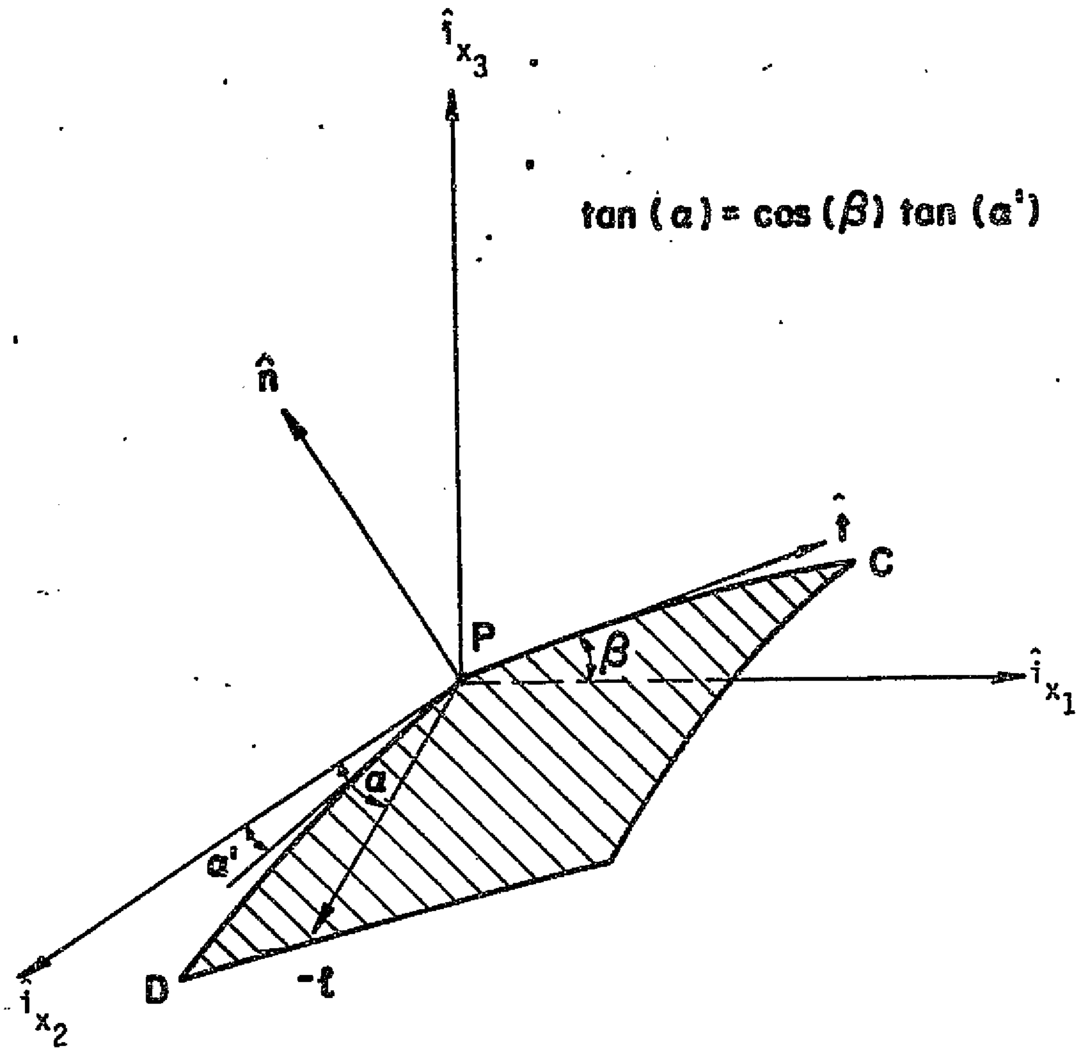

FIGURE 21. ORIENTATION OF DISCONTINUITY SURFACES

$$\hat{n} = -\cos\alpha \sin\beta \; \hat{i}_{x_1} - \sin\alpha \; \hat{i}_{x_2} + \cos\alpha \cos\beta \; \hat{i}_{x_3} \tag{60}$$

The cross cast angle α', made by the cut of the discontinuity surface with the plane x_1 = constant and the x_2 coordinate direction, is related to the angles α and β by the relation

$$\tan\alpha' = \tan\alpha/\cos\beta \tag{61}$$

Shock Point

For the calculation of a shock point, the local velocity vector expressed in the shock oriented system may be written

$$\bar{V} = \tilde{u}\hat{n} + \tilde{v}_t\hat{t} + \tilde{v}_\ell\hat{\ell} \tag{62}$$

and the Rankine-Hugoniot jump relations in this shock normal system are:

Continuity

$$\rho_1 \tilde{u}_1 = \rho_2 \tilde{u}_2 \tag{63}$$

Normal Momentum

$$P_1 + \rho_1 \tilde{u}_1^2 = P_2 + \rho_2 \tilde{u}_2^2 \tag{64}$$

$\hat{t}$ Momentum

$$\tilde{v}_{t_1} = \tilde{v}_{t_2} \tag{65}$$

$\hat{\ell}$ Momentum

$$\tilde{v}_{\ell_1} = \tilde{v}_{\ell_2} \tag{66}$$

Energy

$$H = \text{constant} = h+\tfrac{1}{2} V^2 \tag{67}$$

State

$$\rho = \rho\ (P,h,\Phi) \tag{68}$$

where points 1 and 2 are respectively upstream and downstream of the shock. Combining and rewriting Equation (63) and Equation (64) in terms of the angles α and β and velocity, expressed by q, ϕ and ψ, one obtains

Continuity and $\hat{n}$ Momentum

$$\rho_1\ \tilde{u}_1\ (\tilde{u}_1 - \tilde{u}_2) = P_2 - P_1 \tag{69}$$

where

$$\tilde{u} = q[\tan\psi \sin\alpha + \cos\alpha \sin(\beta-\phi)]$$

$\hat{t}$ Momentum

$$q_1\ \cos(\beta-\phi_1) = q_2\ \cos(\beta-\phi_2) \tag{70}$$

$\hat{\ell}$ Momentum

$$q_1(-\sin\alpha \sin(\beta-\phi_1) + \cos\alpha\ \tan\psi_1) = q_2(-\sin\alpha \sin(\beta-\phi_2) + \cos\alpha\ \tan\psi_2) \tag{71}$$

Energy

$$H_2 = h_2 + \tfrac{1}{2}\ (q_2/\cos\psi_2)^2 = \text{constant} \tag{72}$$

State

$$\rho_2 = \rho(P_2,\ h_2,\ \Phi) \tag{73}$$

Referring to Figure (22), illustrating the local finite-difference network in the line source system, shock point C is calculated as follows:

(1) In each reference plane J, point C is located by the relation

$$\frac{h_3}{h_1}\left(\frac{dx_3}{dx_1}\right)_{sh} = \tan\beta_i \tag{74}$$

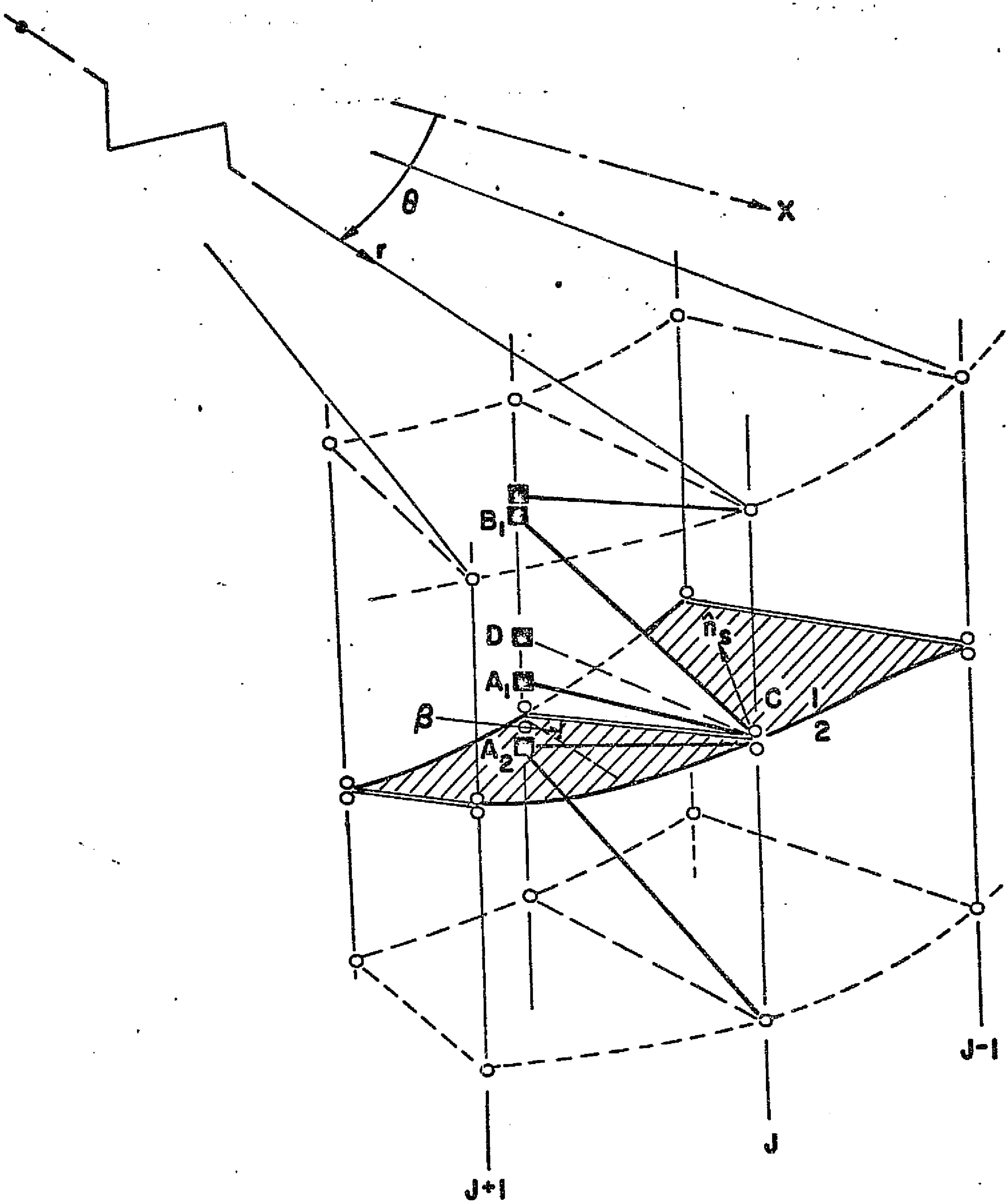

FIGURE 22. TYPICAL SHOCK WAVE CALCULATION

where β_i is the shock angle in the reference plane at the preceding step. Having located points x_{3_c} in adjacent reference planes J - 1 and J + 1, the cross cut angle α' is calculated by the relation

$$\tan\alpha'_c = \frac{h_3}{h_2} \frac{(x_{3_{c_{J+1}}} - x_{3_{c_{J-1}}})}{2\,\Delta x_2} \tag{75}$$

for reference planes equally spaced at intervals of Δx_2.

(2) Properties at C_1 are evaluated by a standard reference plane characteristic procedure. Note that the position of C remains invariant in this calculation procedure and thus properties may be evaluated at both the predictor and corrector level. Points A_1 and B_1 (Figure 22) are the intersections of the reference plane characteristics passing through C_1 with the initial data surface.

(3) A value of the shock angle in the reference plane, β_c, is assumed, yielding α_c via Equation (61).

(4) The Rankine-Hugoniot relations (Equations 69 - 73) yield properties q, ϕ, ψ, P and ρ at C_2.

(5) The compatibility relation applied along the uprunning characteristic A_2C_2 with $\phi = \phi_{c_2}$ and coefficients averaged yields an alternate value of pressure $\tilde{P}_{c_2}$.

(6) The angle β_c is perturbed and steps (3) and (5) are repeated until the pressures P_{c_2} and $\tilde{P}_{c_2}$ are in agreement to within a specified tolerance. Linear error extrapolations are employed to speed convergence.

(7) Having converged in each reference plane J, the following global iterative procedure may be employed although the additional accuracy provided by these additional steps has not been ascertained.

ORIGINAL PAGE IS
OF POOR QUALITY

(a) Evaluate cross derivatives $\partial/\partial x_2$ at points C_2 and incorporate their values into the forcing function terms of the compatibility relations along A_2C_2. Although coefficients were averaged in this relation, forcing function terms were evaluated based on cross derivative values at A_2.

(b) Relocate the points x_{3_c} replacing $\tan\beta_i$ of Equation (74) with $\frac{1}{2}[\tan\beta_i + \tan\beta_c]$, in each reference plane J. Then, the cross cut angles α' must also be reevaluated via Equation (75).

(c) Repeat steps (2) through (6) in each reference plane J with the initial estimate of β_c being the converged value from the first global iteration.

Contact Point

The contact point calculational procedure is substantially more complex than its two-dimensional counterpart since the streamlines passing through a point on either side of the contact discontinuity not only differ in the values of composition and stagnation properties, but also may be highly skewed with respect to each other. Thus, as for a solid boundary, the angle made by the cut of the contact surface with the reference plane differs from the streamline projection onto the reference plane. Referring to Figure (23) illustrating the local surface geometry, the streamline passing through point C on the upper side (side 2) of the contact surface is the line $D_2^* C_2$ while that through the lower side (side 1) is the line $D_1^* C_1$. The angle β is the angle made by the contact surface intersection with the reference plane x_2 = constant while α' is the cross cut angle. Geometric relations are those presented above. A local iterative procedure in each reference plane, analogous to that for the shock point calculation is performed to satisfy the boundary conditions:

$$(\bar{V}\cdot\hat{n})_{c_1} = (\bar{V}\cdot\hat{n})_{c_2} = 0 \tag{76a}$$

$$P_{c_1} = P_{c_2} \tag{76b}$$

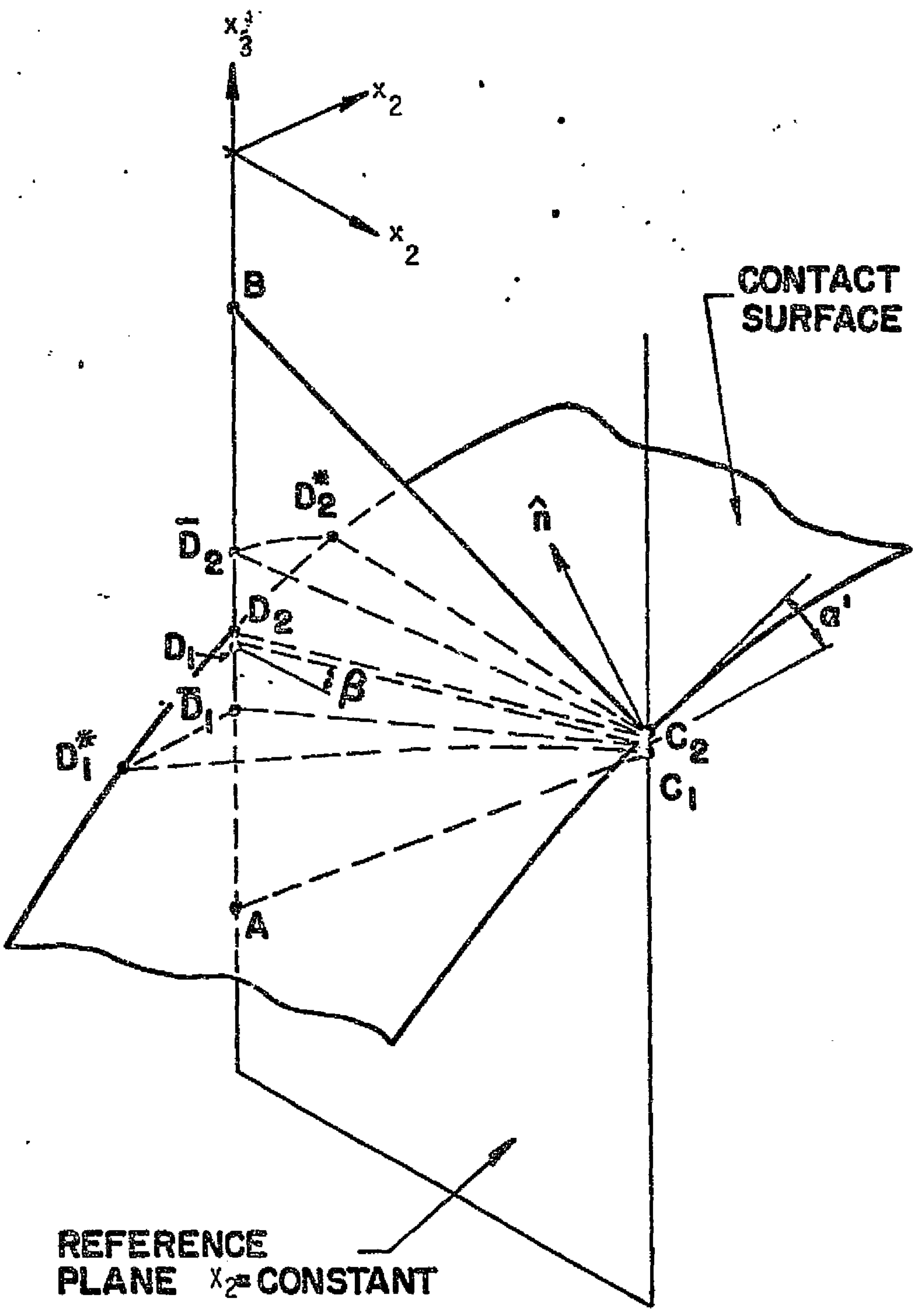

FIGURE 23. TYPICAL CONTACT SURFACE CALCULATION

The computational procedure may be summarized as follows:

(1) Points x_{3_c} are located in each reference plane J via Equation (74) while cross cut angles α' are obtained via Equation (75).

(2) A value of β_c is assumed yielding α_c via Equation (61) and an expression of the boundary condition $\bar{V}\cdot\hat{n} = 0$ (Equation 76a) in the form

$$\sin(\beta_c - \phi_{c_{1,2}}) + \tan\alpha_c \tan\psi_{c_{1,2}} = 0 \tag{77}$$

(3) The standard solid surface calculational procedure (Section IIIC) in conjunction with Equation (77) yields values of P, ϕ and ψ at points c_1 and c_2 for the assumed value of β_c.

(4) The angle β_c is perturbed and steps (2) and (3) are repeated until the pressures P_{c_1} and P_{c_2} agree to within a specified tolerance. Linear error extrapolations are again employed to speed convergence.

(5) Upon convergence in each reference plane J, the global iterative procedure employed for the shock may be employed with cross derivatives $\partial/\partial x_2$ now evaluated along grid points c_1 and c_2.

F. Cowl Lip Exhaust/External Flow Interaction - At the cowl lip, the inviscid interaction between the nozzle exhaust flow and external stream is discretely analyzed establishing the initial geometry of the contact surface separating these streams. For underexpanded flows, this interaction results in an expansion fan propagating towards the vehicle undersurface and a plume generated bow shock as schematized in Figure (24). The calculation of this interaction is simplified by recognizing that the flow phenomena is locally two-dimensional in planes normal to the cowl trailing edge. Figure (25) depicts the coordinate system associated with this local normal plane. By transforming data to this coordinate system, standard two-dimensional procedures are employed in determining the contact angle $\bar{\beta}$ which yields a pressure balance

TYPICAL REFERENCE PLANE

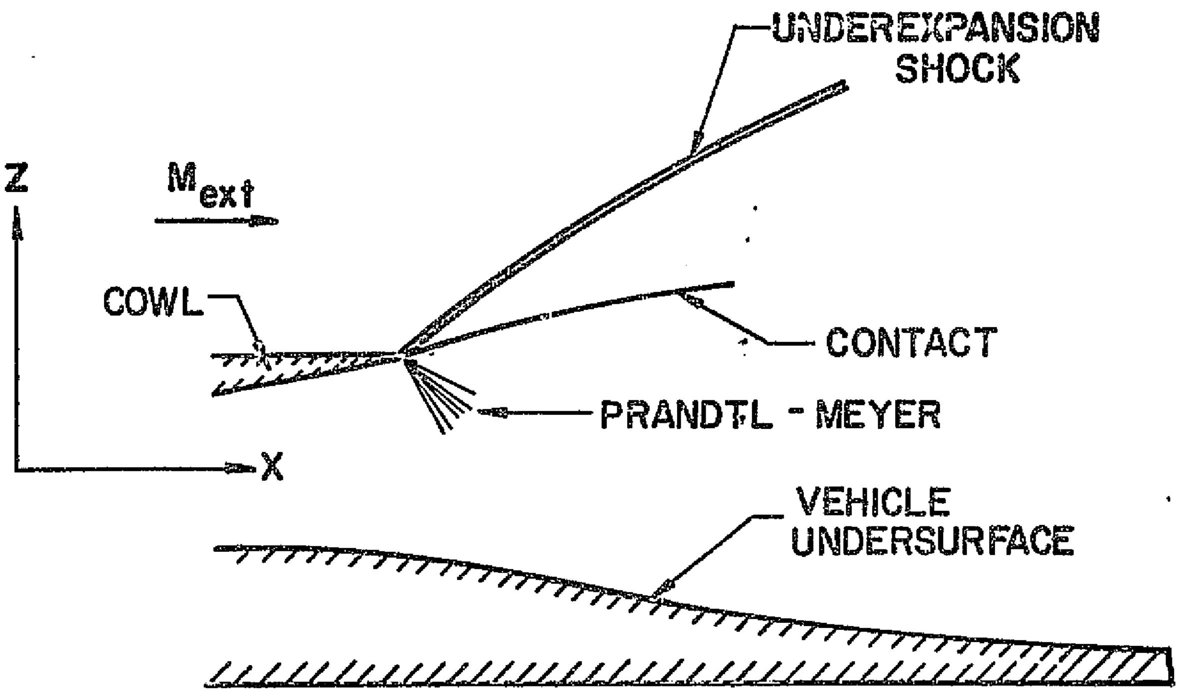

FIGURE 24. UNDER-EXPANSION INTERACTION

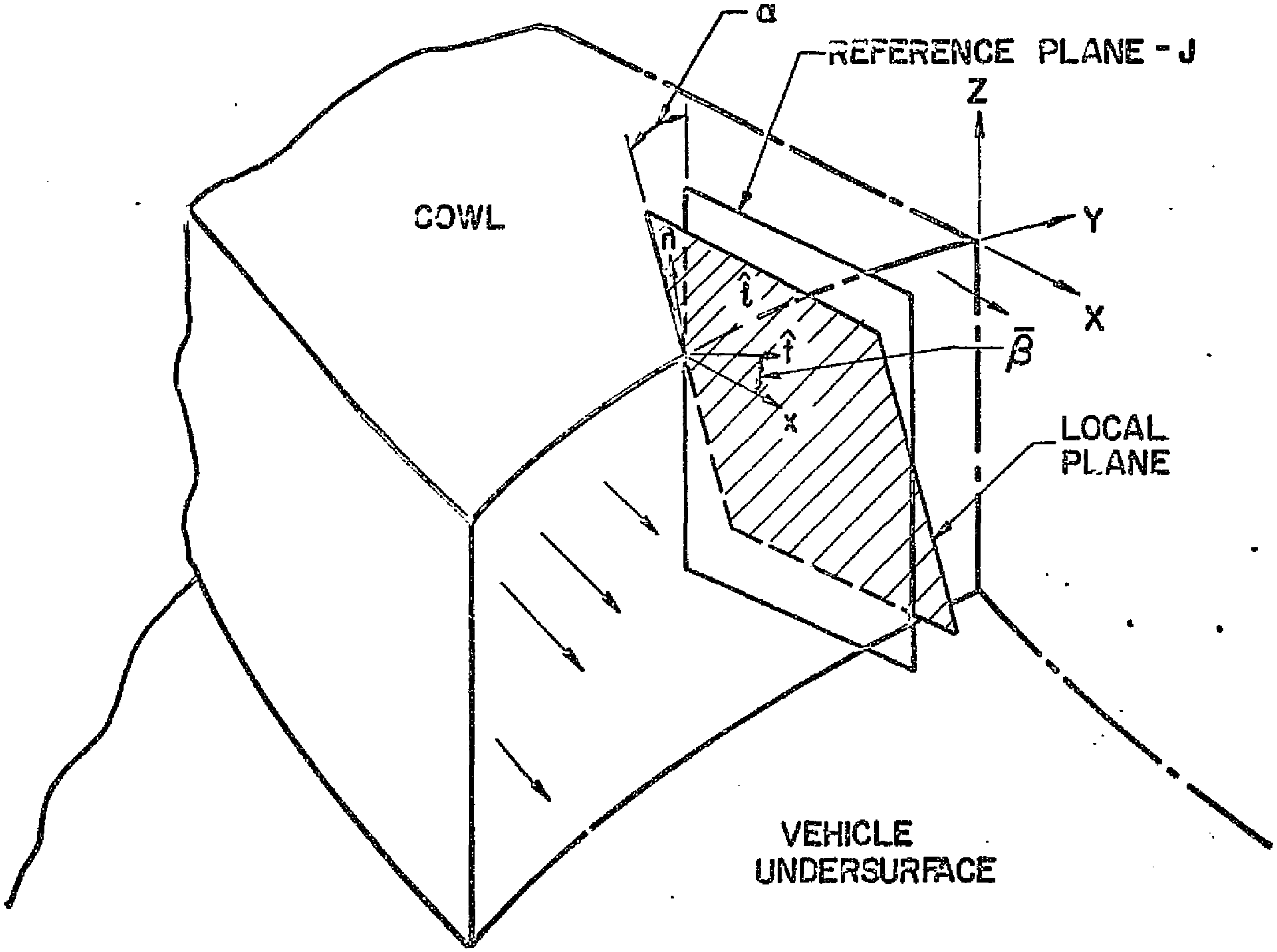

FIGURE 25. LOCALLY ORIENTED SYSTEM FOR EXHAUST/EXTERNAL FLOW INTERACTION.

between the exhaust flow and external stream.

For a non-swept cowl trailing edge, the local unit vectors are obtained via the transformation

$$\begin{pmatrix} \hat{n} \\ \hat{\ell} \\ \hat{t} \end{pmatrix} = A \begin{pmatrix} \hat{i}_{x_1} \\ \hat{i}_{x_2} \\ \hat{i}_{x_3} \end{pmatrix} A = \begin{pmatrix} \sin\bar{\beta} & -\cos\bar{\beta}\sin\alpha & \cos\bar{\beta}\cos\alpha \\ 0 & \cos\alpha & \sin\alpha \\ \cos\bar{\beta} & -\sin\bar{\beta}\sin\alpha & \sin\bar{\beta}\cos\alpha \end{pmatrix} \tag{78}$$

where, referring to Figure (26), $\hat{\ell}$ is the unit vector tangent to the cowl trailing edge and $\hat{n}$ is normal to the discontinuity surface at the trailing edge. The angle α is the cross cut angle made by the cowl trailing edge with the x_2 coordinate direction, while β is an angle made by the cut of the discontinuity surface with the reference plane x_2 = constant. The angle $\bar{\beta}$ is the cut of this discontinuity surface with the local normal plane and is related to α and β by the expression

$$\tan\bar{\beta} = \cos\alpha\tan\beta \tag{79}$$

The iterative process is initiated by transforming the velocity components to cowl oriented coordinates where $\hat{n}$ is identified as the unit normal to the inner cowl surface at the trailing edge.* The initial velocity of the exhaust flow in this system is expressed by

$$\bar{V} = \tilde{u}\hat{n} + \tilde{v}\hat{\ell} + \tilde{w}\hat{t} \tag{80}$$

where the components $\tilde{u}$, $\tilde{v}$ and $\tilde{w}$ are obtained via the transformation

---

*For a cowl surface specified by the relation $z = f(x,y)$, $\bar{\beta}$ is given by

$$\bar{\beta} = \tan^{-1}\left(\frac{f_x^2}{1 + f_y^2}\right)^{\frac{1}{2}}$$

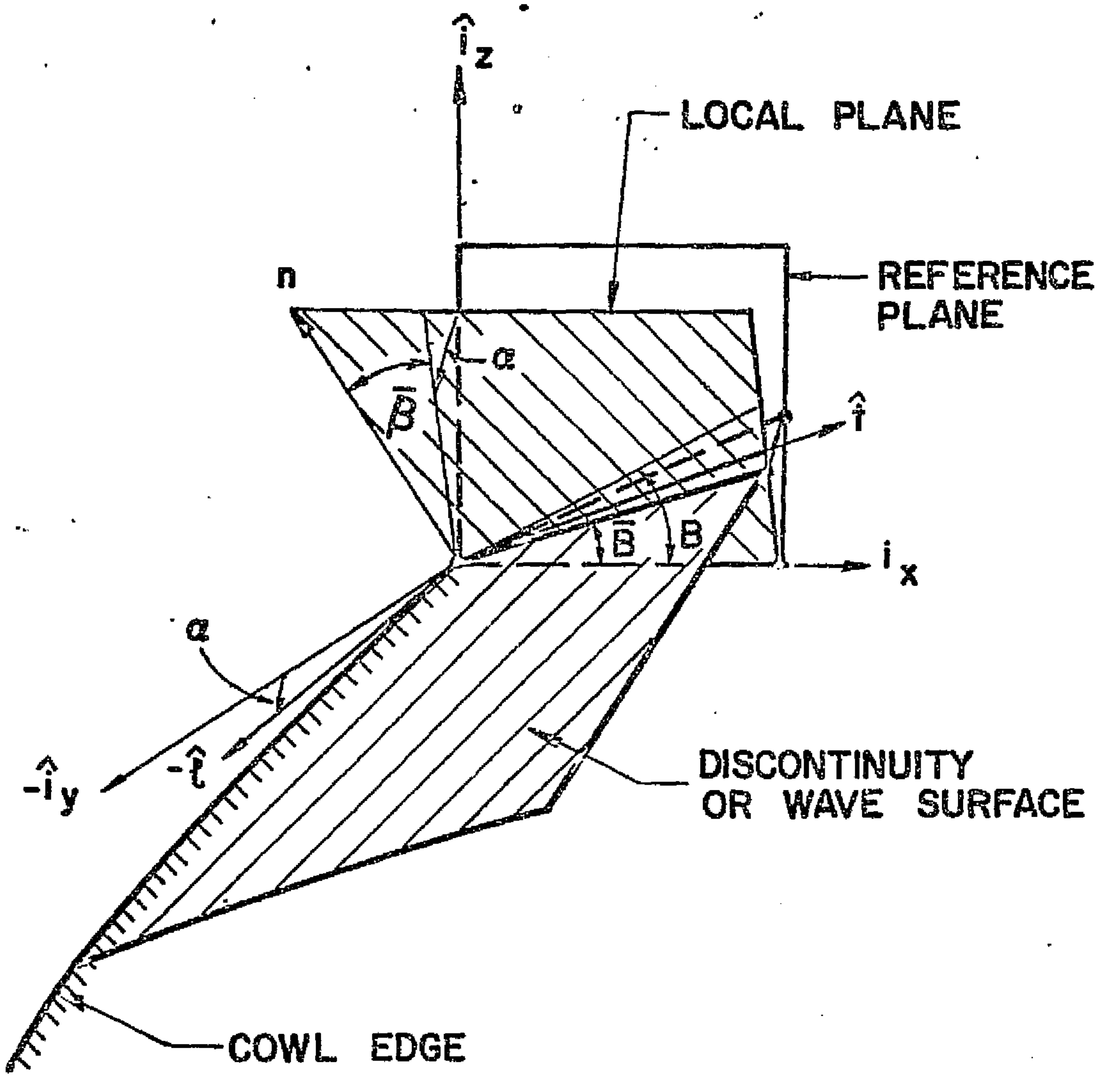

FIGURE 26. EXTERNAL FLOW INTERACTION-LOCAL AND REFERENCE PLANE ORIENTATION

$$\begin{pmatrix} \tilde{u} \\ \tilde{v} \\ \tilde{w} \end{pmatrix} = A \begin{pmatrix} u \\ v \\ w \end{pmatrix}$$

The Mach number projection onto the local normal plane, used to initiate the Prandtl-Meyer integration, is expressed by

$$M_i^2 = (\tilde{u}^2 + \tilde{w}^2)/a^2$$

Then, the interface angle $\bar{\beta}$ is incremented in small steps of $\Delta\bar{\beta}$, where for each step i the following procedure is followed:

(1) The pressure on the interface is determined via the relation

$$\ell n\ P_i = \ell n\ P_{i-1} - \left(\Gamma \frac{M^2}{\sqrt{M^2-1}} \right)_{i,i-1} \Delta\bar{\beta} \tag{81}$$

where $\bar{\beta}_i = \bar{\beta}_i + (i-1)\ \Delta\bar{\beta}$ and subsequent projected Mach numbers are obtained by a standard isentropic relation.

(2) The pressure jump across the bow shock wave is determined in correspondence with the change in flow deflection angle in the local normal plane as expressed by

$$\delta_{sh} = \cos^{-1} (\hat{n}_w \cdot \hat{n}_c) \tag{82}$$

where $\hat{n}_w$ is the unit normal to the outer cowl surface while $\hat{n}_c$ is the normal to the contact surface as expressed by Equation (78) with $\bar{\beta} = \bar{\beta}_i$.

(3) The shock angle $\bar{\beta}_s$ is determined via the relation (for a perfect gas)

$$\cot\delta_{sh} = \tan\bar{\beta}_s \left[\frac{(\gamma+1)\ \tilde{M}_e^2}{2(M_e^2 \sin^2\beta_s - 1)} - 1 \right] \tag{83}$$

ORIGINAL PAGE IS OF POOR QUALITY

where $\tilde{M}_E^2$ is the external stream Mach number projected onto the local normal reference plane as given by

$$\tilde{M}_E^2 = (\tilde{u}_E^2 + \tilde{w}_E^2)/a_f^2 \tag{84}$$

where the velocity components $\tilde{u}_E$ and $\tilde{w}_E$ are obtained via the transformation of Equation (80) identifying $\bar{\beta}$ in matrix A with expressions of the normal to the outer cowl surface.

(4) The pressure on the external side of the interface associated with the change in flow deflection angle δ_{sh} and shock angle $\bar{\beta}_s$ is given by

$$P_{s_i} = P_E + \frac{2\gamma M_E^2 \sin^2\bar{\beta}_s - (\gamma-1)}{(\gamma+1)} \tag{85}$$

(5) The process is repeated until $P_{s_i} \leq P_i$; then properties are obtained by linearly interpolating between values at the last two iterations.

(6) Resultant velocities in the local normal system are transformed back to standard reference plane components via the inverse transformation

$$\begin{pmatrix} u \\ v \\ w \end{pmatrix} = A^{-1} \begin{pmatrix} \tilde{u} \\ \tilde{v} \\ \tilde{w} \end{pmatrix}$$

G. External Corner - End Module Calculational Procedures - For an end module, the local exhaust/external flow interaction processes at the trailing edge occur in mutally perpendicular planes. To best accommodate the plume flowfield calculations in this vicinity, a combination of reference plane systems is employed. For the rectangular end module schematized in Figure (27), vertical reference planes (y=constant) are employed in the central region while horizontal reference planes (z=constant) are used in the vicinity of the module sidewall. A cylindrical "wraparound" reference plane system is employed in the region of the corner to provide for the transition between these two systems. Implementation of this hybrid grid system provides reference plane alignment essentially perpendicular to predominant wave and discontinuity surfaces as well as to the vehicle undersurface.

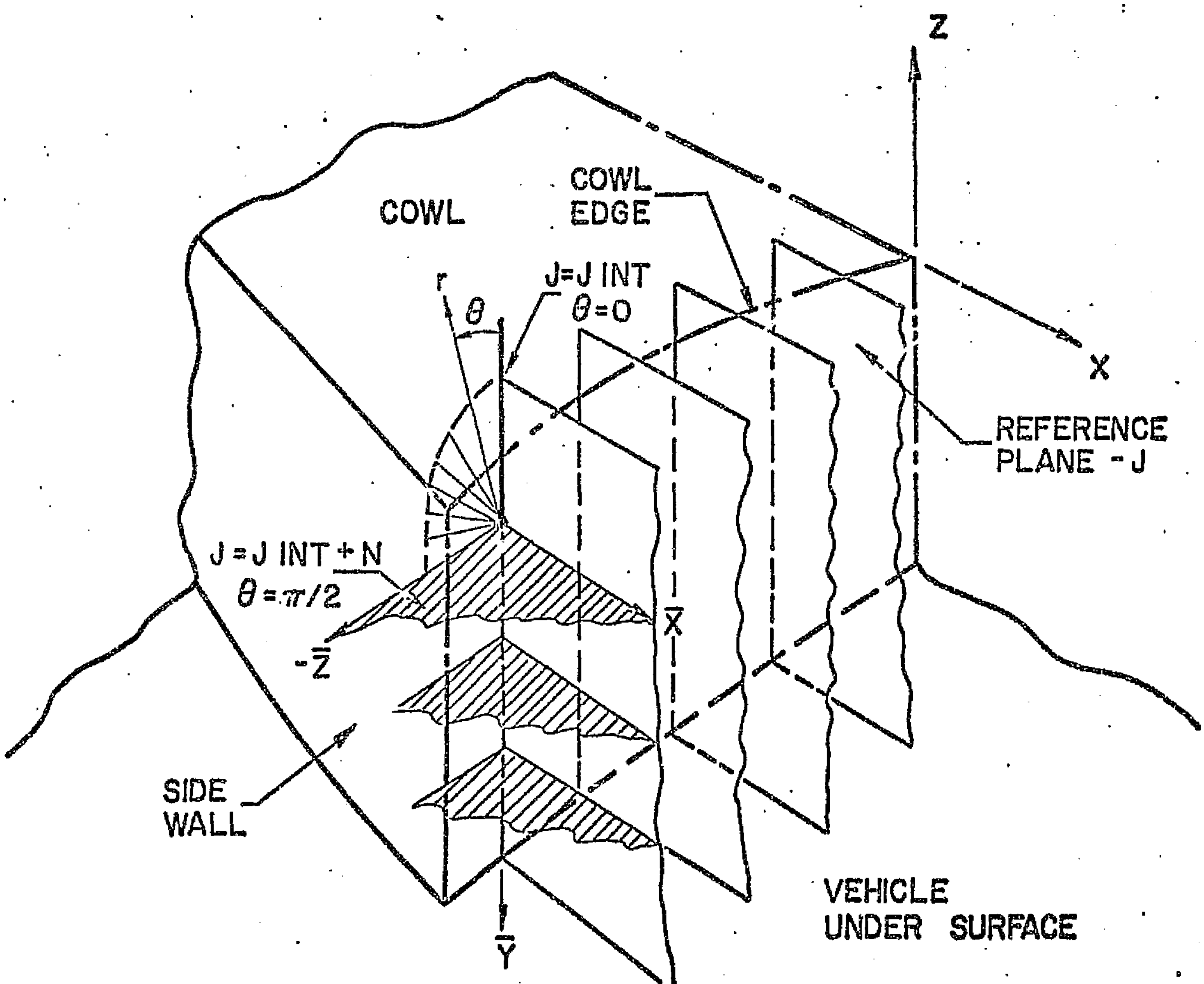

FIGURE 27. EXTERNAL CORNER REGION

The details of the interaction process in the corner region are depicted in Figure (28). For the simple corner comprised of the intersection of the surfaces z = constant (cowl) and y = constant (sidewall) with uniform internal and external flowfields, the following two-dimensional regions may be identified, for an underexpanded exhaust:

(1) A cowl interaction region resulting in an interface deflection angle δ_1, a bow shock angle τ_1 and uniform pressure P_{2D} (cowl) extending from the bow (external) shock to the terminating ray of the Prandtl-Meyer expansion fan emanating from the cowl.

(2) A sidewall interaction region having corresponding interface an shock angles δ_2 and τ_2 respectively and region of uniform pressure P_{2D}(SW).

Both these two-dimensinal regions occur outside the domain encompassed by the Mach cone enamating from the juncture of the cowl and sidewalls at the trailing edge. The region outside the intersection of the two Prandtl-Meyer fans emanating from the cowl and sidewalls remains undisturbed while the region within the intersection of these expansion fans is highly three-dimensional. Numerical solutions for internal and external corners have been performed exploiting the conical invariance of such flowfields (Reference 16). A comparison of such internal corner solutions with those obtained by BIGMAC and CHAR3D, employing standard boundary calculational procedures, have been demonstrated in Reference (12) and are described in more detail in the next section. Similar comparisons for the substantially more complex underexpanded exhaust/external flow interaction problem pend the availability of solutions by techniques exploiting the ocnical invariance of this flowfield.

Details of the localized grid network in the corner region, for a quiescent external stream, are provided in Figure (29). Each of the three reference plane systems are discretely analyzed employing overlap planes at the boundaries of each system to provide a mechanism for the evaluation of cross derivatives. The grid point located at the origin of the cylindrical wraparound network is calculated in both the vertical and horizontal reference plane systems and the results, averaged. Evaluation of the allowable marching step via the CFL sta-

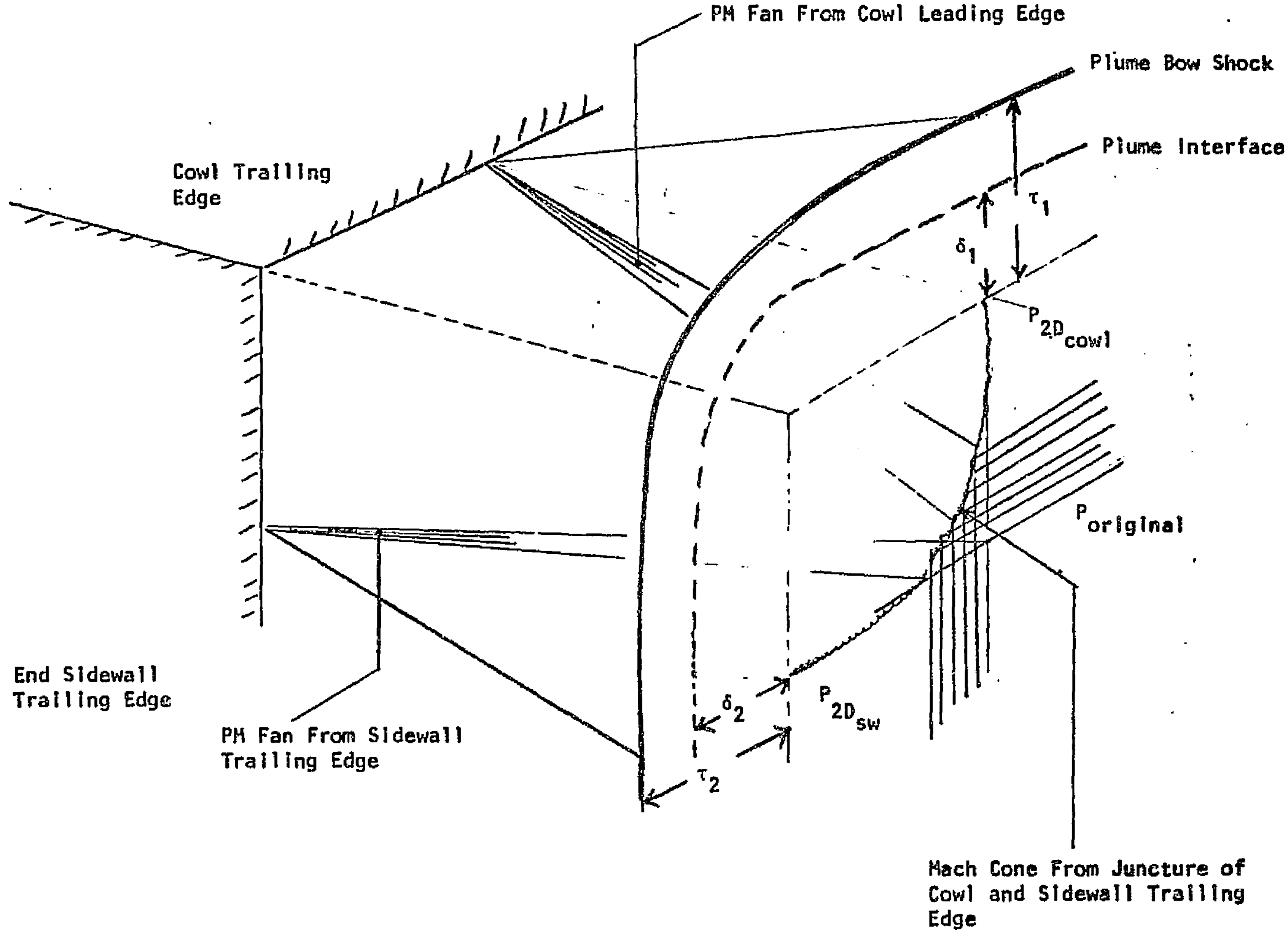

FIGURE 28. UNDEREXPANDED EXHAUST CORNER INTERACTION FLOWFIELD

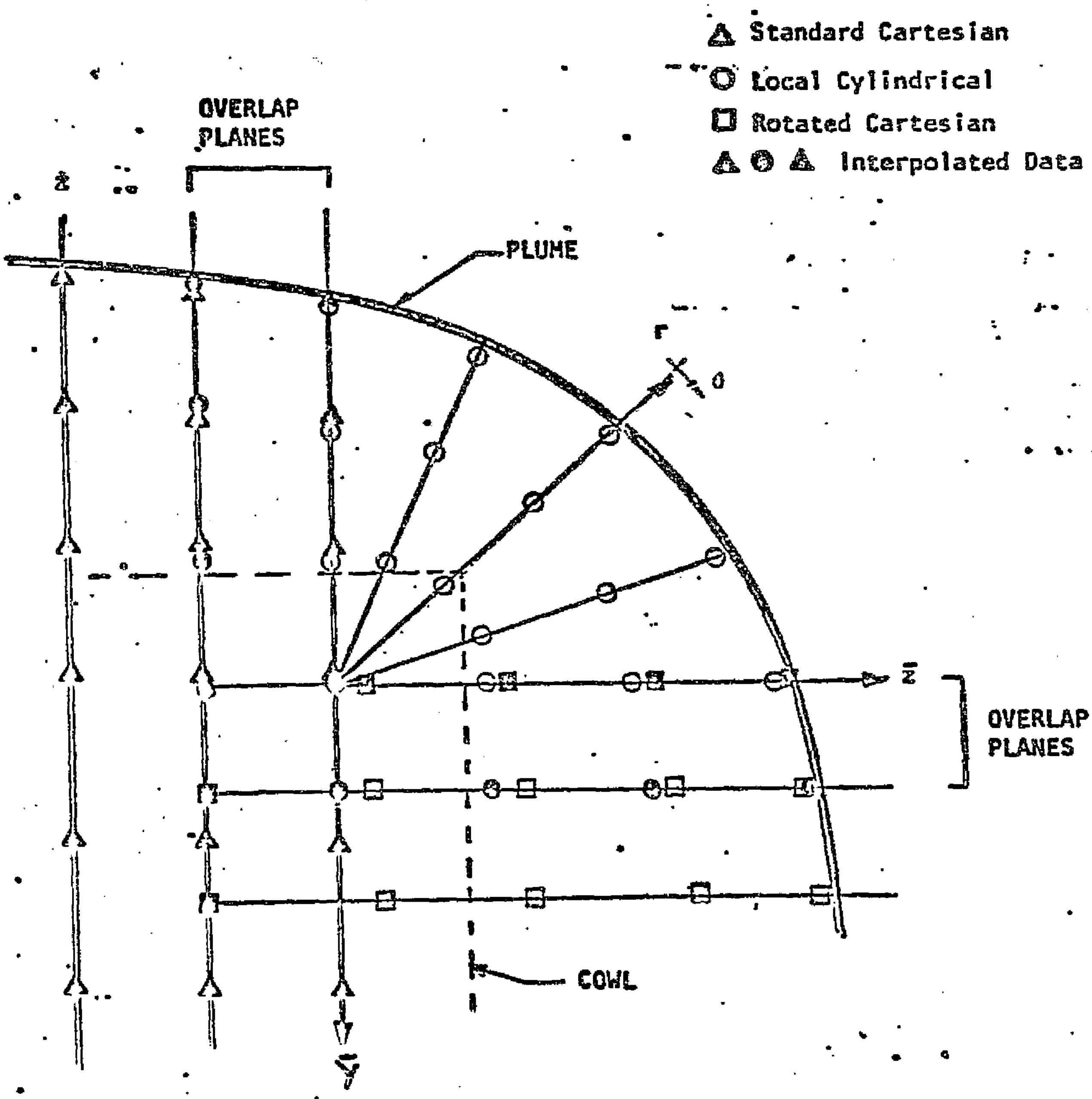

FIGURE 29. GRID NETWORK FOR END MODULE EXHAUST PLUME IN QUIESCENT STREAM

bility criterion does not consider transversal spacing in the cylindrical system, since this would be overly restrictive in the proximity of the origin. Rather, the numerical domain utilized for the evaluation of such cross derivatives is "extended" to encompass grid points outside the intersection of the Mach four cone from the grid point being calculated with the initial data plane, thus ensuring stability.

Rather limited experience in performing such corner calculations has failed to lead to an optimized approach for grid orientation in this region. However, the location of the origin of the cylindrical "wraparound" reference plane system cannot be fixed apriori in a generalized manner catered to a wide class of exhaust/external flow conditions. Rather, the origin must be a "floating" one, which adjusts to the local growth rate of the plume interface both vertically and horizontally such as to best approximate the local radius of curvature in the "wraparound" region. The logic to perform the above has been developed for Program BIGMAC, which of course includes a complete revision of the local corner grid network everytime the origin is revised.

H. Multiple Module Interactions - The numerical models developed analyze the plume interactions associated with exhausts emanating from multiple nozzles separated by common walls, as illustrated in Figure (1). The internal (nozzle) flowfield calculations are performed for each individual module and the resultant exit plane data stored on local files are combined to generate a complete exit plane map of the exhaust flowfield.

The resultant exit plane properties may differ in pressure and stagnation properties from module to module and, a discontinuity in cross flow angle may exist, produced by the finite trailing edge wedge angle in the common walls separating the individual modules. Thus, in addition to the primary interaction between the exhaust flow and external stream (as depicted in Figure 24) a module to module interaction process occurs at the trailing edge of the walls separating adjacent modules, resulting in a wave system propagating predominantly in the spanwise direction. This process is schematized in Figure (30) wherein the wedge induced cross flow shocks interaction with the downrunning Prandtl-Meyer expansion fan and plume induced bow shock in the domain included within

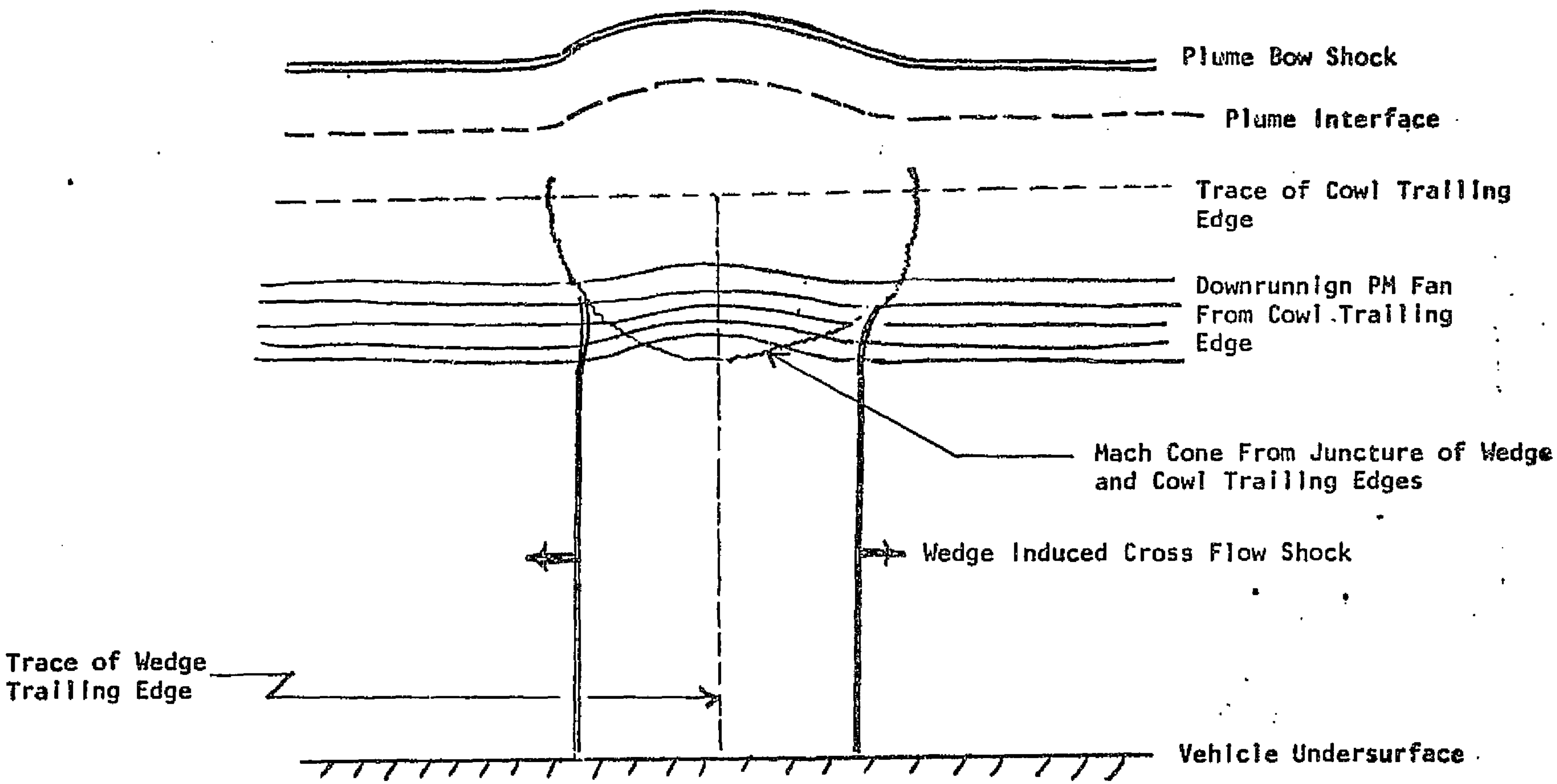

FIGURE 30. INTERMODULE INTERACTIONS

the Mach cone emanating from the juncture of the wedge and cowl trailing edges.

Preliminary results from calculations made in these regions indicate the requirement for maintaining proper grid control and calculating these localized flowfields initially employing a highly refined grid network. In particular, the calculation of these complex interaction regions requires a finite number of integration steps to converge to the conically invariant solution whose boundary conditions are those associated with the flowfield in the immediate vicinity of the wedge/cowl trailing edge juncture. In corporating the calculation of such regions into the numerical codes on a grid scale commensurate with the overall flow domain may result in numerical difficulties attributed to the influx of waves (resulting from nonuniform flowfield properties at the module exit planes) into these regions before convergence has been achieved. Since the convergence process should take place on a length scale which is small in comparison to global inviscid length scales (i.e., module dimensions), the calculation of such interaction regimes seems most readily performed via the performance of a separate, localized calculation. The locally converged results can then be incorporated into the overall grid network as initial conditions made in the same manner that a Prandtl-Meyer expansion solution would be incorporated into a two-dimensional grid network.

IV. SAMPLE CALCULATIONS

A systematic procedure has been followed in assessing the capabilities and limitations of programs BIGMAC and CHAR3D. First, the ability of these codes to capture shock waves and trace their propagation in the reference planes has been evaluated via the performance of a series of two-dimensional calculations in convergent and divergent ducts. Three-dimensional capabilities were then evaluated via the performance of a series of corner calculations for which experimental results and/or conically invariant solutions were available for comparison. The favorable results obtained in these calculations supported useage of these codes in generalized three-dimensional situations.

Results have been obtained with BIGMAC for the flowfield in a rectangular nozzle, demonstrating its ability to calculate the interactions associated with shocks emanating from mutually perpendicular surfaces. Applications to multiple module exhaust flows have indicated the requirement for 1) a refined network in the vicinity of the intersection of the intermodule walls and cowl trailing edge and 2) a floating origin for the wraparound region associated with the end module exhaust flow. A descripton of the calculations performed is provided below.

A. Single Wedge Inlet - Calculations were performed for a 10° wedge inlet having the following uniform entrance conditions:

$$M_1 = 2.94$$

$$P_1 = 845.5$$

$$T_1 = 2328°K$$

$$\gamma = 1.4 = \text{const}$$

(All pressures are nondimensionalized with respect to 47.88 N/m2.)
Results obtained for the upper and lower wall pressure distributions with CHAR3D are displayed in Figure (31) for 11 and 21 point grid networks. In performing these calculations, the grid point on the wedge surface was initialized by conditions behind the wedge shock. Hence, the results were shifted slightly to reflect the uncertainty in shock location between the first and second grid

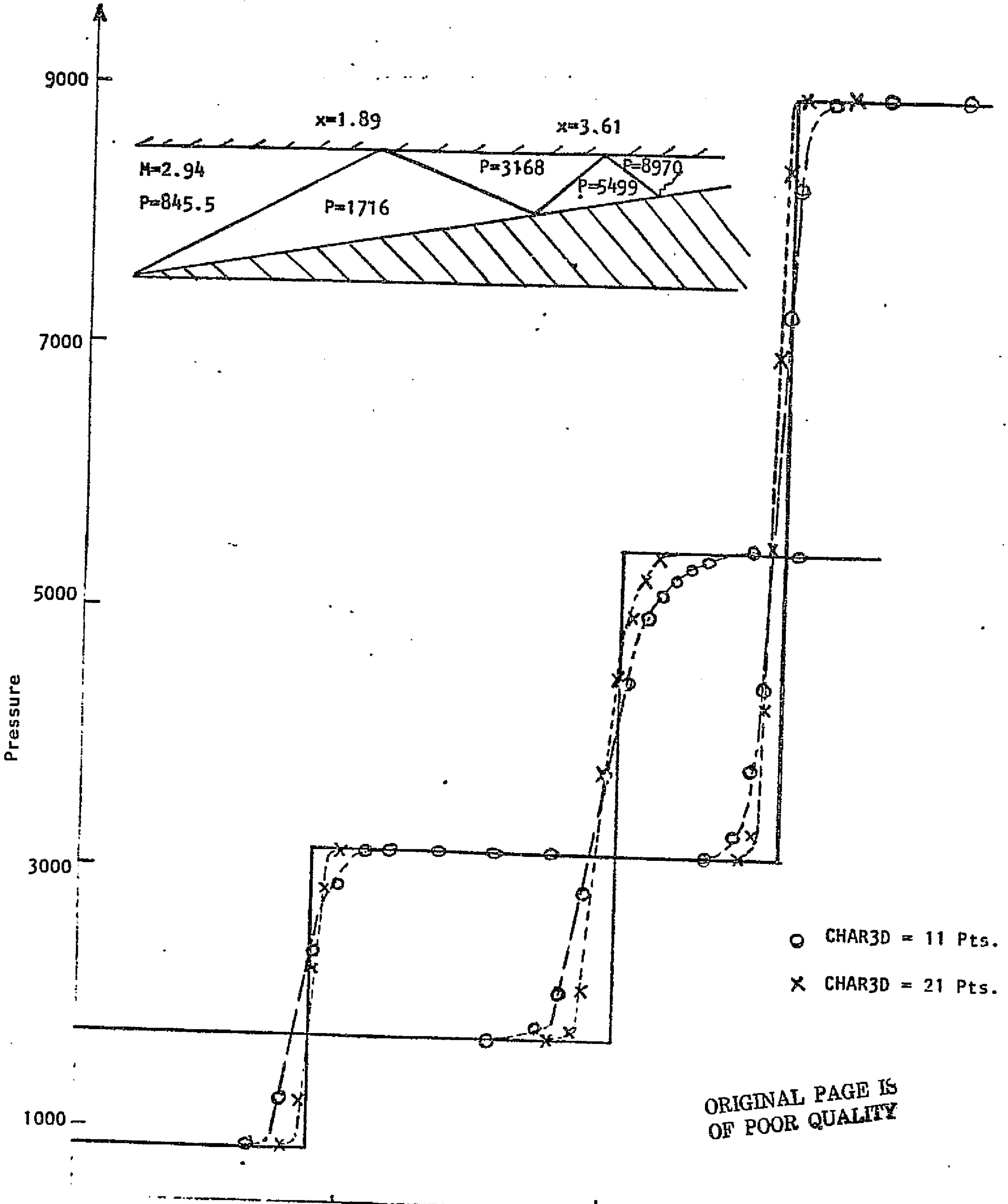

ORIGINAL PAGE IS OF POOR QUALITY

FIGURE 31. SINGLE WEDGE INLET PRESSURE DISTRIBUTIONS - CHAR3D

points. The agreement with the exact solution is quite satisfactory. Shock locations are accurately predicted with a spread over 3 to 5 axial stations at the reflection points and no overshoots are encountered at the shock waves. The results obtained with the 21 point grid provide a somewhat sharper definition of the shock jumps although the 11 point grid is felt to be adequate.

Results obtained with BIGMAC utilizing a 21 point grid are depicted in Figure (32). The three sets of results depicted were obtained employing the predictor/connector algorithm in variant modes. With IFLIP=1, predictive derivatives are made with forward differences while connector derivatives are made with backward differences; with IFLIP= 0 the opposite procedure is followed; while with the FLIP-FLOP procedure the sequence is alternated at successive intergration steps (i.e., IF.IP=1 at odd steps and IFLIP=0 at even steps).

Clear benefits accrue from implementation of the FLIP-FLOP procedure in terms of accurately locating the shock reflection points. The overall accuracy (with the FLIP-FLOP option) is quite comparable to that of CHAR3D. Shock waves appear more sharply defined by BIGMAC although overshoots are encountered at the reflection points. These overshoots are of minimal axial duration and should have a negligible effect on forces and moments.

Subsequent studies, outside of the scope of this effort (i.e, Reference 17, Supersonic Compressor Studies) have indicated that such overshoots are partially attributable to the convergence of streamlines in the reference planes, in regions of large compressions. This convergence also leads to a rather restrictive forward marching step with grid points outside this compressed region being advanced with local Courant numbers substantially less than one. This is reflected in numerically diffusive effects whose buildup can become rather substantial in ducted convergent flows. Elimination of this behavior has been affected by incorporating grid controls in the reference planes; in particular, it was found that grid points in the reference planes should be dropped when they restrict the allowable marching step in comparison to the average allowable step by more than about sixty percent. Implementation of this criterion has substantially improved the performance of these

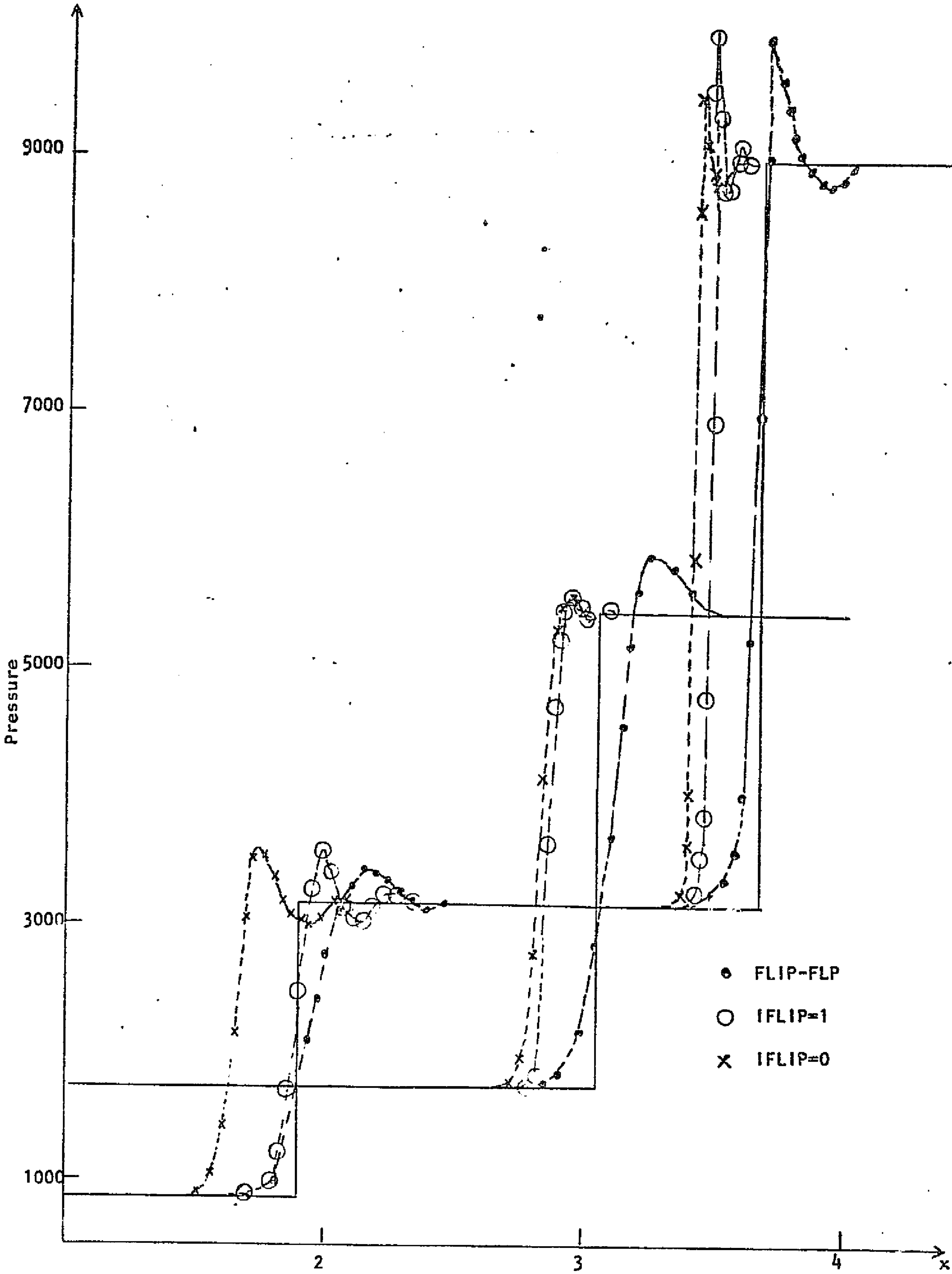

FIGURE 32. SINGLE WEDGE INLET PRESSURE DISTRIBUTIONS - BIGMAC

codes although the results presented herein were performed without this modification.

B. Double Wedge Inlet - Calculations with CHAR3D were performed for the double wedge inlet depicted in Figure (33), having the same uniform entrance conditions as the single wedge inlet case just described. Pressure profiles at x = .64, 1.16 and 2.14 are depicted in Figures (34), (35) and (36), respectively, for both 21 and 41 point grids. The entropy distribution at x = .64 with a 21 point grid is depicted in Figure (37). These calculations further demonstrate the predictive capabilities of CHAR3D for a complex two-dimensional situation involving multiple wall and shock interactions.

C. Two-Dimensional Convergent Duct - Calculations were performed for the duct geometry depcited in Figure (38) and tabulated below, for the same entrance conditions as in the previous calculations.

Lower Surface:

$0 < x < .5; \quad z = 0$
$.5 < x < 1.5; \quad z = .1(x-.5)^2$
$1.5 < x < 2.0; \quad z = .1+.2(x-1.5)$
$2.0 < x < 3.0; \quad z = .2+.2(x-2) - .1(x-2.)^2$
$3.0 < x < 2; \quad z = .3$

Upper Surface:

$x < 0, \quad z = 1.0$

Results obtained with program BIGMAC employing an 11 point grid are depicted in Figures (38) to (41). Results are compared with those of program SEAGULL* employing a 21 point grid and thought to accurately represent the exact solution.

The calculated shock propagation pattern is depicted in Figure (38) for five wall reflections. The upper and lower wall pressure distributions are shown in Figures (39) and (40) respectively, while the upper and lower wall

*Discrete shock code developed by M. Salas at NASA Langley for two-dimensional and axisymmetric internal flows (Reference 18).

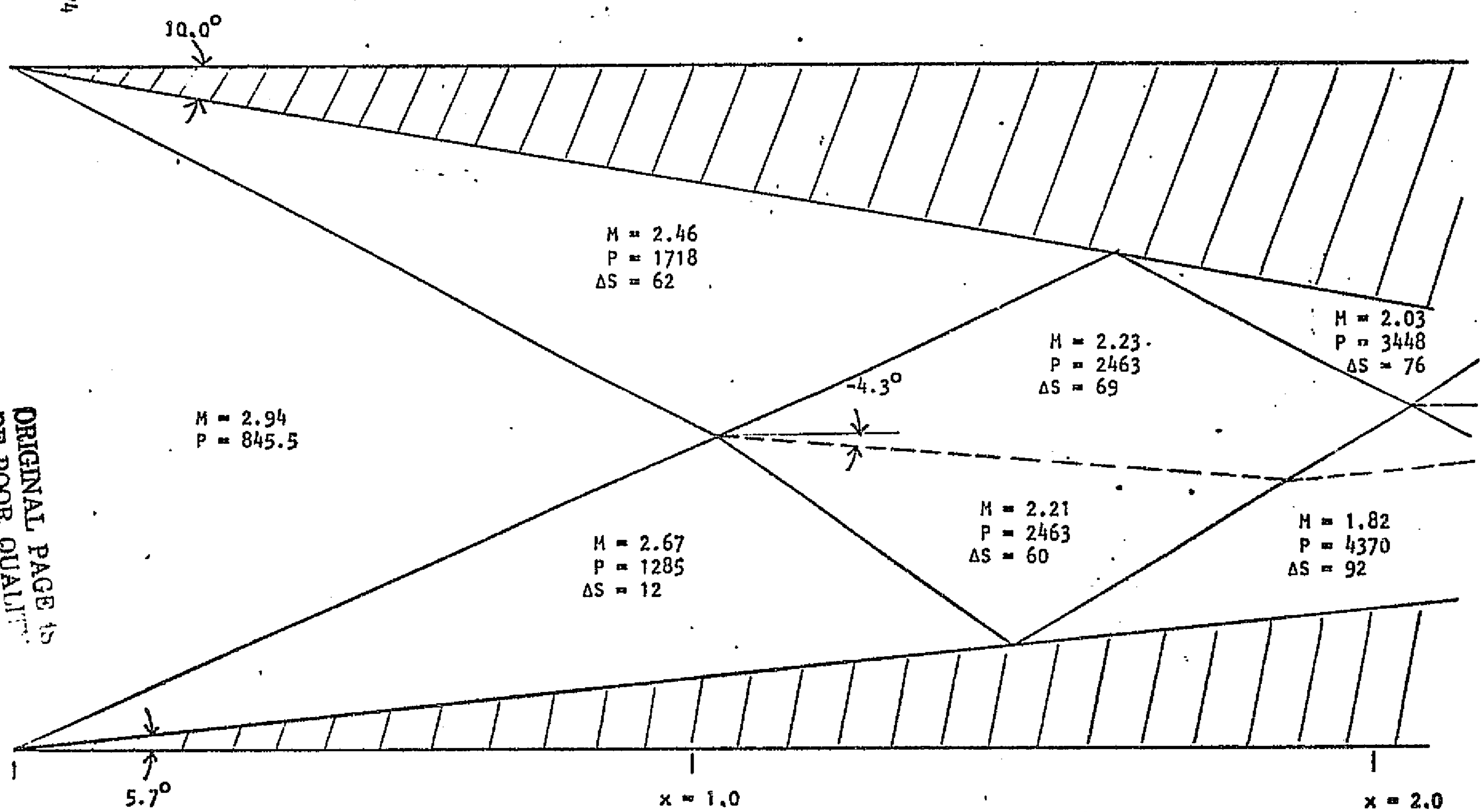

FIGURE 33. DOUBLE WEDGE INLET CONFIGURATIONS

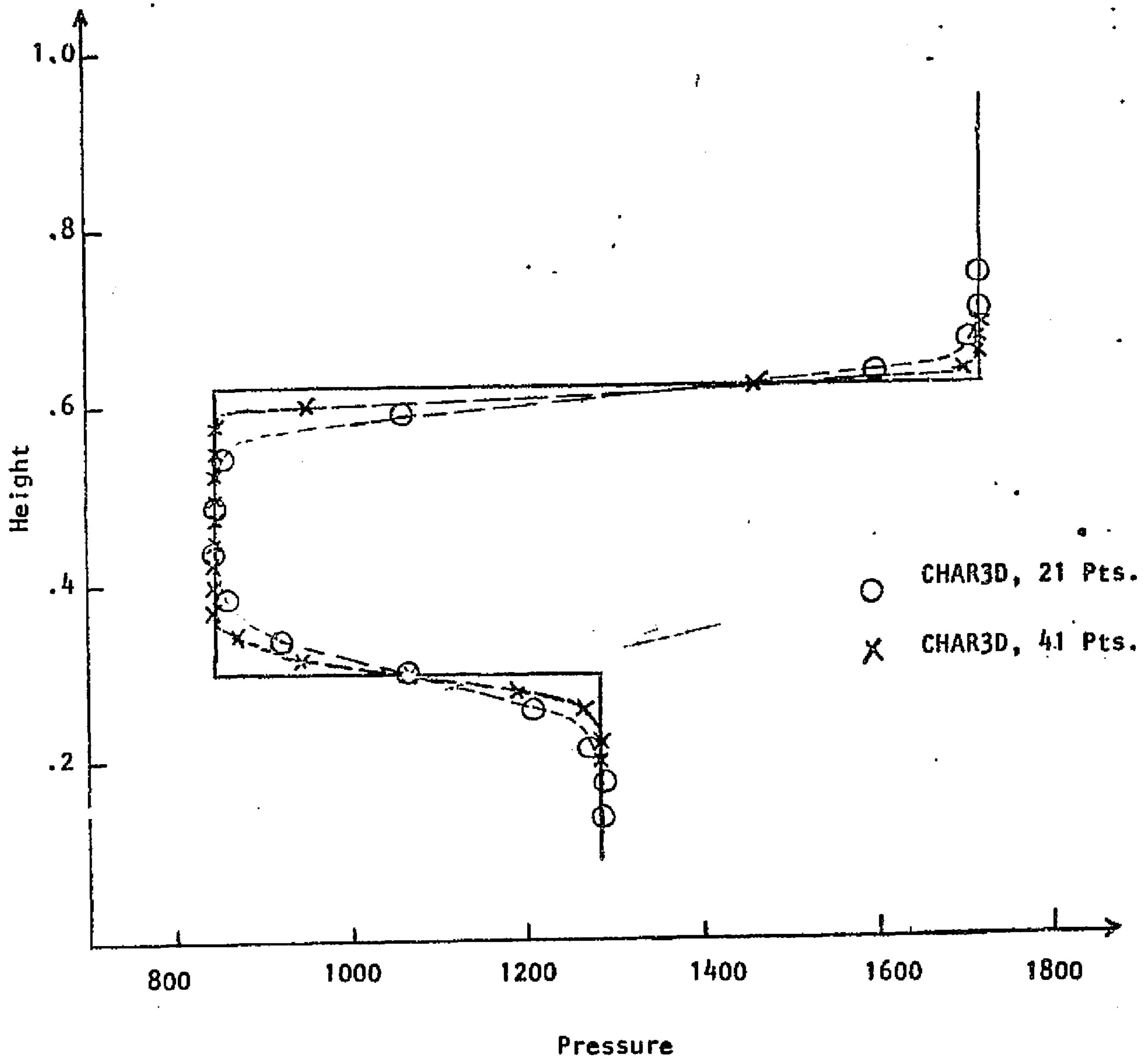

FIGURE 34. DOUBLE WEDGE INLET, PRESSURE PROFILES AT x = .64

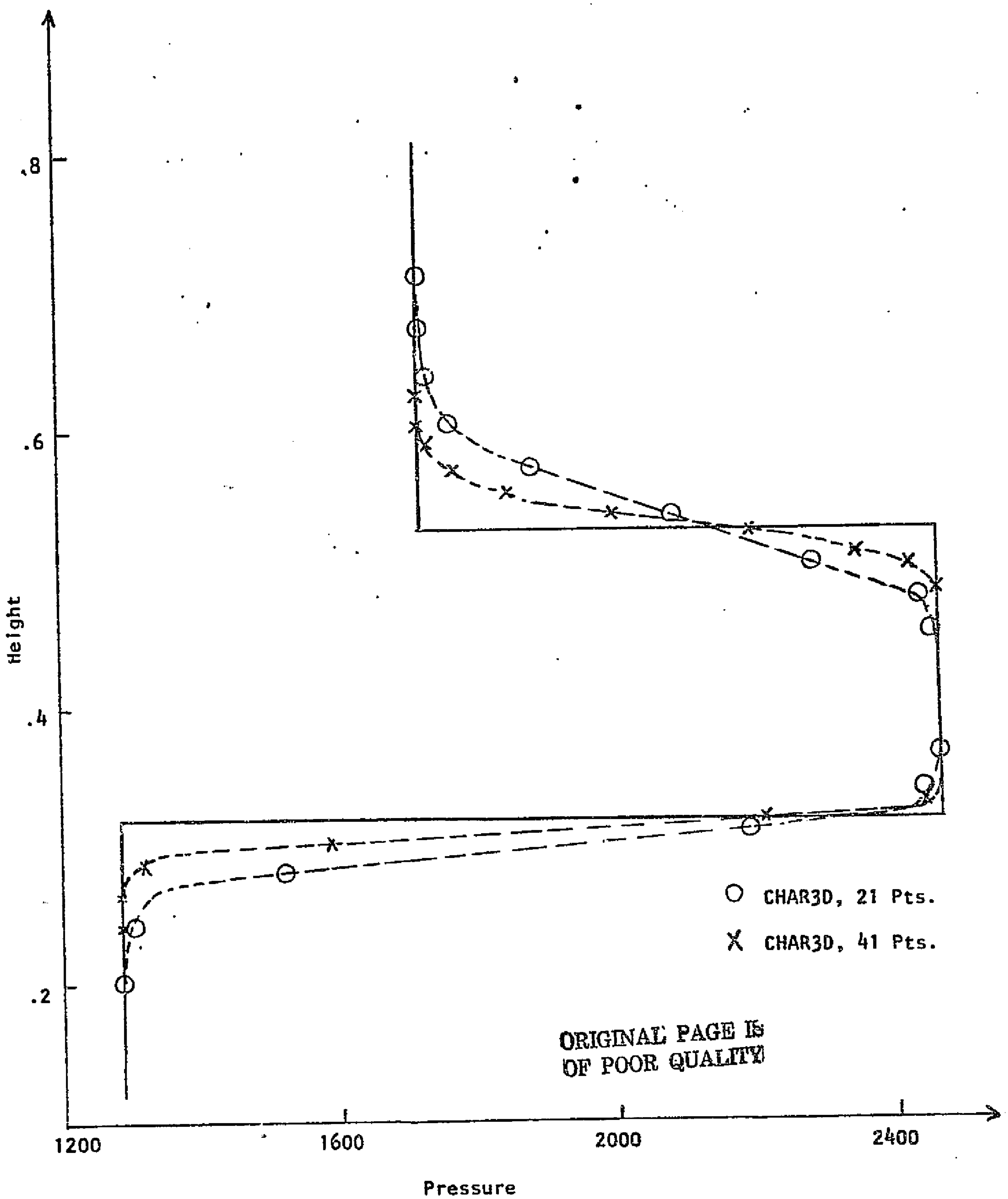

FIGURE 35. DOUBLE WEDGE INLET, PRESSURE PROFILES AT x = 1.16

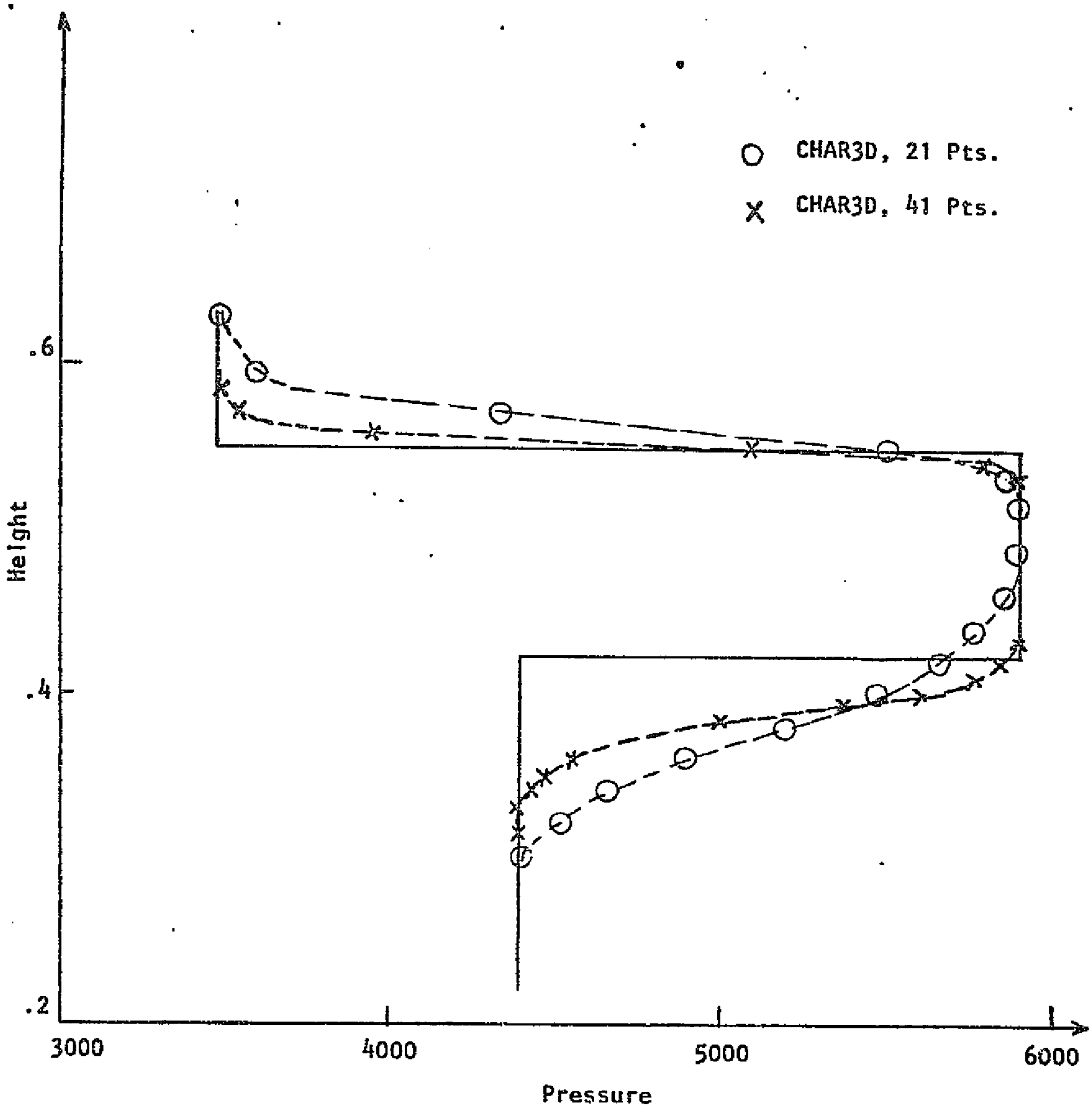

FIGURE 36. DOUBLE WEDGE INLET, PRESSURE PROFILES AT x = 2.14

ORIGINAL PAGE IS
OF POOR QUALITY

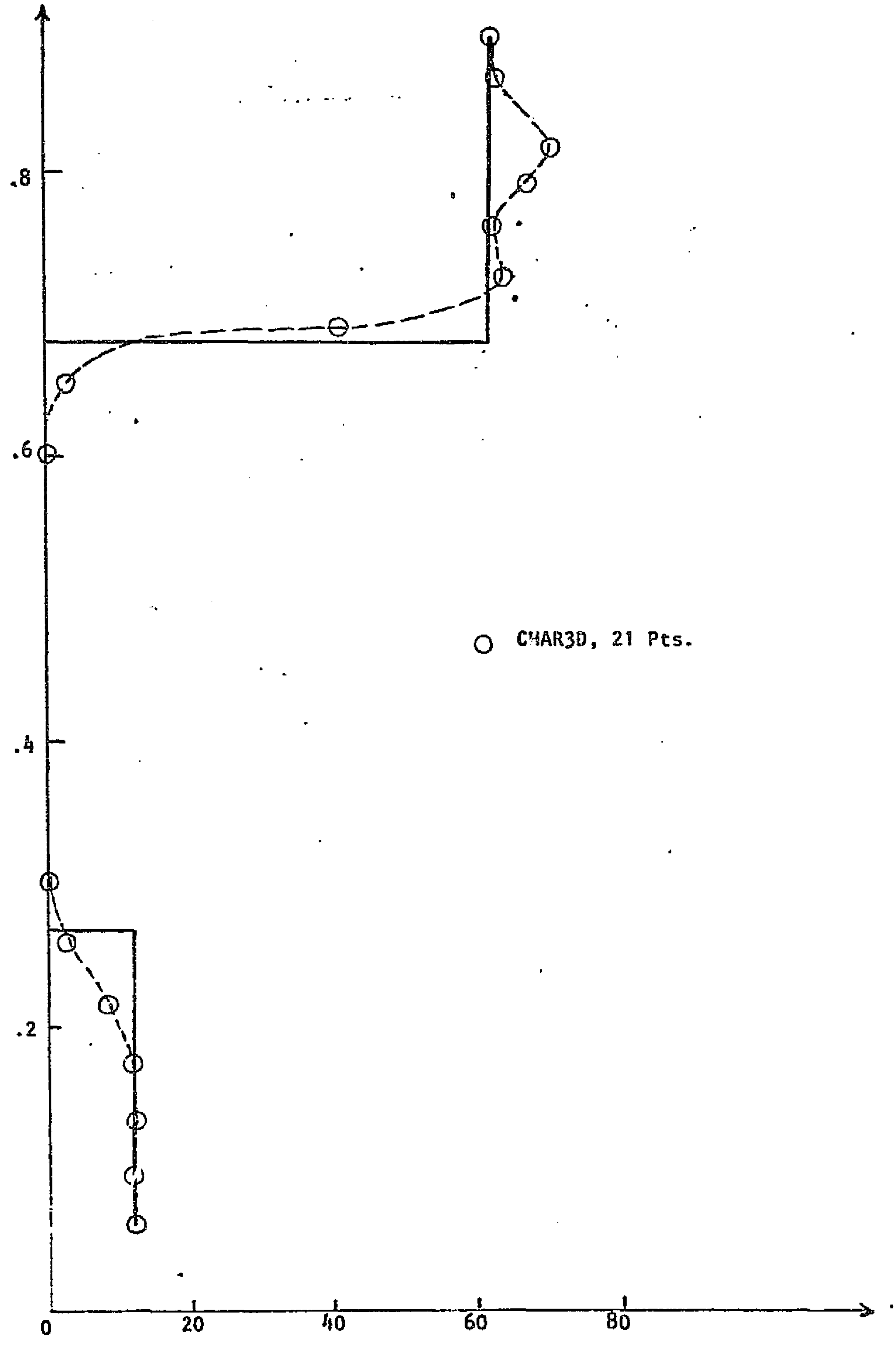

FIGURE 37. DOUBLE WEDGE INLET, ENTROPY PROFILE AT X = .64

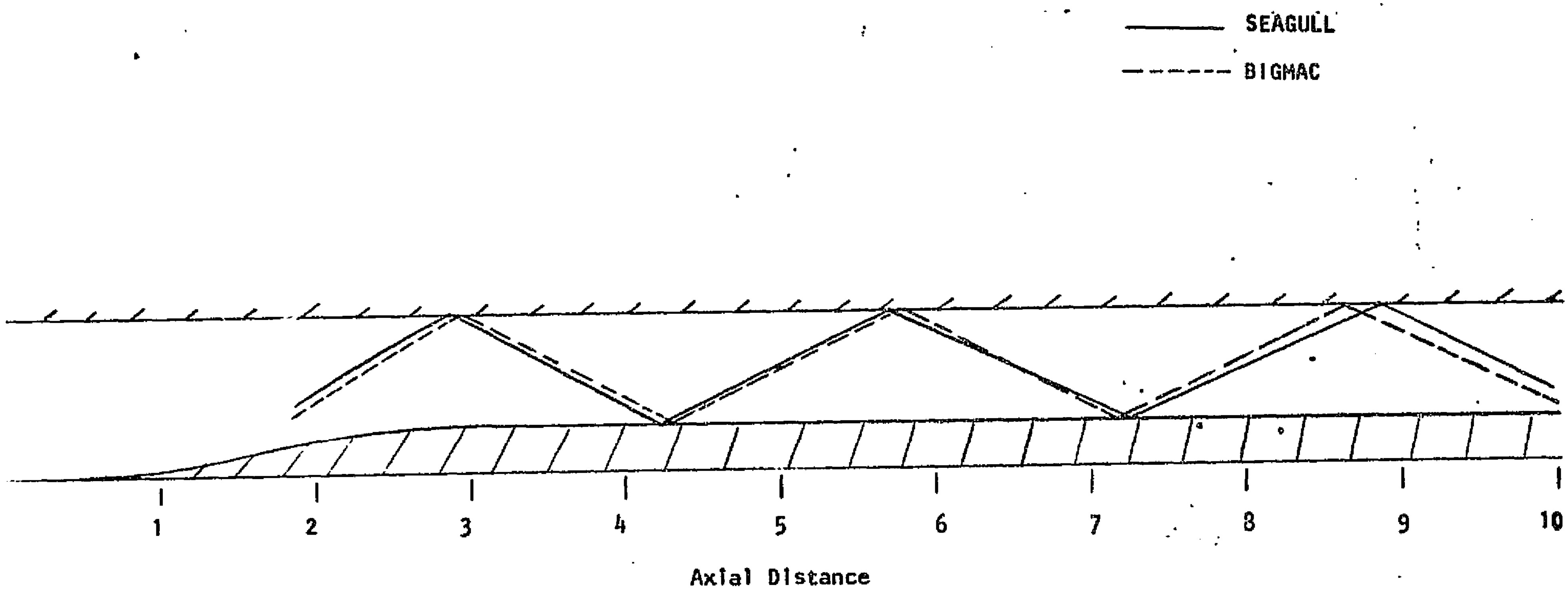

FIGURE 38. CONVERGENT DUCT GEOMETRY AND SHOCK PROPAGATION PATTERN

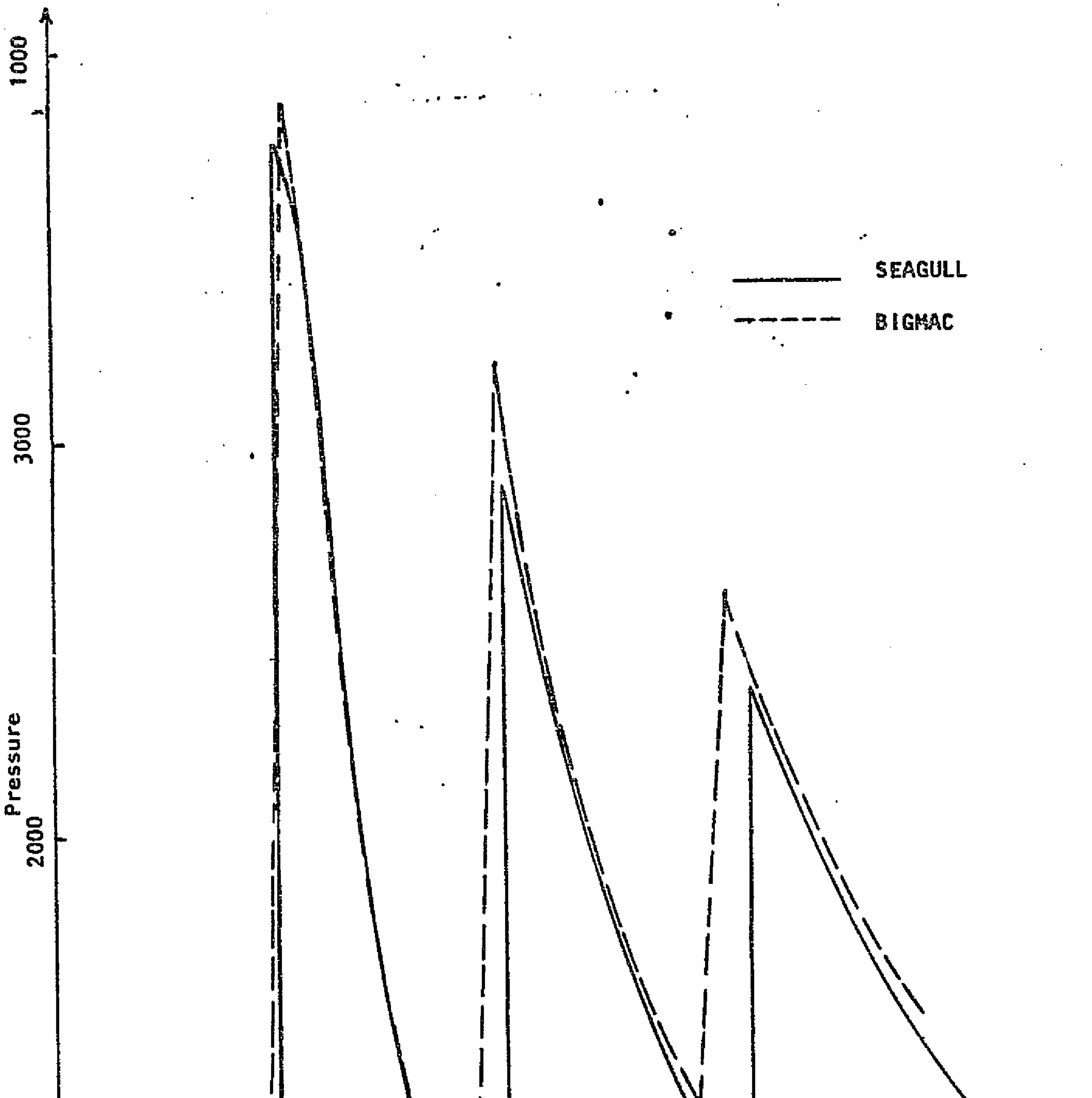

ORIGINAL PAGE IS
OF POOR QUALITY

FIGURE 39. CONVERGENT DUCT, UPPER WALL PRESSURE DISTRIBUTION-BIGMAC

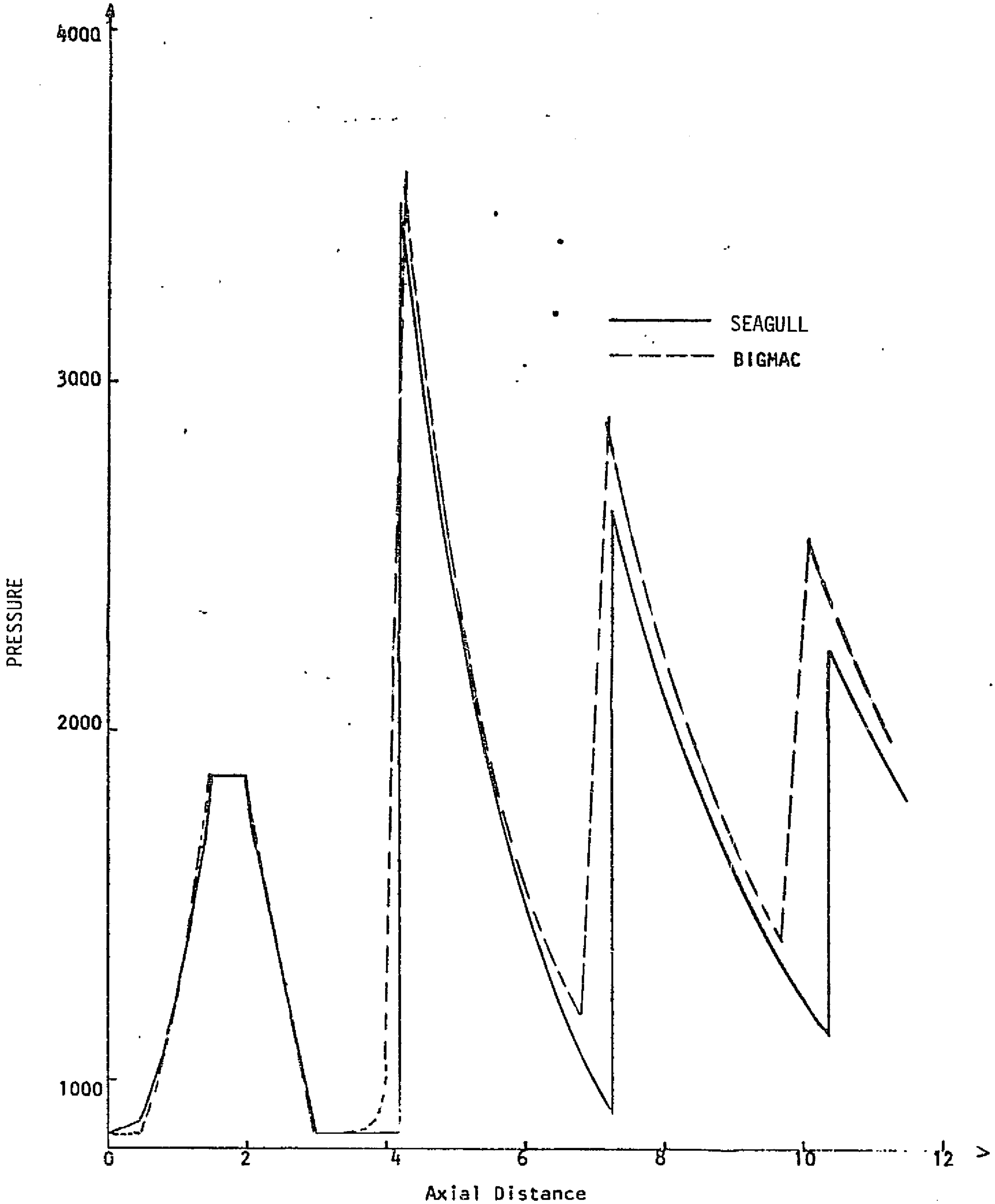

FIGURE 40. CONVERGENT DUCT, LOWER WALL PRESSURE DISTRIBUTION, BIGMAC

entropy variations are depicted in Figures (41A) and (41B). These results demonstrate ability of program BIGMAC to numerically "capture" a shock formed via the enveloping of compression waves and carry it with minimal diffusion over multiple wall reflections. The favorable comparisons obtained with this relatively coarse 11 point grid are quite promising.

Upper and lower wall pressure distributions as obtained with CHAR3D employing an 11 point grid are depicted in Figures (42) and (43). These comparison indicate that BIGMAC and CHAR3D provide results of comparable accuracy for the same grid definition. It is felt that the diffusive behavior exhibited after 4 or 5 wall reflections would be largely eliminated by the grid control technique previously described.

D. Two-Dimensional Divergent Duct - Calculations with BIGMAC were performed for the nozzle geometry depicted in Figure (44). The results are again compared with those of SEAGULL. The solid lines in Figure (44) depict the polynomial approximation of the nozzle surfaces utilized in the SEAGULL calculation, while the discrete points are those obtained with the spline fit geometry package described in Appendix II and employed in the BIGMAC calculation. It is noted that a rather poor fit for the upper wall contour was obtained in the vicinity of $x = 7$ with the spline fit approximation, which might have been avoided by utilizing more contour data points in generating the spline fits in this region of rapidly changing curvature (see Reference 11).

Initial conditions for this calculation were again the same as in previous cases. Resultant wall pressure distributions obtained with BIGMAC are compared with those of SEAGULL for the lower and upper nozzle walls in Figures (45) and (46) respectively. The poor geometric fit for the upper wall in the vicinity of $x = 7$ is clearly reflected in the oscillation depicted in Figure (46) in this area. The deviations in upper wall pressures downstream of $x = 12$ are not readily accounted for although the spurious waves emanating from the upper wall around $x = 7$ may have a dispersing effect on the expansion waves emanating from the lower surface, contributing to this beha ior. Radial pressure profiles are compared at the axial locations $x \sim 2.3$, $x \sim 5.1$, $x \sim 9$ and $x \sim 13.5$ in Figures (47A,B,C and D) respectively, indicating favorable agreement.

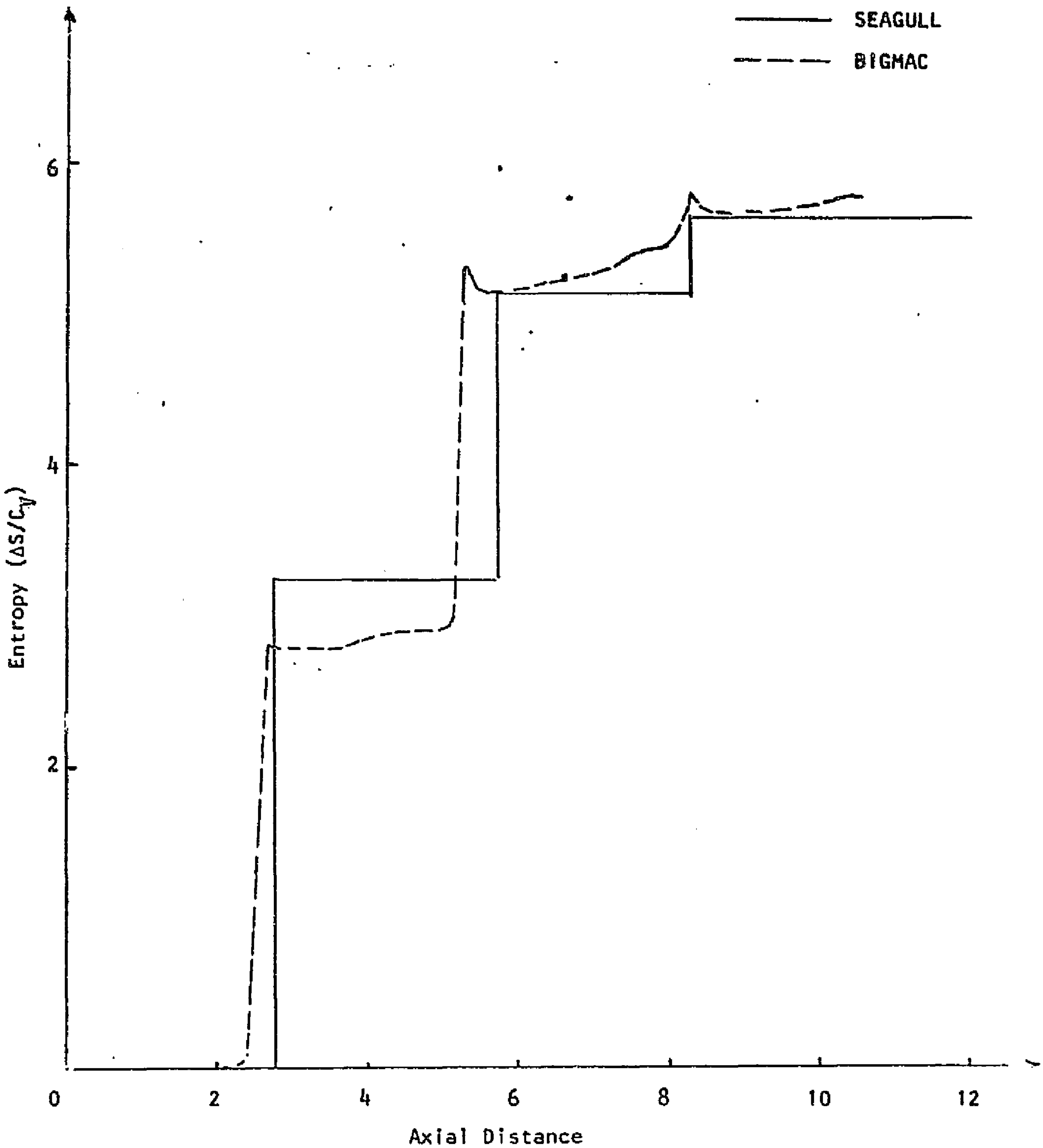

FIGURE 41A. CONVERGENT DUCT, UPPER WALL ENTROPY DISTRIBUTION - BIGMAC

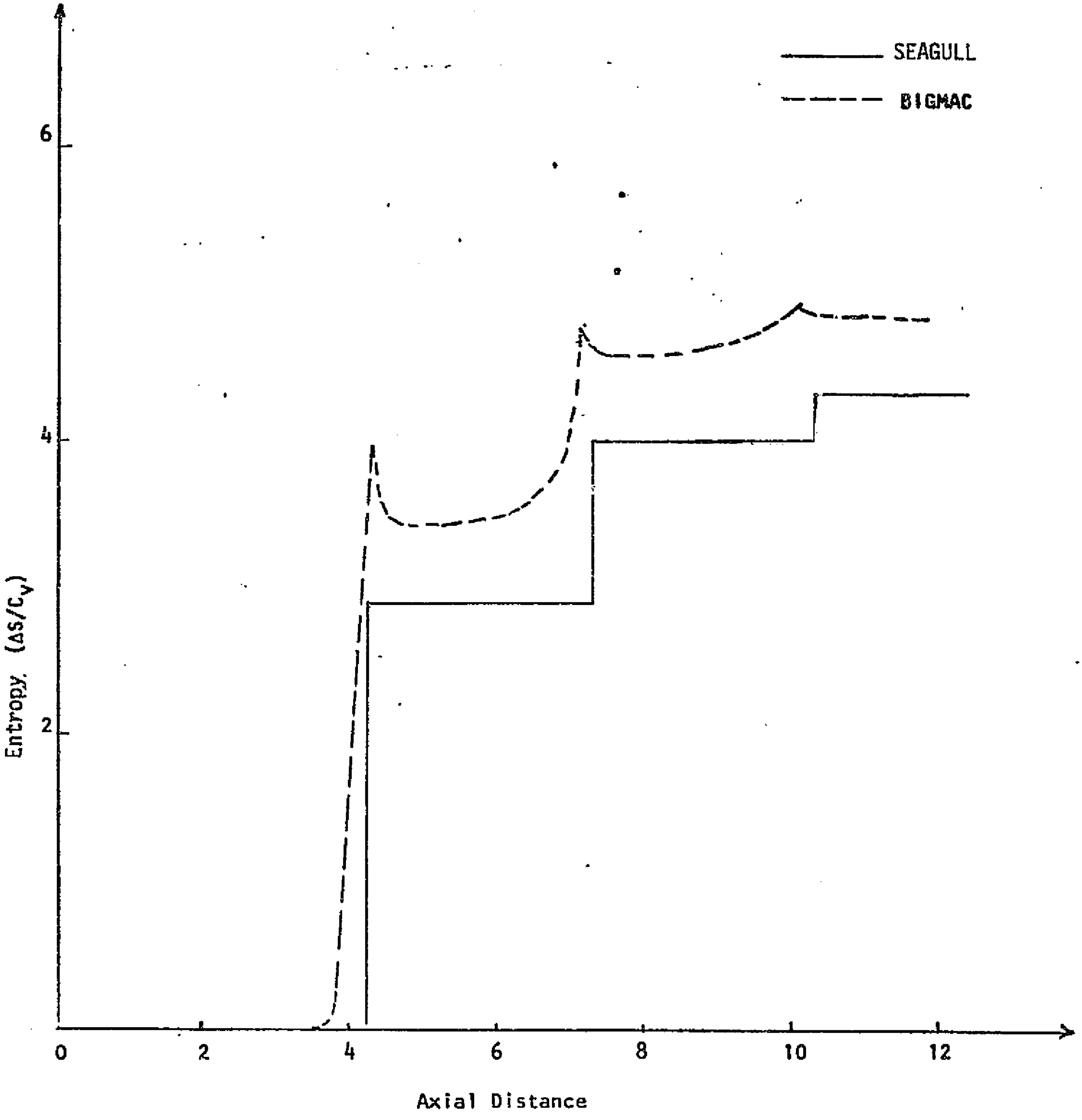

FIGURE 41B. CONVERGENT DUCT, LOWER WALL ENTROPY DISTRIBUTION - BIGMAC

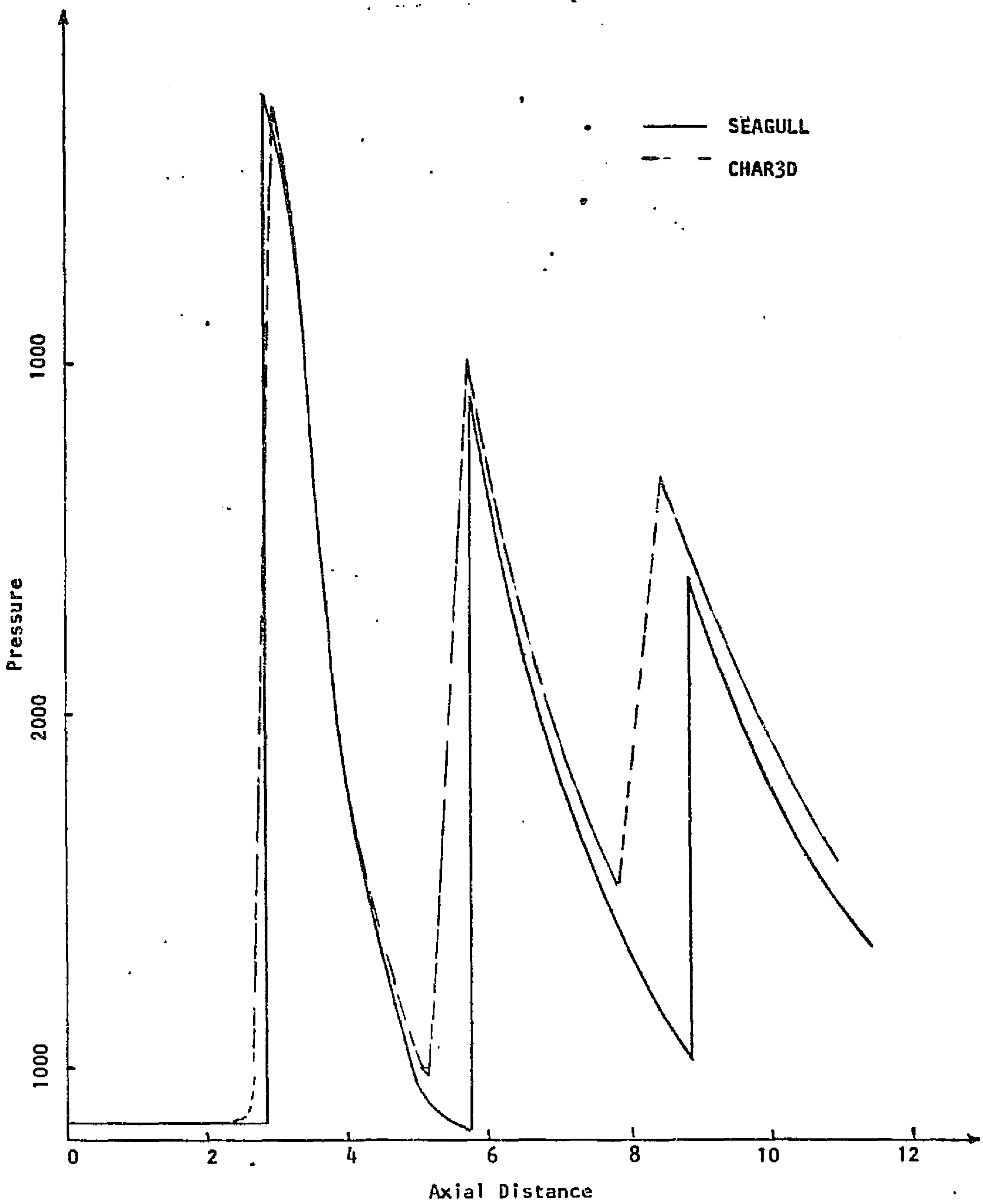

FIGURE 42. CONVERGENT DUCT, UPPER WALL PRESSURE DISTRIBUTION - CHAR3D

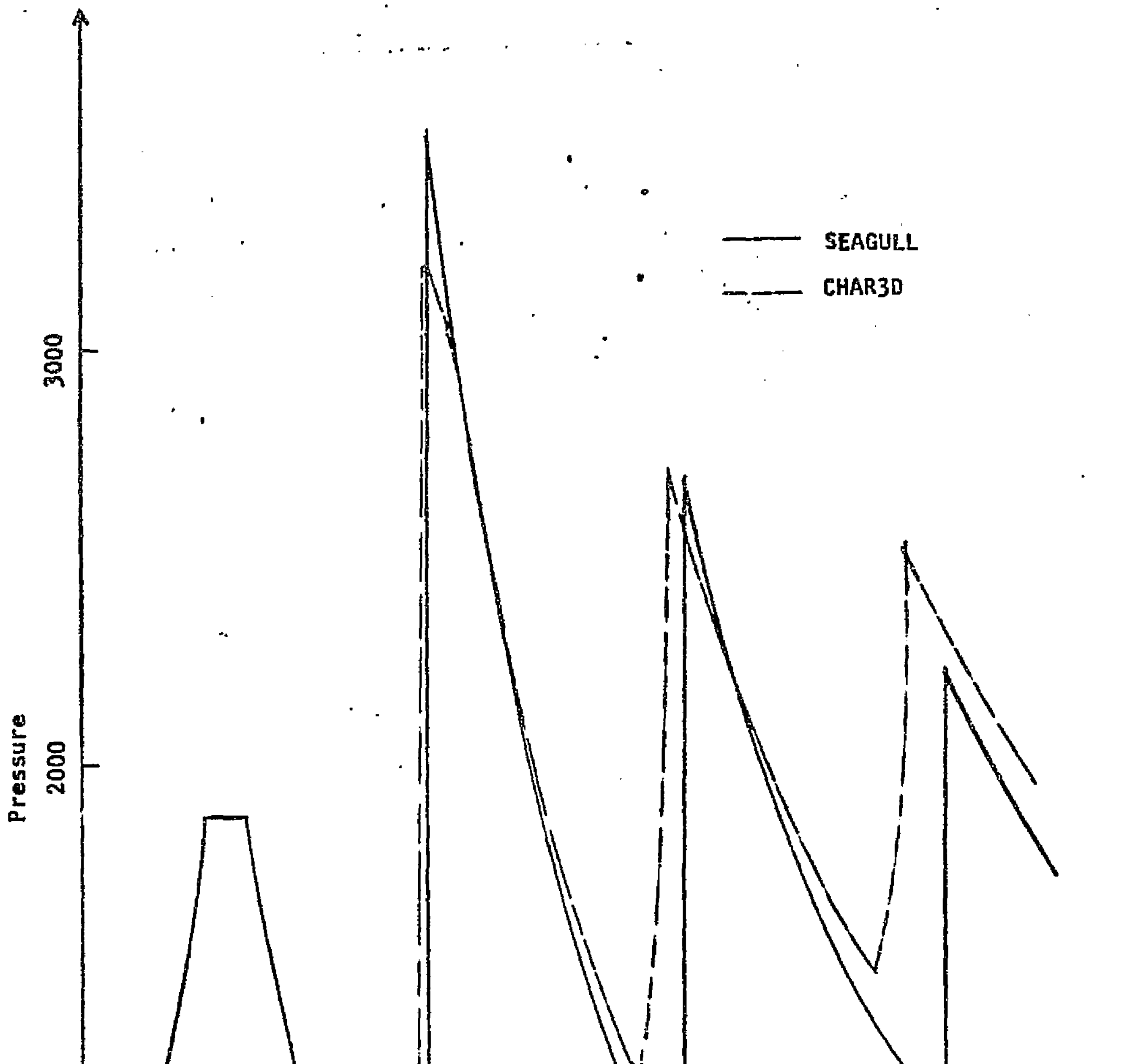

FIGURE 43. CONVERGENT DUCT, LOWER WALL PRESSURE DISTRIBUTION - CHAR3D

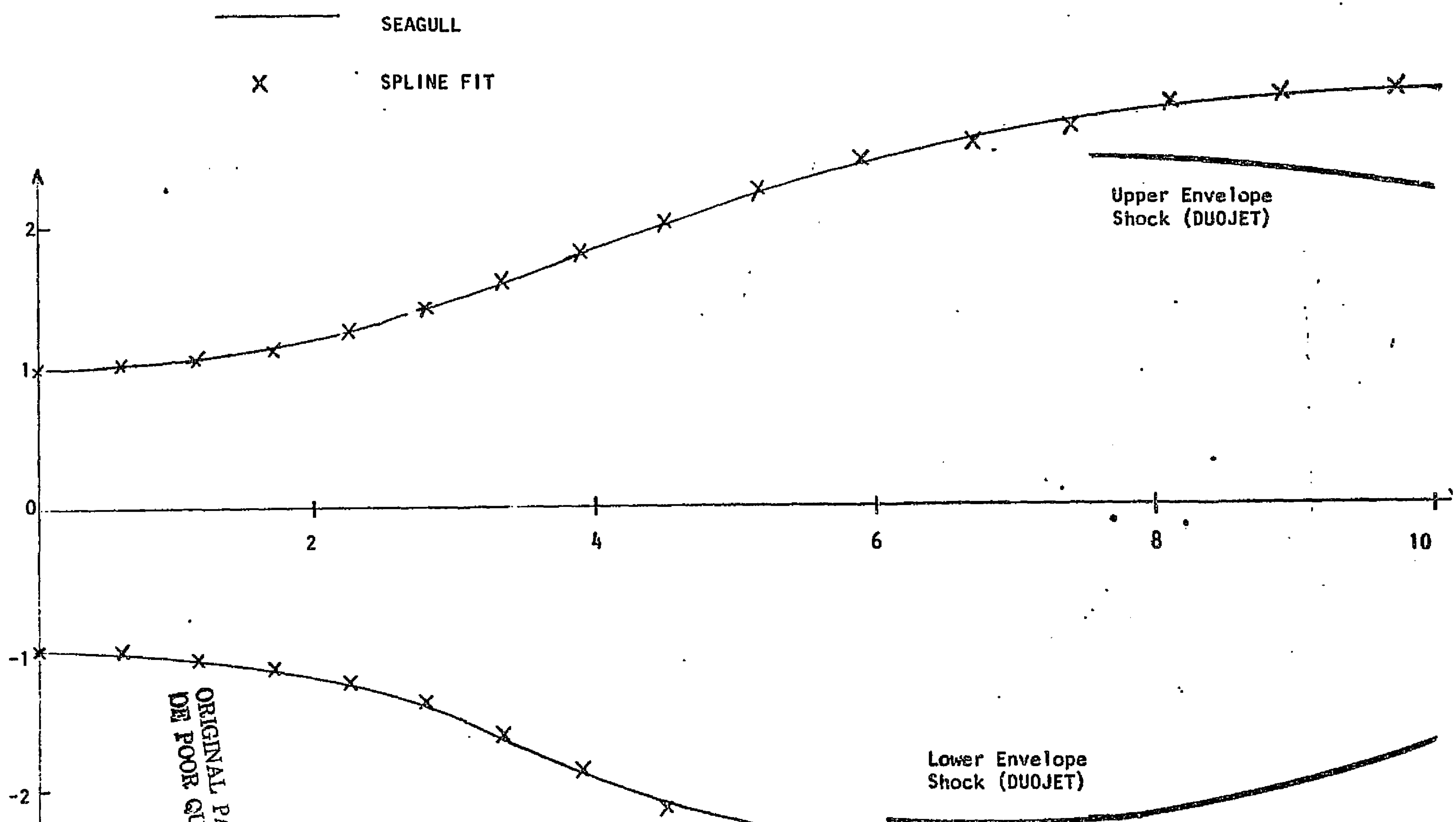

FIGURE 44. DIVERGENT DUCT GEOMETRY

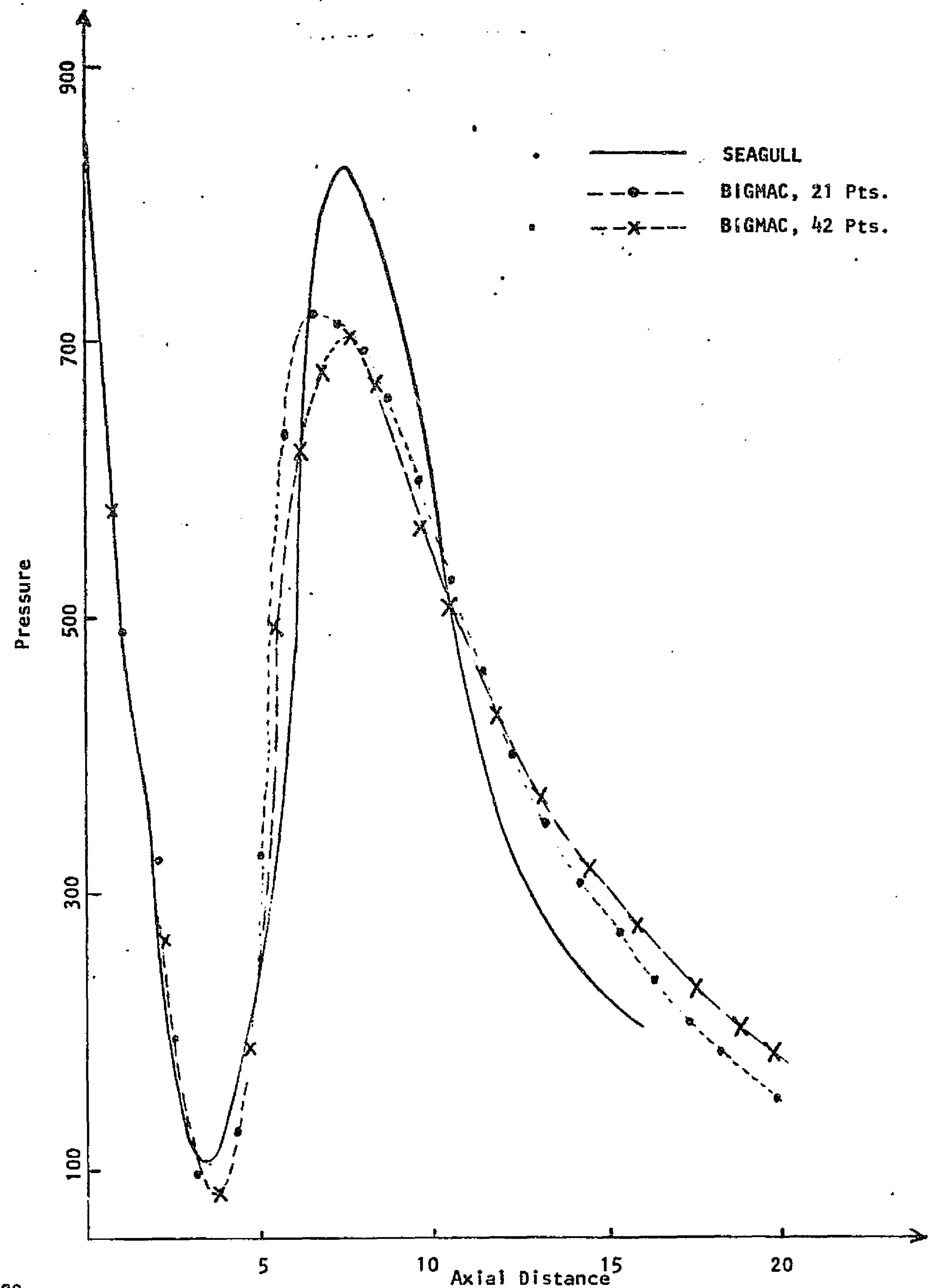

FIGURE 45. DIVERGENT DUCT, LOWER WALL PRESSURE DISTRIBUTION

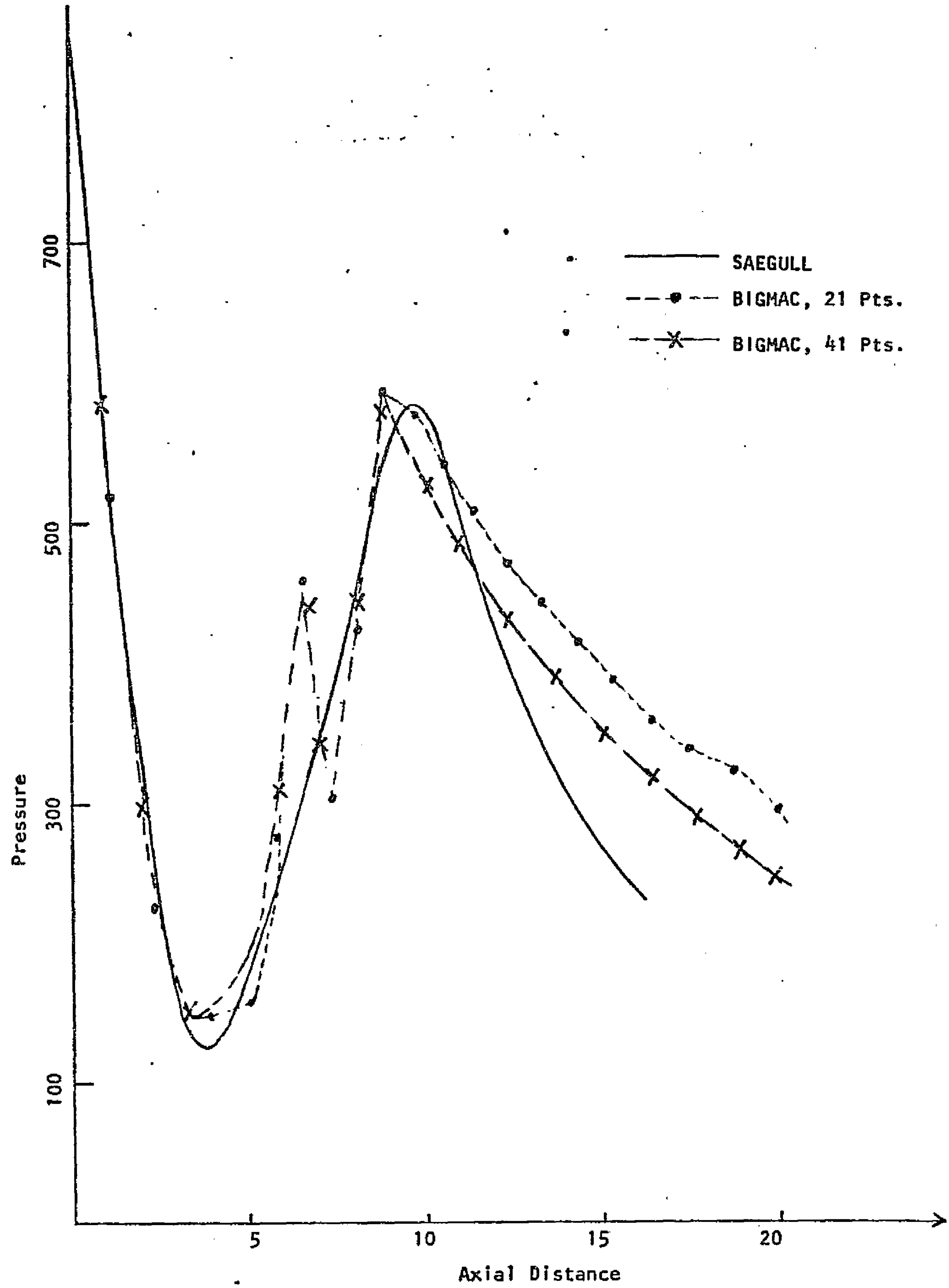

FIGURE 46. DIVERGENT DUCT, UPPER WALL PRESSURE DISTRIBUTION

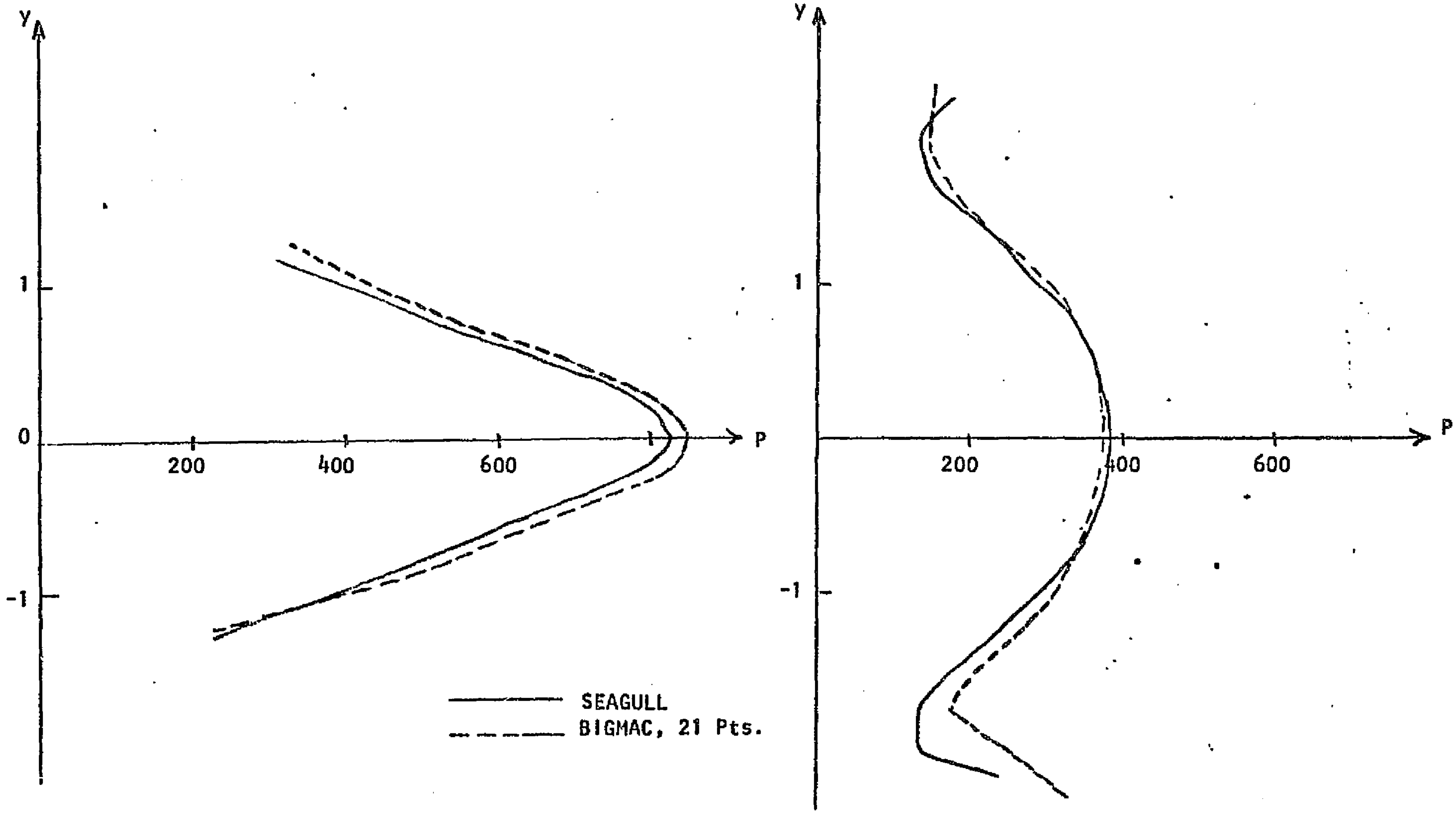

A. x = 2.3

B. x = 5.1

FIGURE 47. DIVERGENT DUCT, PRESSURE PROFILES

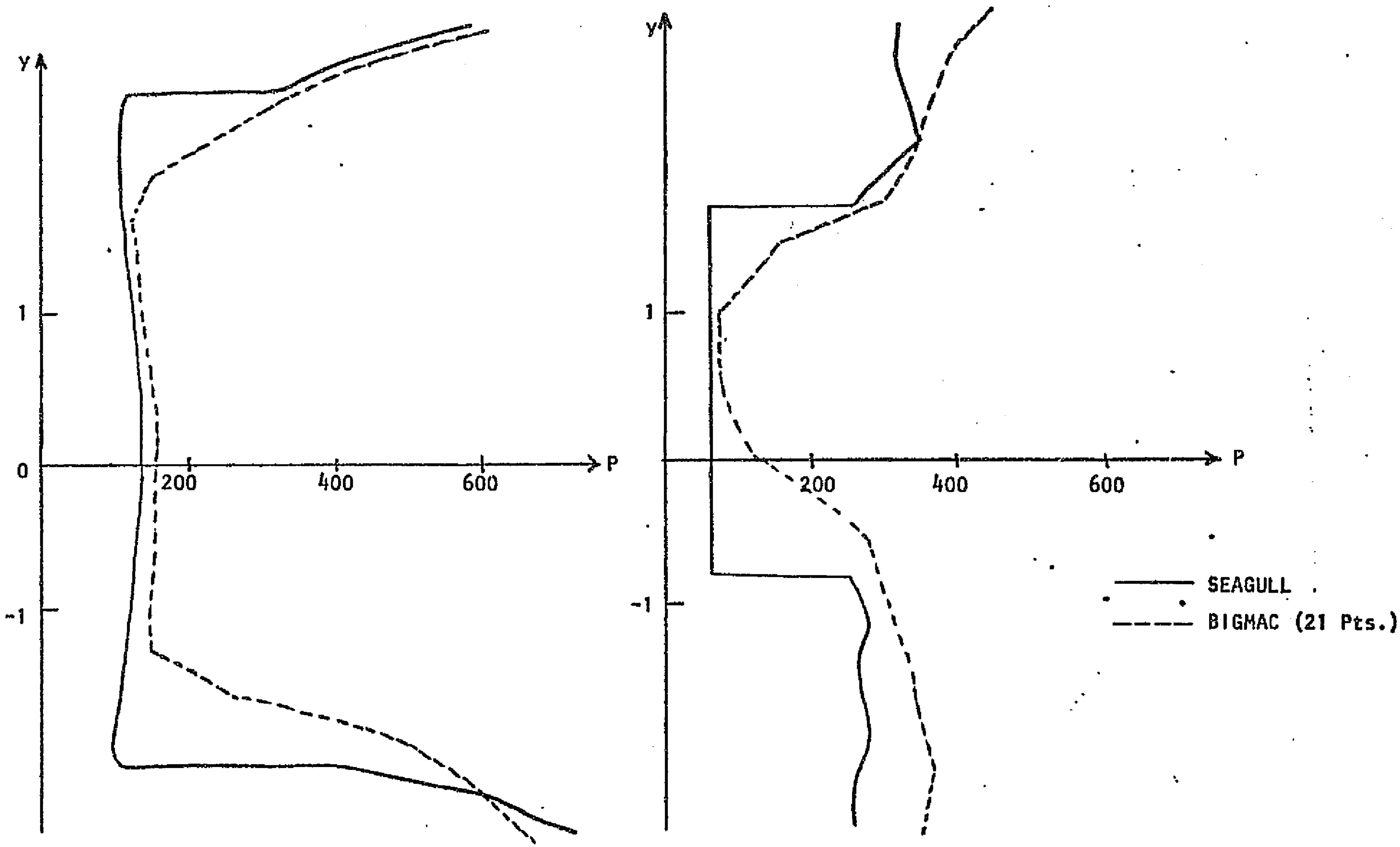

C. x = 9.0

D. x = 13.5

FIGURE 47. DIVERGENT DUCT, PRESSURE PROFILES

E. Internal Corner Calcualtions - Corner flowfields associated with interacting waves formed from mutually perpendicular surfaces represent ideal cases with which to test the developed codes. Experimental data and calculations exploiting the conical invariance of the reported cases is available for comparison. In all cases reported, flow at the initial station was uniform and the interaction flowfield was generated by an abrupt change in wall angle at the initial station for two mutually perpendicular surfaces.

Results for a 5° double expansion corner are depicted in Figures (48) and (49). These results were obtained with CHAR3D starting from the conditions $P_{\infty} = 945.5$ and $M_{\infty} = 2.94$ for an 11 x 11 grid in cartesian coordinates. Results are depicted after nine axial marching steps as required to establish a converged solution. This is indicated by the axial variation or corner pressure which originally overexpands and then recompresses to the converged value.

The finite convergence length required to achieve invariance has important implications in the generalized application of corner boundary procedures in regions of discontinuity. In particular, one must achieve convergence in a distance which is small compared to the overall inviscid length scale of the problem - this sets the grid network size for the localized corner calculation. In addition, one must isolate the computation of this region so that extraneous waves doe not interfere with the convergence process.

Results for an expansion-compression corner generated by an abrupt 5° expansion and $7\frac{1}{2}^{\circ}$ compression of a uniform Mach 2 flow are depicted in Figure (50) as calculated by BIGMAC. An 11 x 11 cartesian grid was employed and the converged results are depicted after 10 axial marching steps. These results are compared with the detailed conically invariant numerical solution of Shankar (Reference 19) and the experimental results of Nangia (Reference 20).

Results for a 12.2° double compression corner are presented in Figure (51) as calculated with BIGMAC. A line source reference plane network was employed in this calculation in view of the larger turning angles than in the previous two corner flows. The initial flow was at a Mach number of 3.17. Converged results are depicted after 35 axial marching steps indicating an increase in

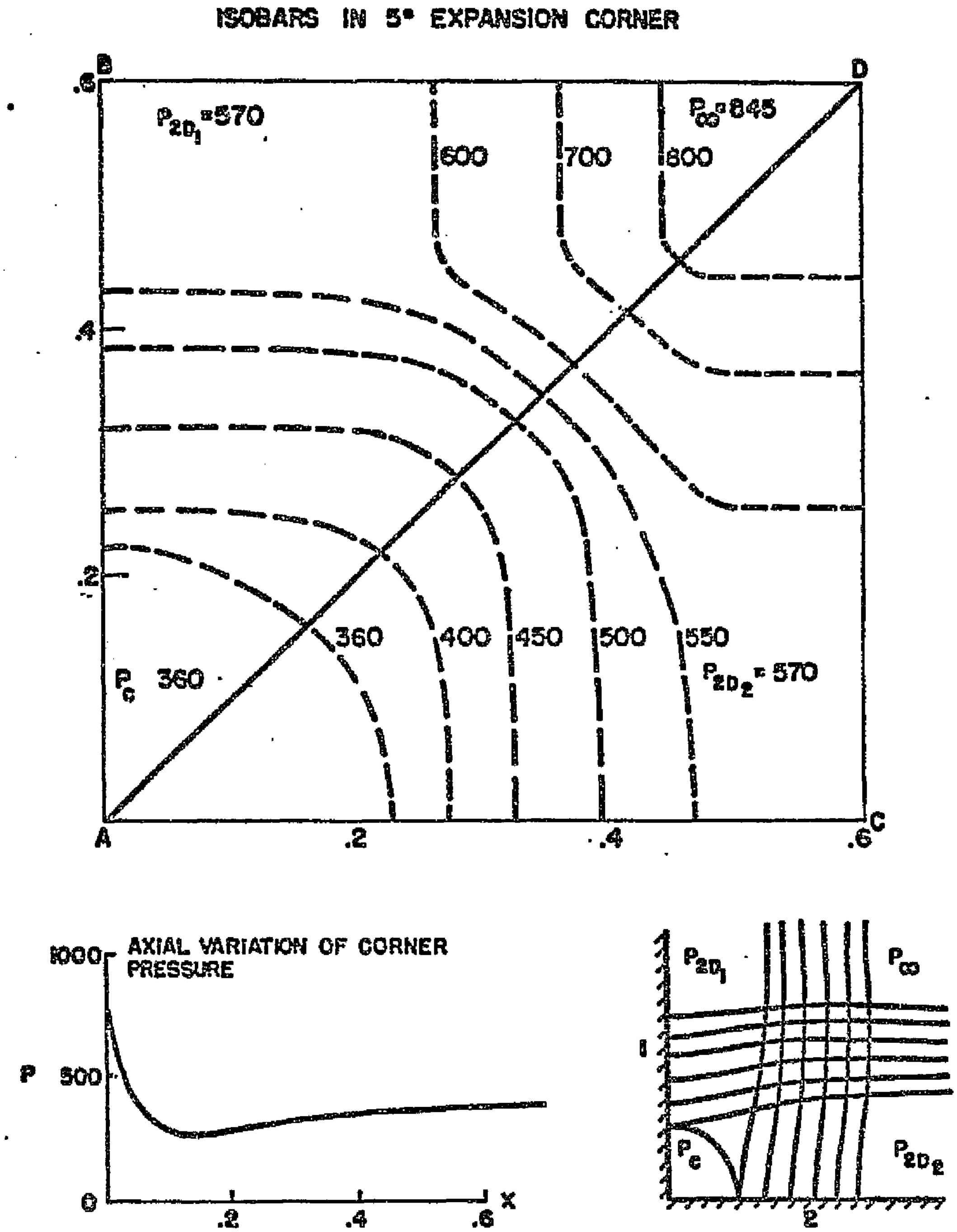

Figure 48. Results for 5° expansion corner. P_c is corner pressure; P_{2D} is two-dimensional wall pressure.

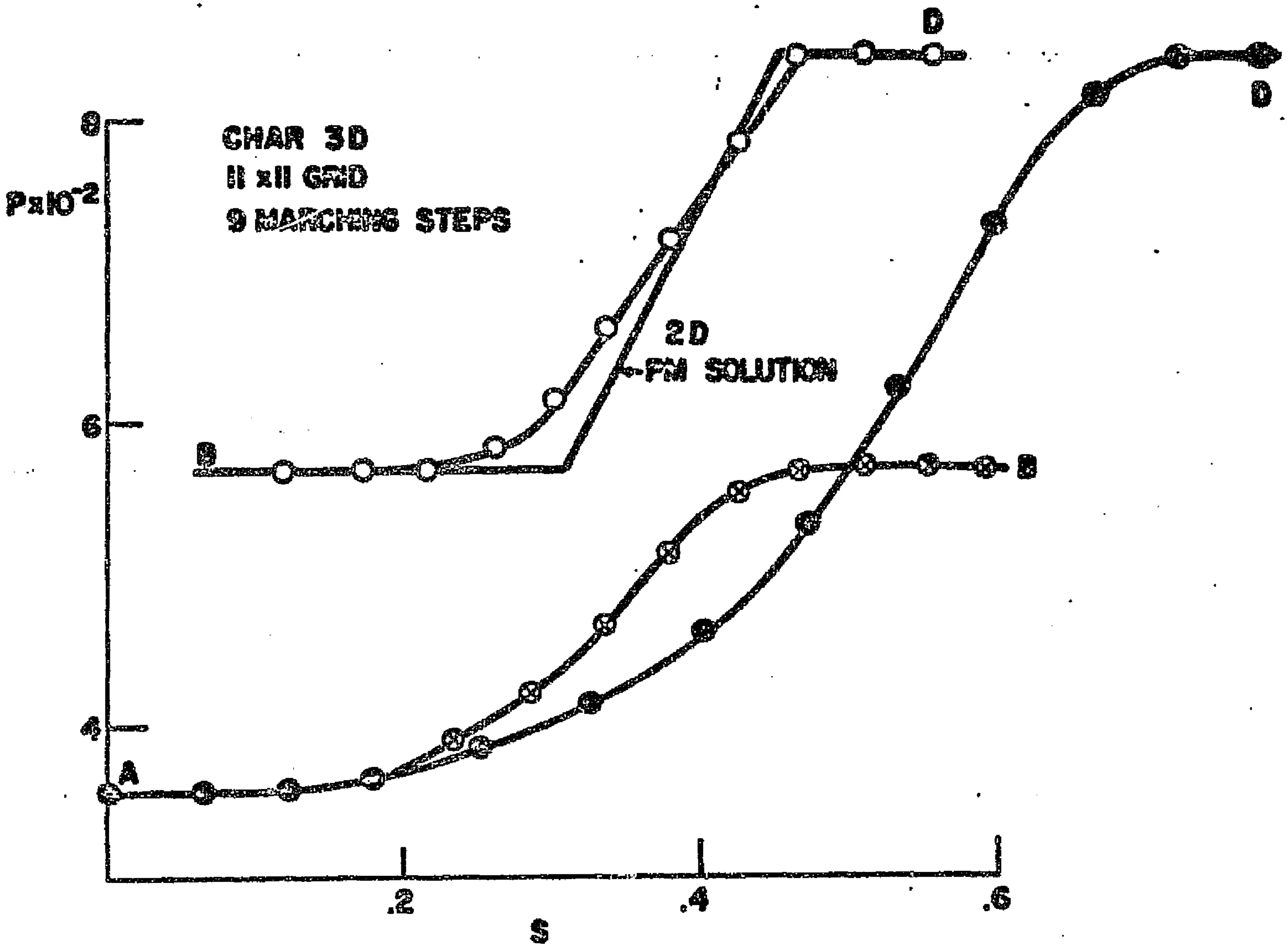

Figure 49.- Pressure distribution for 5° expansion corner. PM means Prandtl-Meyer.

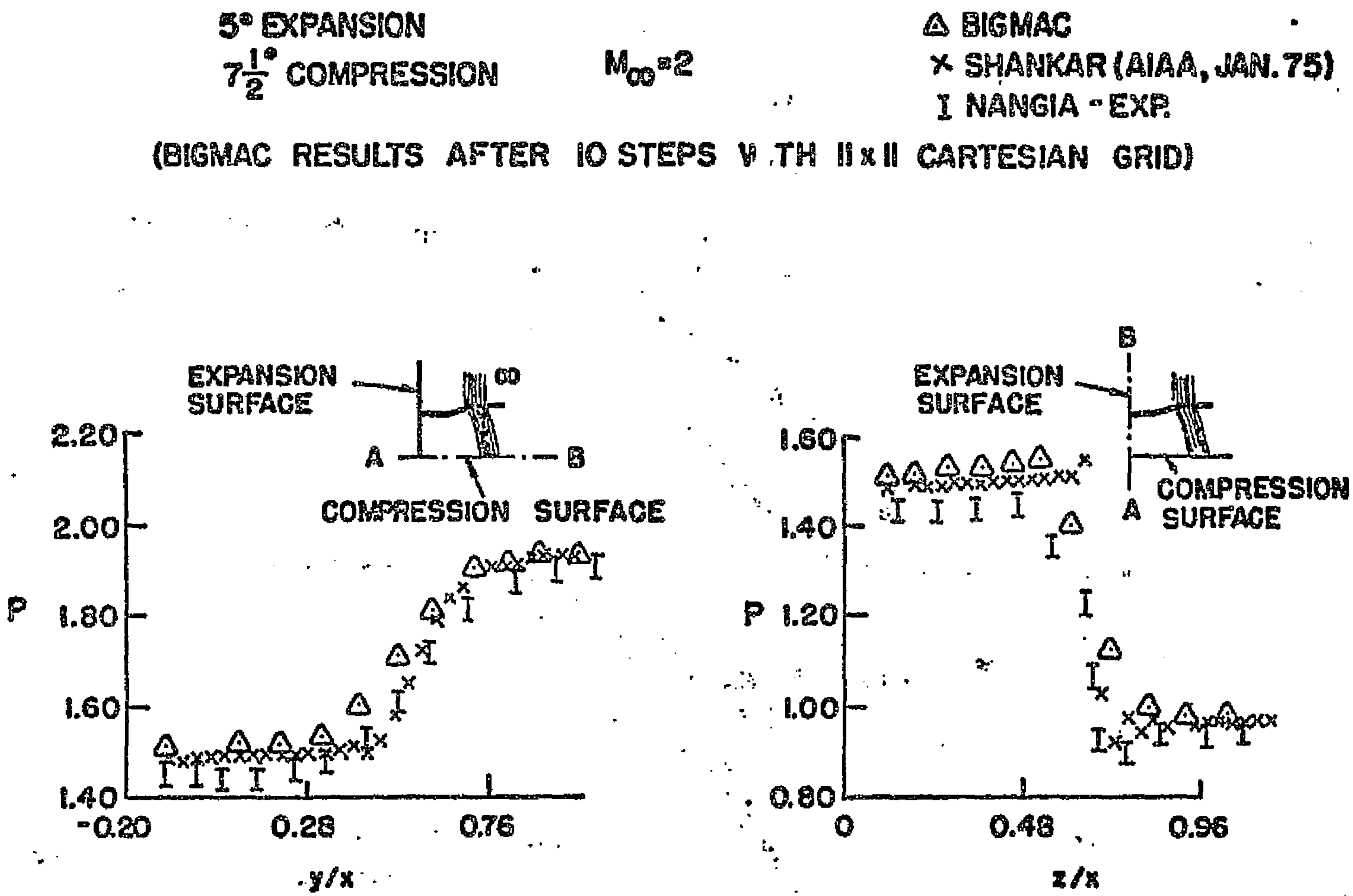

Figure 50.- Results for an expansion-compression corner.

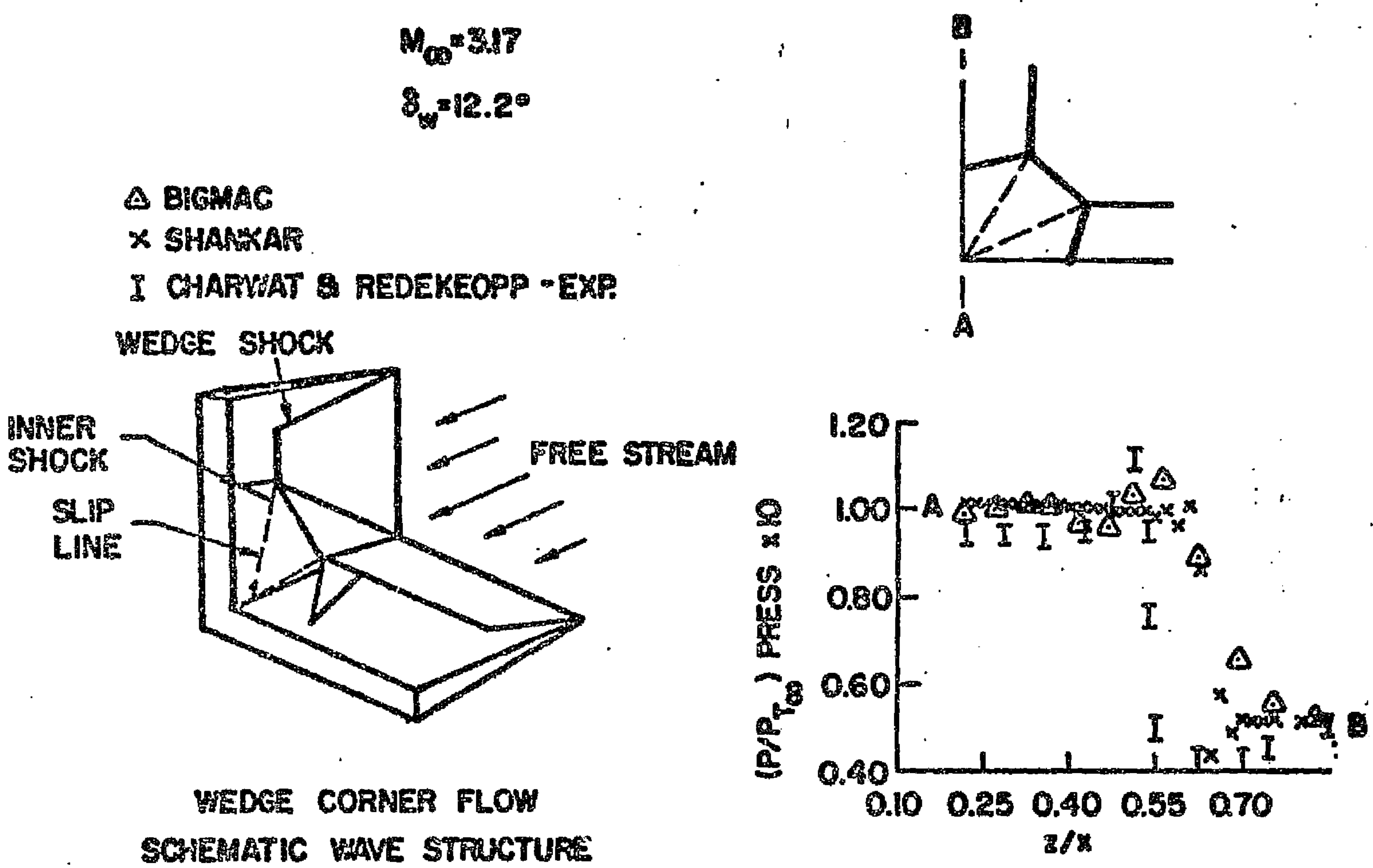

Figure 51. Compression corner. δ_w is wedge angle; P_{T_∞} is total pressure.

convergence length with the severity of the discontinuity as would generally be expected. Comparisons are made with the numerical solution of Shankar (Reference 19) and the experimental results of Charwat and Redekeopp (Reference 21).

F. Square Nozzle - The three-dimensional flowfield within the square nozzle depicted in Figure (52) has been calculated by BIGMAC. This flowfield is characterized by the initial interactions of expansion waves emanating from mutually perpendicular surfaces and the subsequent interaction of enveloping shock systems generated by recompression on the upper wall and sidewall. The initial Mach number was 2.94 and the initial nondimensional pressure was 845.5. A perfect gas calculation with $\gamma = 1.4$ was performed. The calculation employed 21 grid points in each reference plane with 11 reference planes initially (reference plane number 1 was the plane of symmetry). A cartesian network was utilized and additional reference planes were inserted as the module sidewall opened. At the straight section, the network contained 18 reference planes. Pressure contours on the symmetry plane $y = 0$ are depicted in Figure (53). It is of interest to note that the contours on the symmetry plane $z = 0$ are virtually identical to those of Figure (53) thus providing a check on the overall symmetry of the computational system. Similar checks with CHAR3D have not provided the required symmetry in cases where strong wave systems were propagating normal to the reference planes. Of particular interest in Figure (53) is the intersection of four three-dimensional shock surfaces at $x \approx 17$ and and $y = z = 0$. This results from the reflection of the envelope shock produced by the sidewall and the reflection of the envelope shock produced by the upper wall, resulting in an approximate 15/1 pressure ratio at this location. The axial pressure variation along the corner is depicted in Figure (54) while pressure variations along several streamlines in the symmetry plane are depicted in Figure (55).

G. Single Module Nozzle-Exhaust Flowfield - The internal nozzle and exhaust plume flowfield associated with the single module depicted in Figure (56) has been calculated by BIGMAC. The gas mixture was assumed to be perfect and the calculation was initiated by the following uniform conditions at the combustor exit:

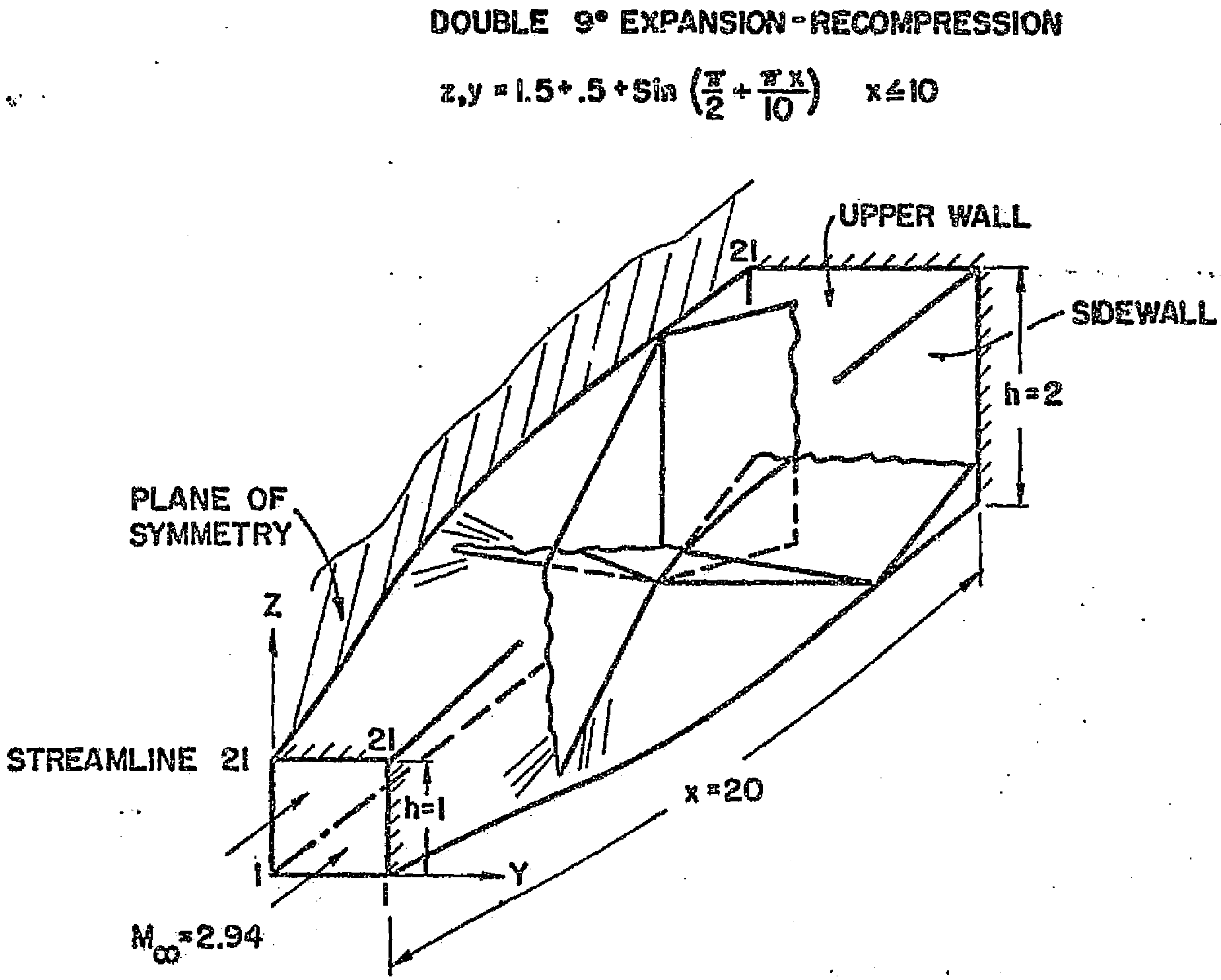

Figure 52. Square nozzle; h is height.

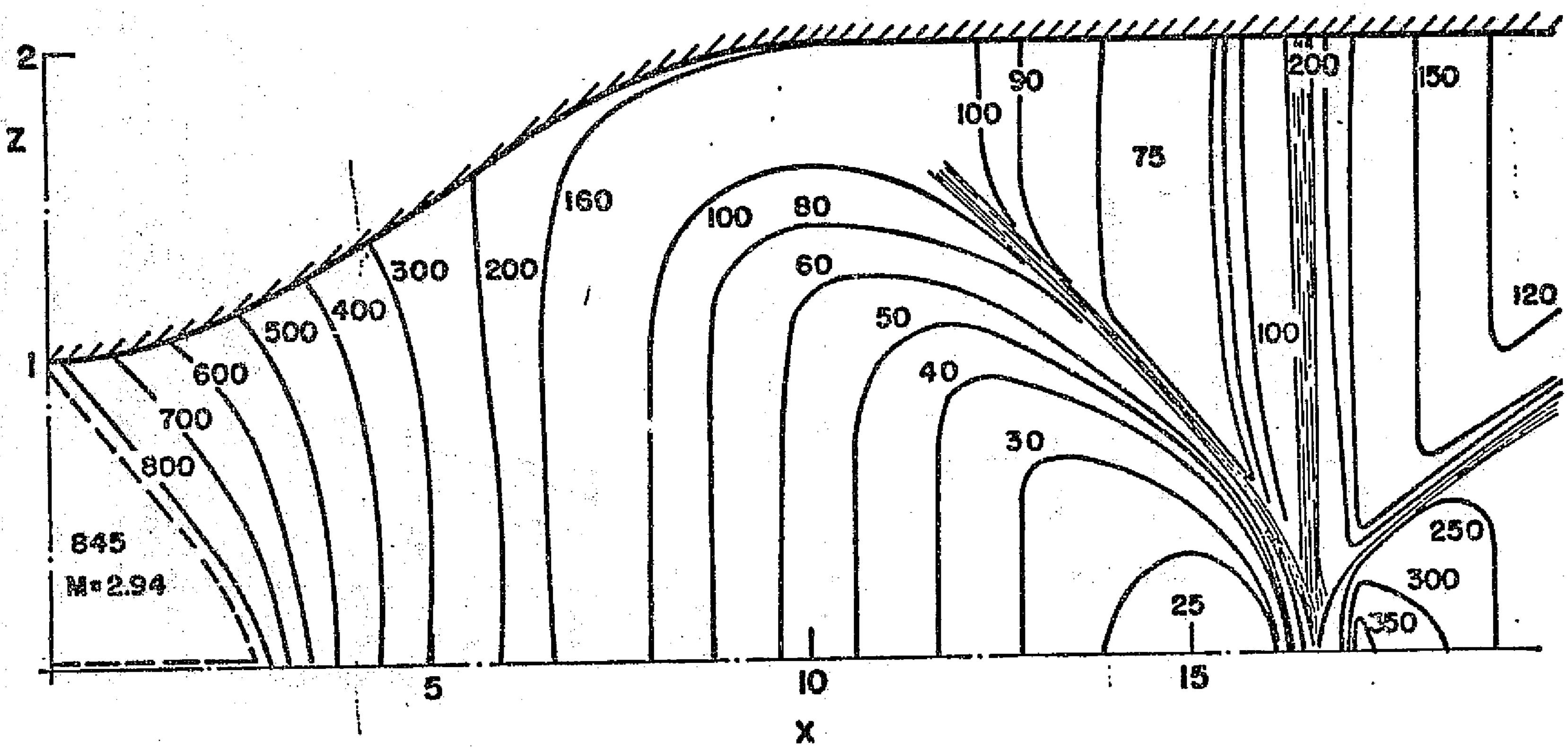

Figure 53. Pressure contours on symmetry plane of square nozzle.

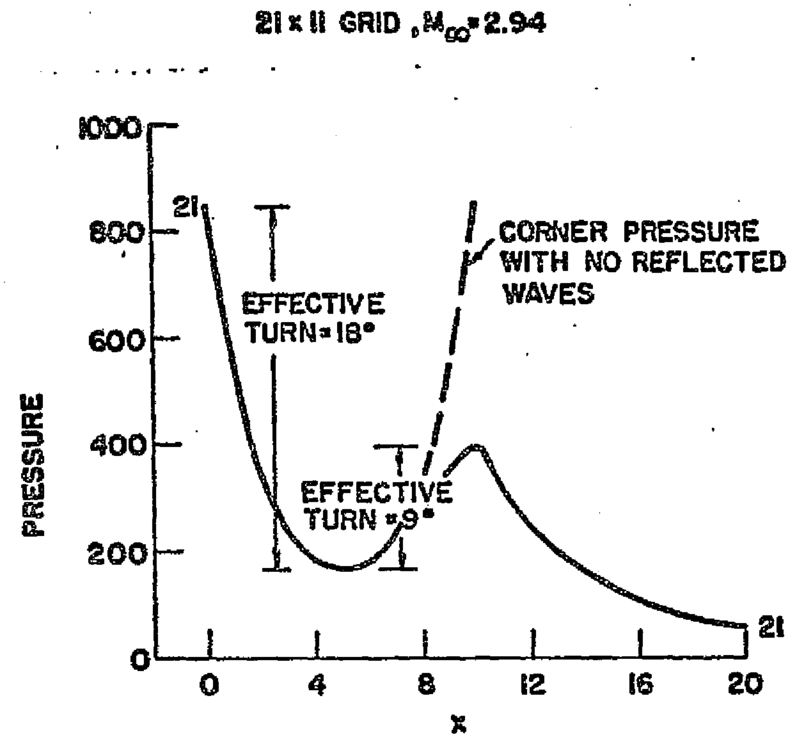

Figure 54. Streamline pressure distribution at sidewall corner of square nozzle.

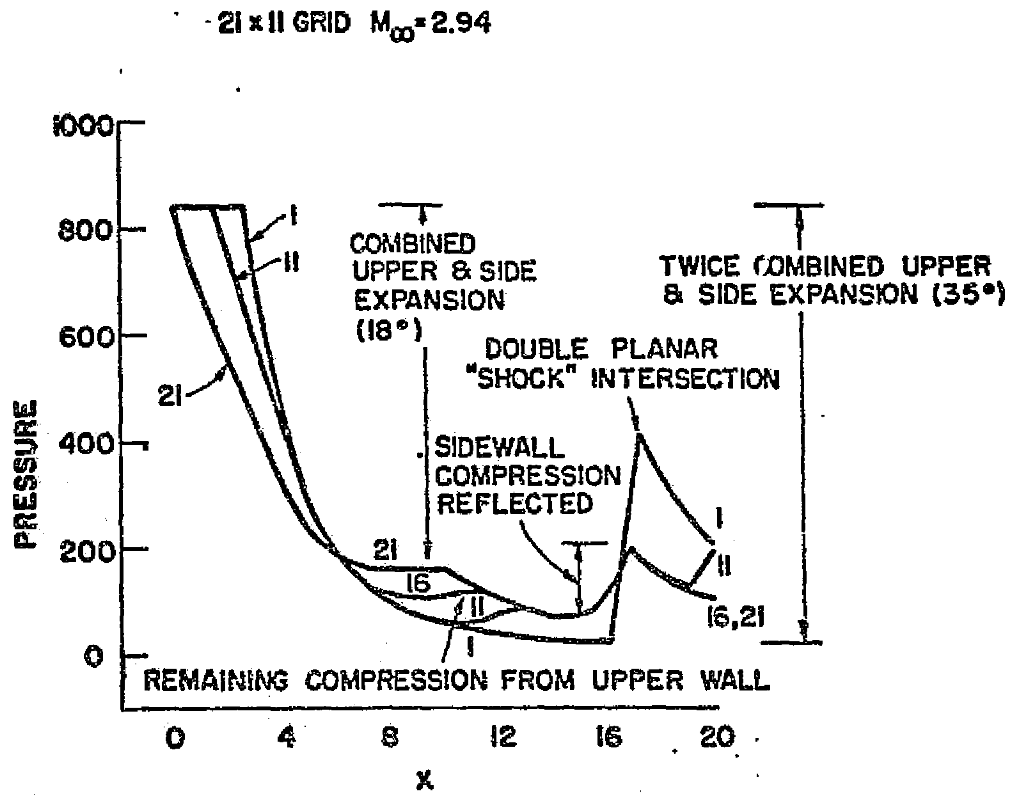

Figure 55. Streamline pressure distribution in plane of symmetry of square nozzle.

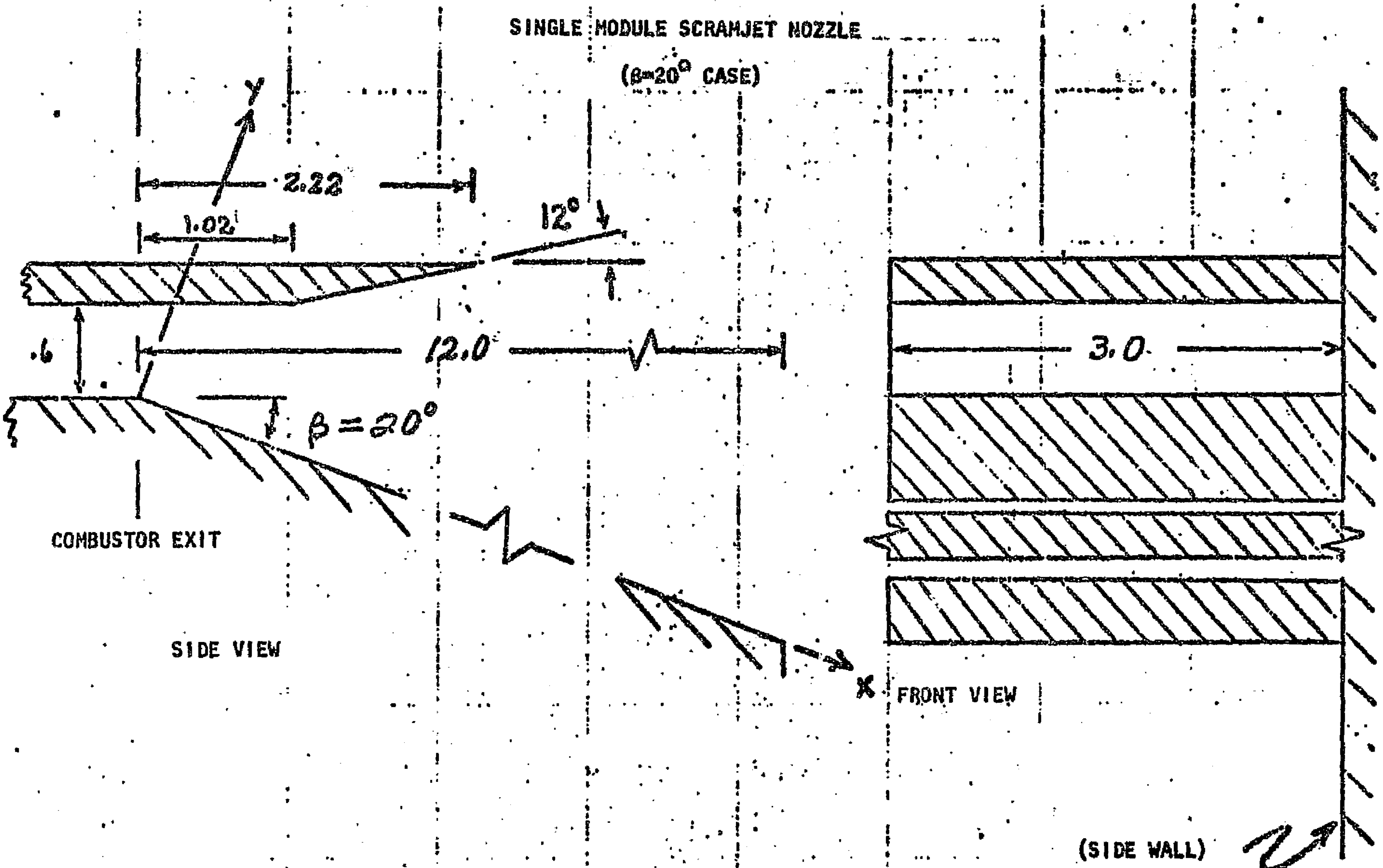

FIGURE 56. SINGLE MODULE GEOMETRIC CONFIGURATION

$$M_E = 1.70$$

$$\gamma_E = 1.20$$

The external flow was quiescent with $\gamma_\infty = 1.4$.

The internal flowfield was two-dimensional and calculated employing an 11 point grid up to the cowl exit station ($x = 2.98$). Note that x is measured along the vehicle undersurface and y normal to it. The resultant flowfield at the cowl exit station is underexpanded along the cowl trailing edge and mixed (partially overexpanded and partially underexpanded) along the end wall trailing edge. The reference plane networks employed are sketched in Figure (57). Fifteen vertical reference planes, fifteen cylindrical reference planes in the corner wraparound system and four horizontal reference planes are employed in this calculation. Resultant interface locations are depicted in Figure (58). The last marching station calculated was at $x/H_t = 6.43$. The requirement for relocating the cylindrical origin (floating origin option) is clearly necessary to continue the calculations beyond this point. All cases with some degree of overexpansion will require this modificiation to account for the nonuniform collapse in plane size. The growth of the plume interface in the plane $y/H_t=3$ is depicted in Figure (59), while isobars at the stations $x/H_t=3.04$, 3.75, 4.99 and 6.43 are depicted in Figures (60) - (63) respectively.

H. Double Module Nozzle-Exhaust Flowfield - For this case, the side view is the same as that depicted in Figure (56), while the top view is illustrated in Figure (64). Initial conditions at the combustor exit are the same

ORIGINAL PAGE IS OF POOR QUALITY

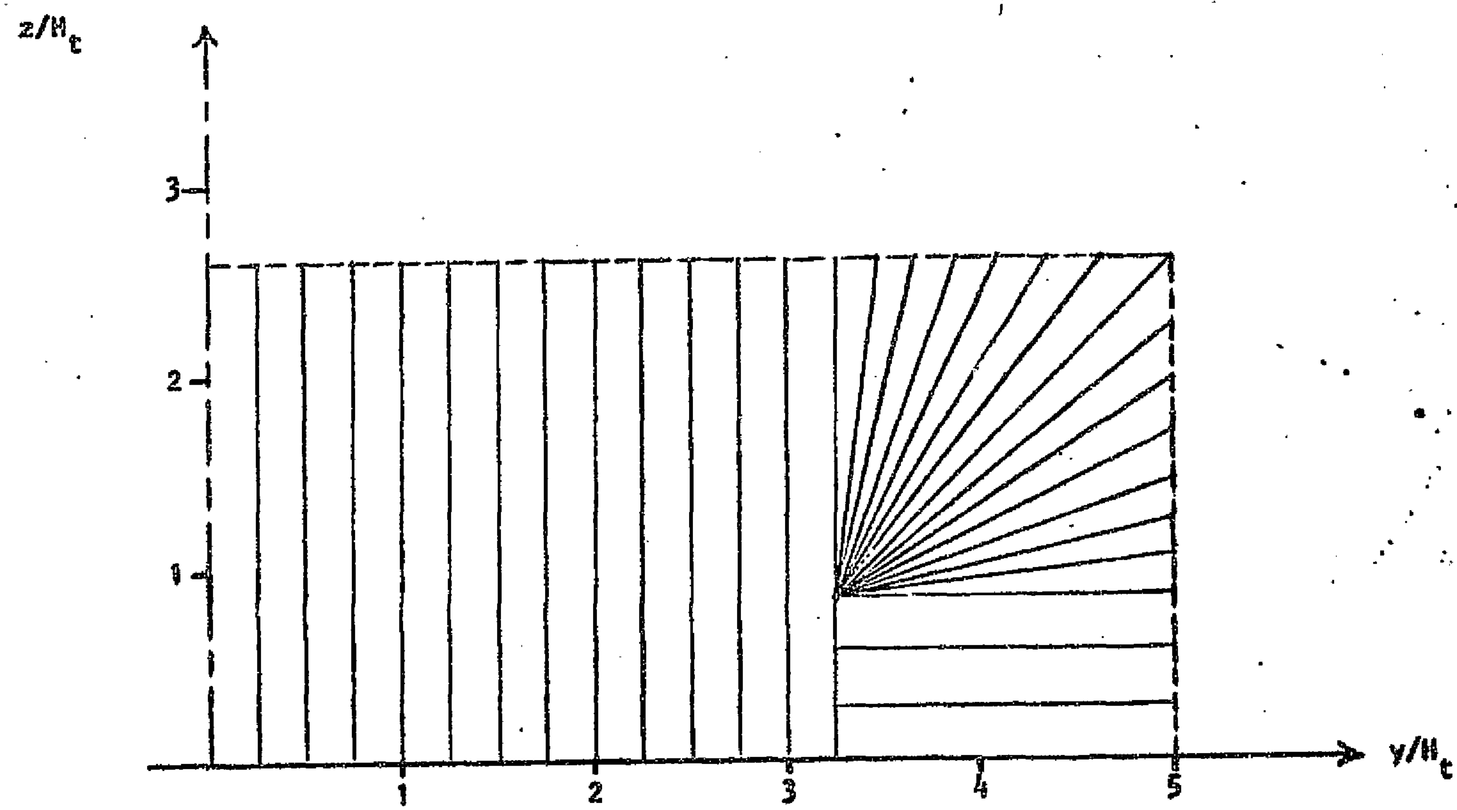

FIGURE 57. SINGLE MODULE REFERENCE PLANE CONFIGURATION

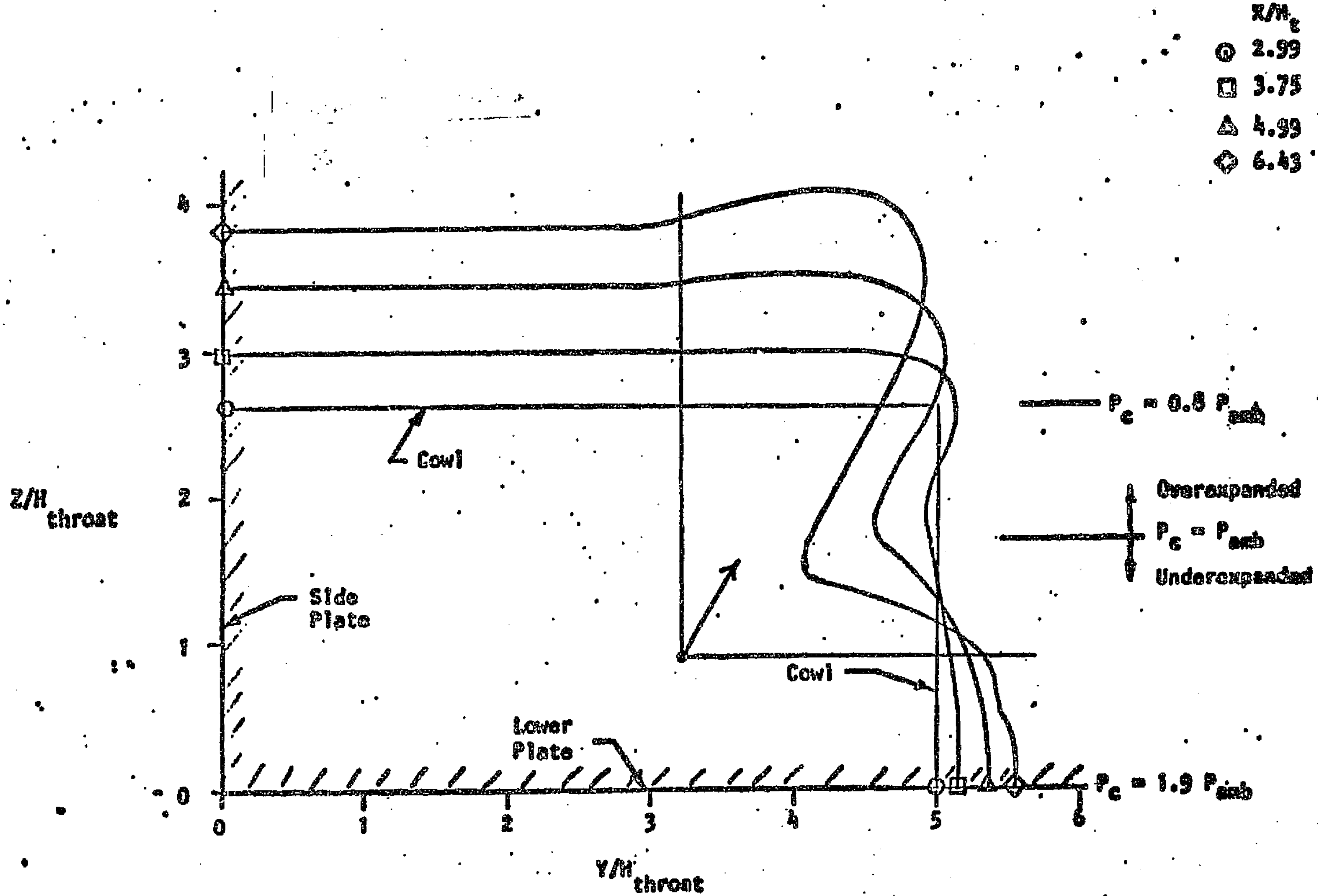

FIGURE 58. SINGLE MODULE, INTERFACE LOCATIONS

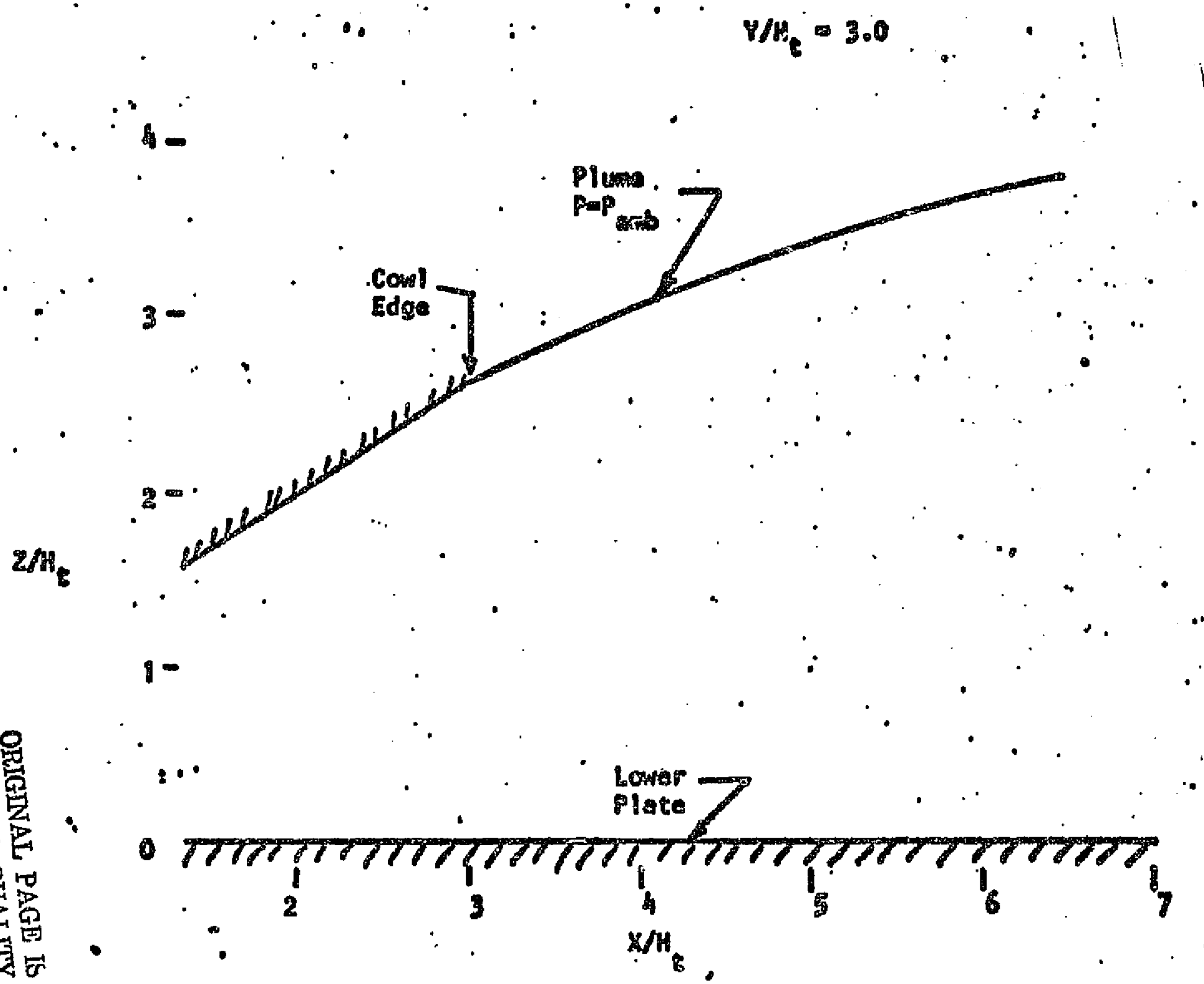

FIGURE 59. SINGLE MODULE INTERFACE TRACE IN THE REFERENCE PLANE $y/H_t = 3.0$

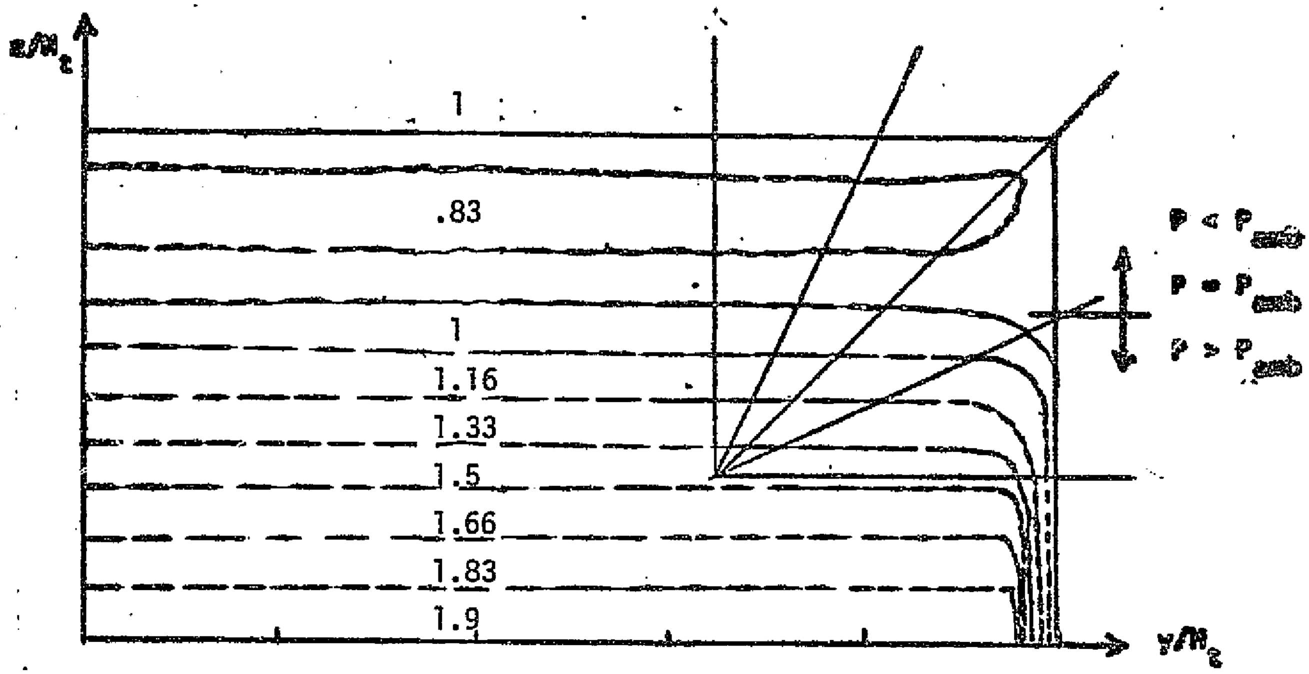

FIGURE 60. SINGLE MODULE ISOBARS AT x/H_t = 3.04

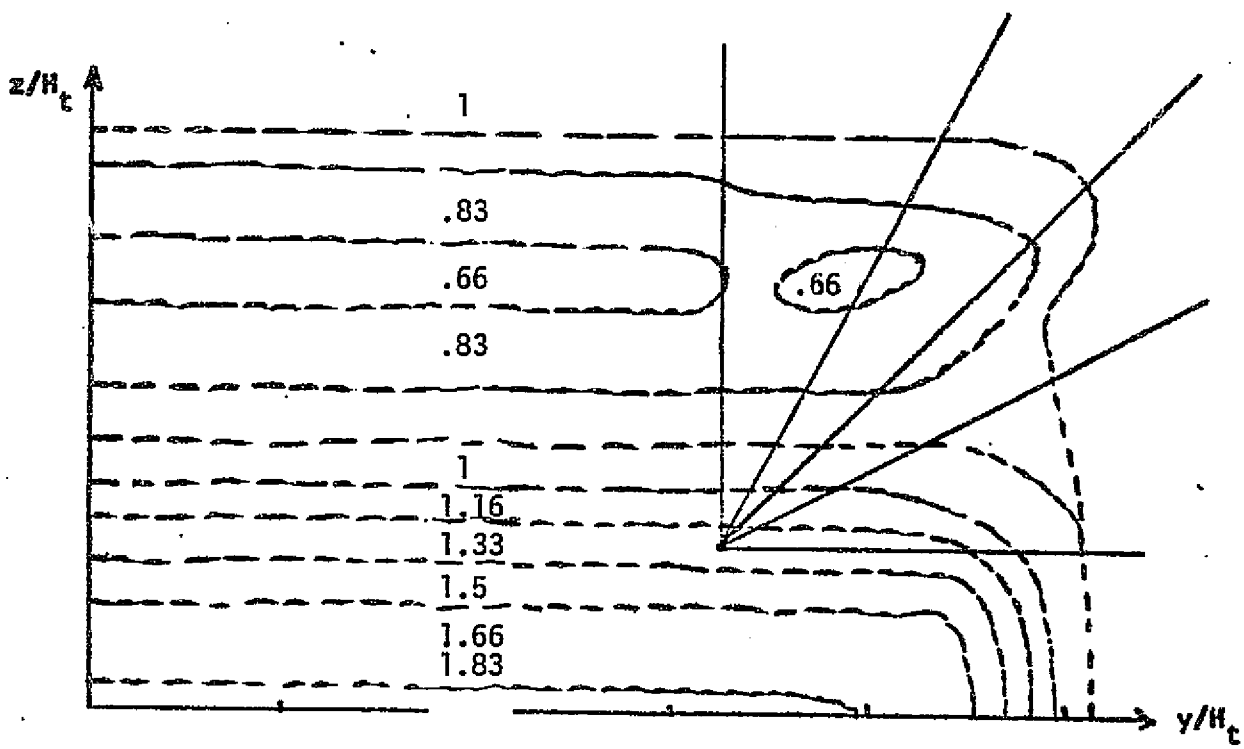

FIGURE 61. SINGLE MODULE ISOBARS AT x/H_t = 3.75

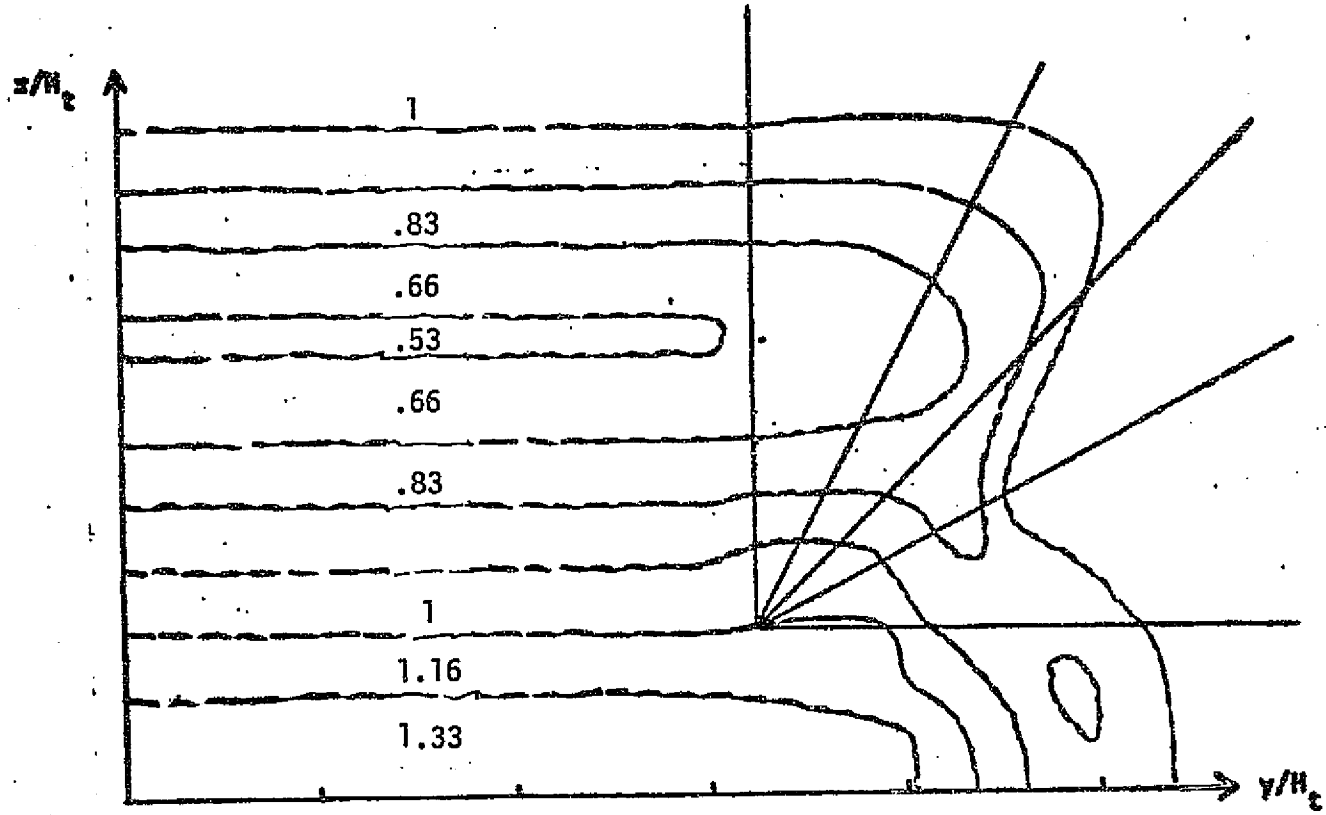

FIGURE 62. SINGLE MODULE ISOBARS AT $x/H_t = 4.99$

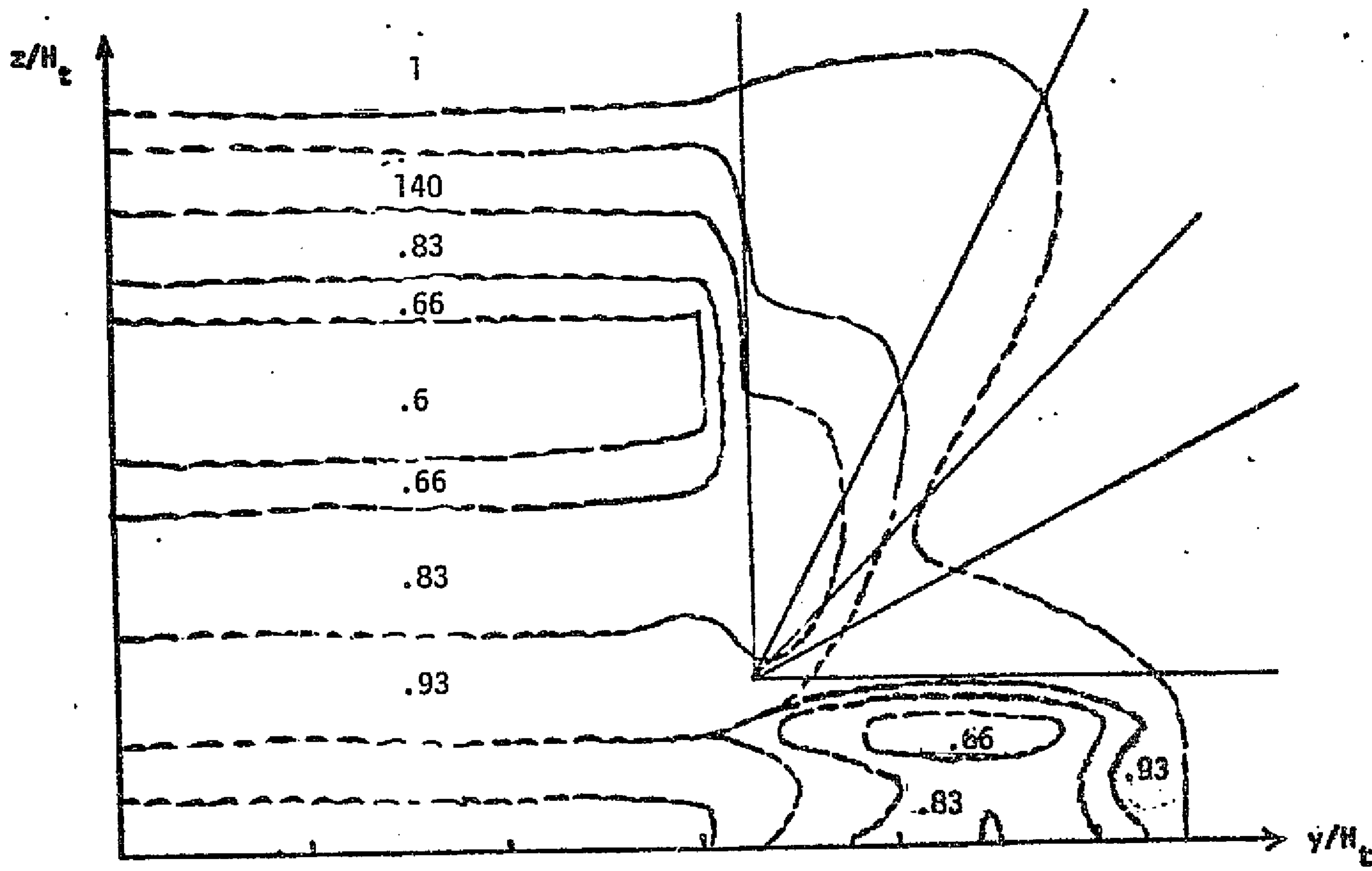

FIGURE 63. SINGLE MODULE ISOBARS AT $x/H_t = 6.43$

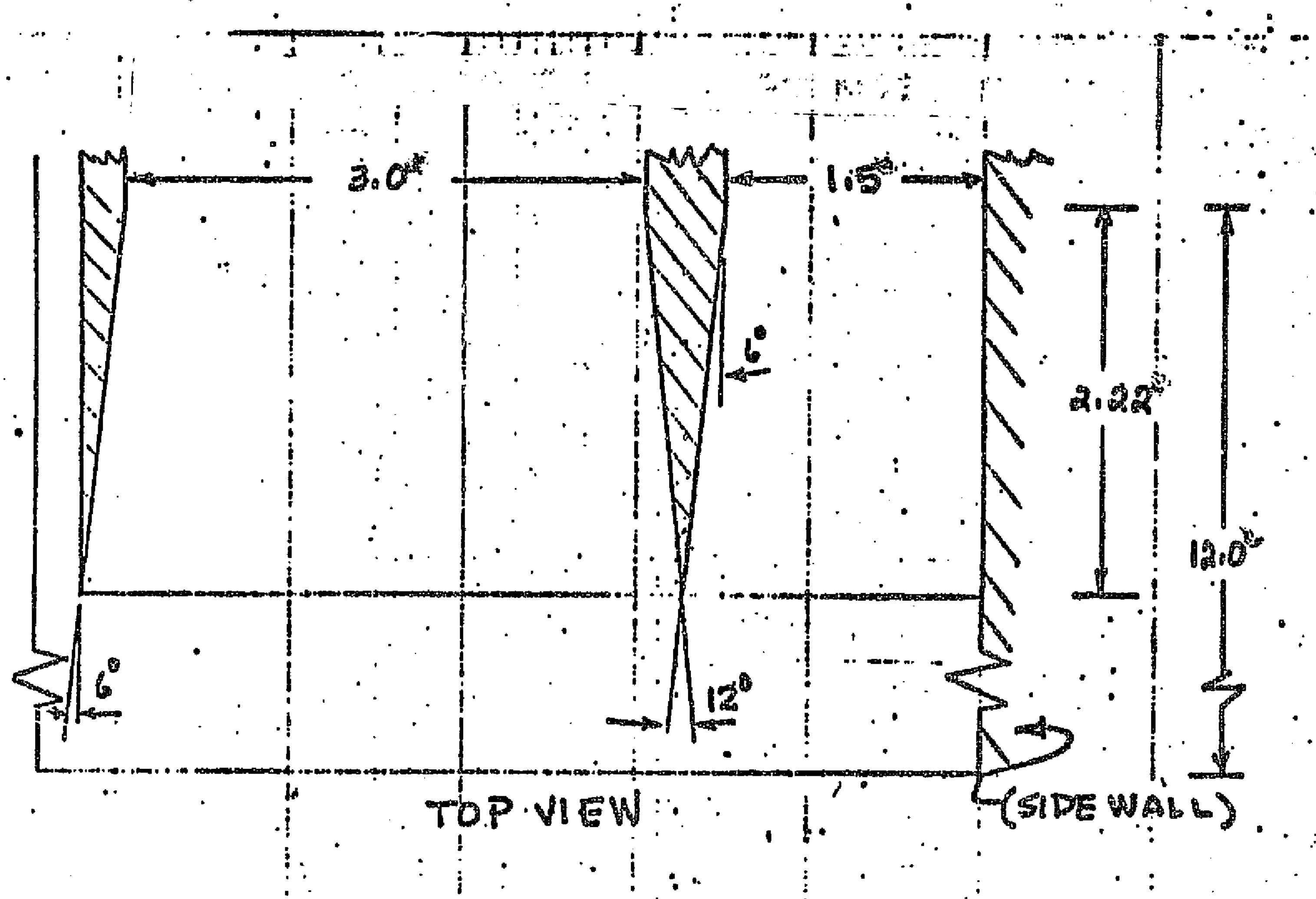

FIGURE 64. GEOMETRIC CONFIGURATION FOR DOUBLE MODULE CASE

as for the single module case except for the pressure ratio P_E/P_∞ which is now 10.5. Resultant plume shapes are depicted in Figure (65). While the ability to calculate such complex flowfields is demonstrated, the results indicate the requirement for major modifications in grid control procedures.

It should be noted that this flowfield was calculated on a one-shot basis. Program BIGMAC calculated the internal flowfields for each of these modules employing a line source reference plane system up to the cowl trailing edge station ($x/Z_t = 3.7$) and automatically interpolated the exit plane results for the two modules in a Cartesian framework and proceeded with the calculation of the exhaust plume flowfield. The initial angle of the contact surface separating the exhaust flow from the quiescent stream is explicitly calculated as described in Section IIIF. The intermediate interaction process is also explicitly calculated. The locally two-dimensional interaction pressure and flow deflection are computed on either side of the module juncture. In addition, at the module juncture-cowl intersection solution computed above. Thus, in this test case the cowl plume at the module juncture experiences a diminished level of overexpansion and possibly a slight underexpansion as a result of the module interaction. At present, in lieu of an exact conical solution, at the cowl module juncture, the procedure described above appears acceptable. However, detailed asymptotical conical solutions for this problem should be obtained.

An interesting comparison is made in Figure (66) employing a discrete floating shock technique as reported in Reference (22). The calculations are for the impingement region of two initially uniform rectangular jets expanding to background conditions. The comparison, which is meant to be qualitative , shows strikingly similar plume shapes, including the plume kink and sharp peak. The results of Reference (22), while preliminary, do lend credibility to the intermodule interaction flowfield as computed herein.

Pressure contours at the cowl trailing edge station ($x/Z_t = 3.7$) as well as the axial stations $x/Z_t = 4.77$, 6.14 and 9.99 are presented in Figures (67) - (70), respectively.

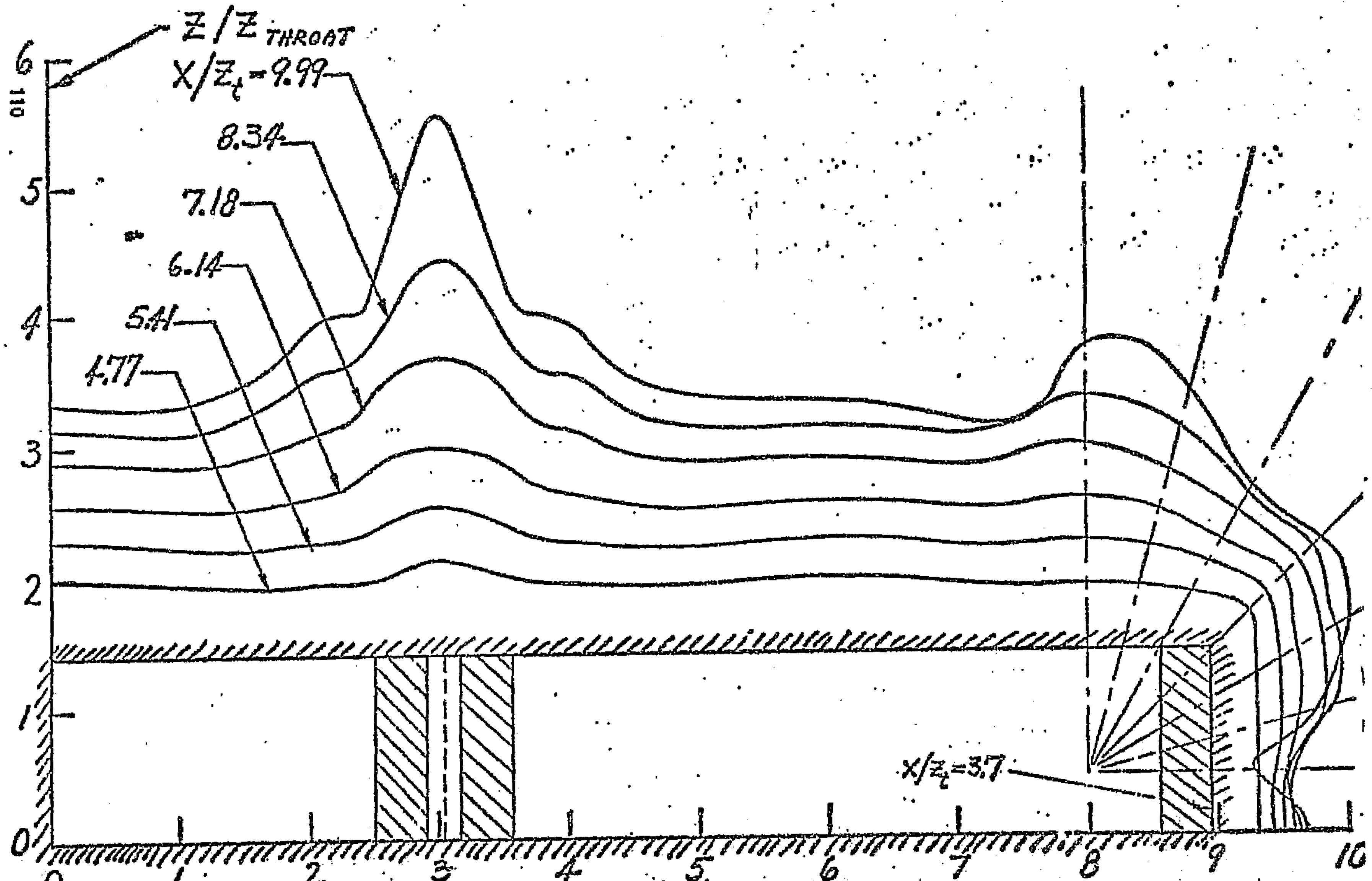

FIGURE 65. RESULTANT INTERFACE CONTOURS FOR DOUBLE MODULE CASE

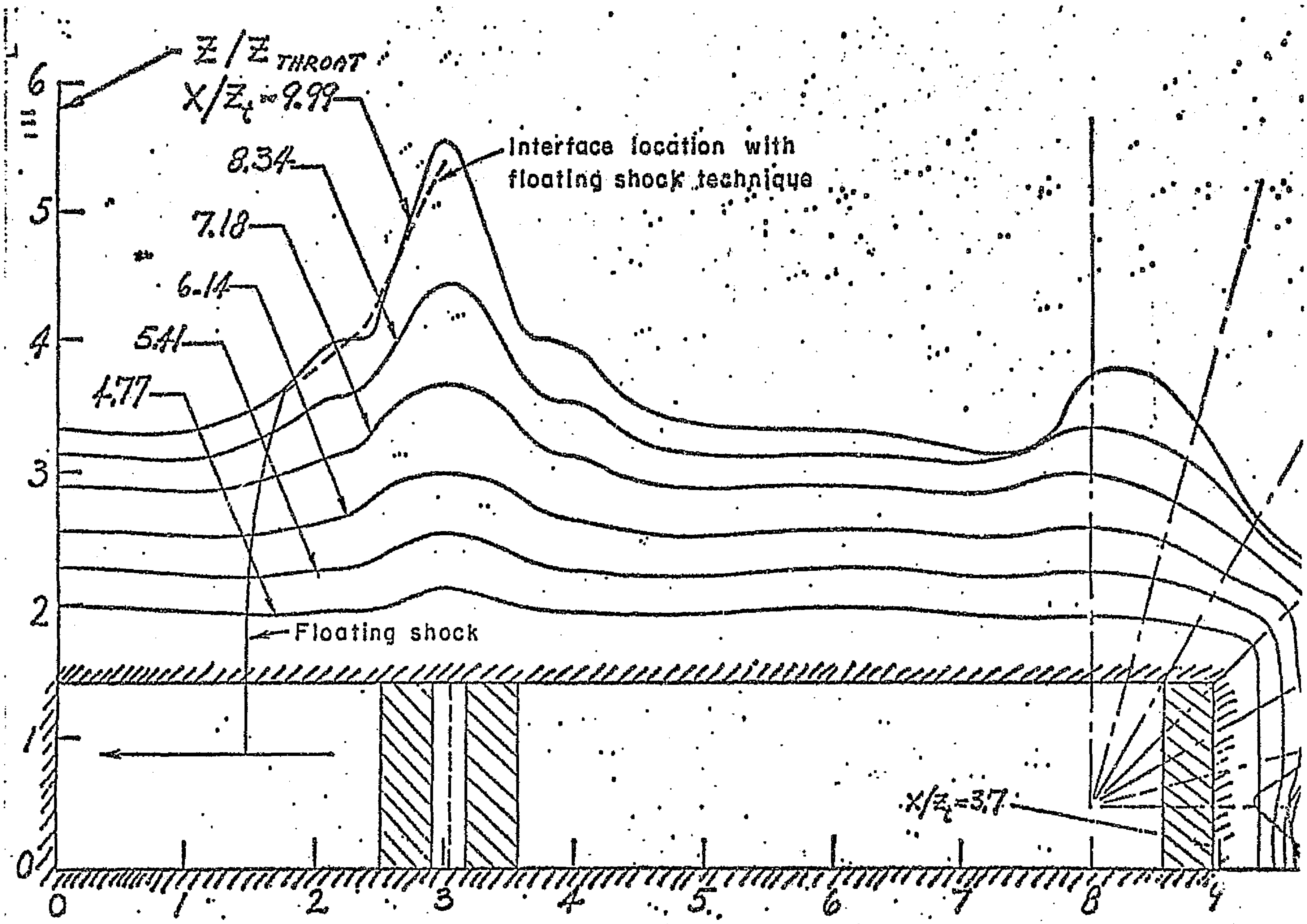

Figure 66. Comparison With Floating Shock Technique for Multiple Plume Impingement.

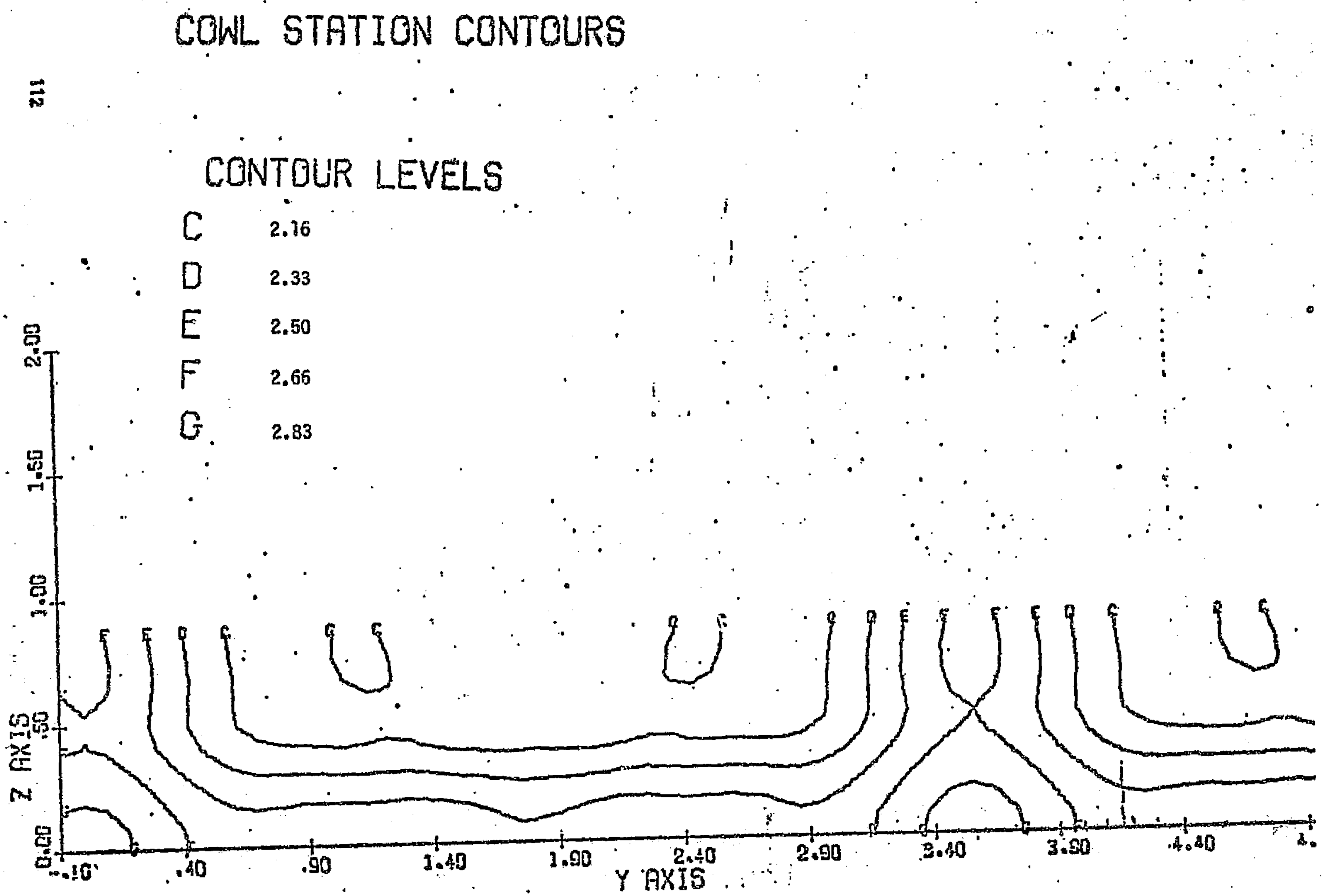

FIGURE 67. PRESSURE CONTOURS AT COWL EXIT PLANE (x/Z_t = 3.7), DOUBLE MODULE CASE

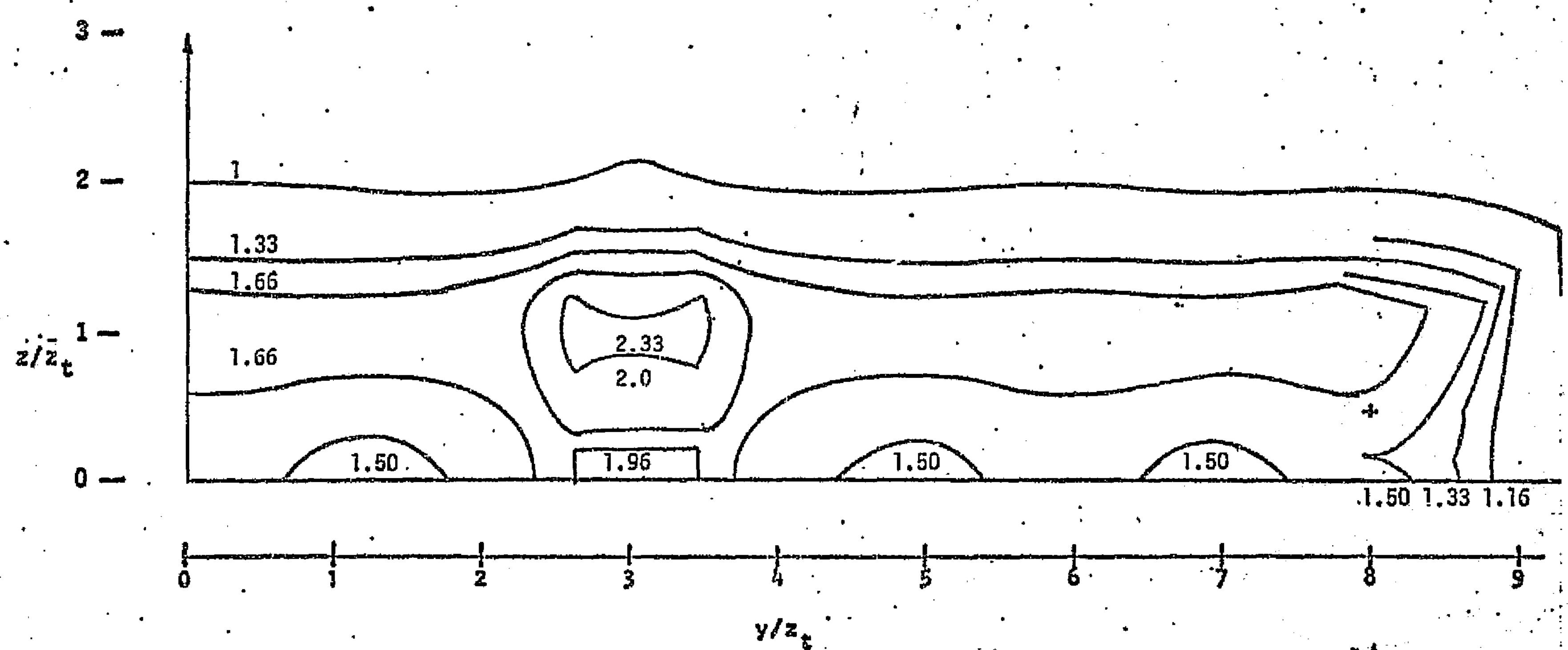

FIGURE 68. PRESSURE CONTOURS AT $x/Z_t = 4.77$, DOUBLE MODULE CASE

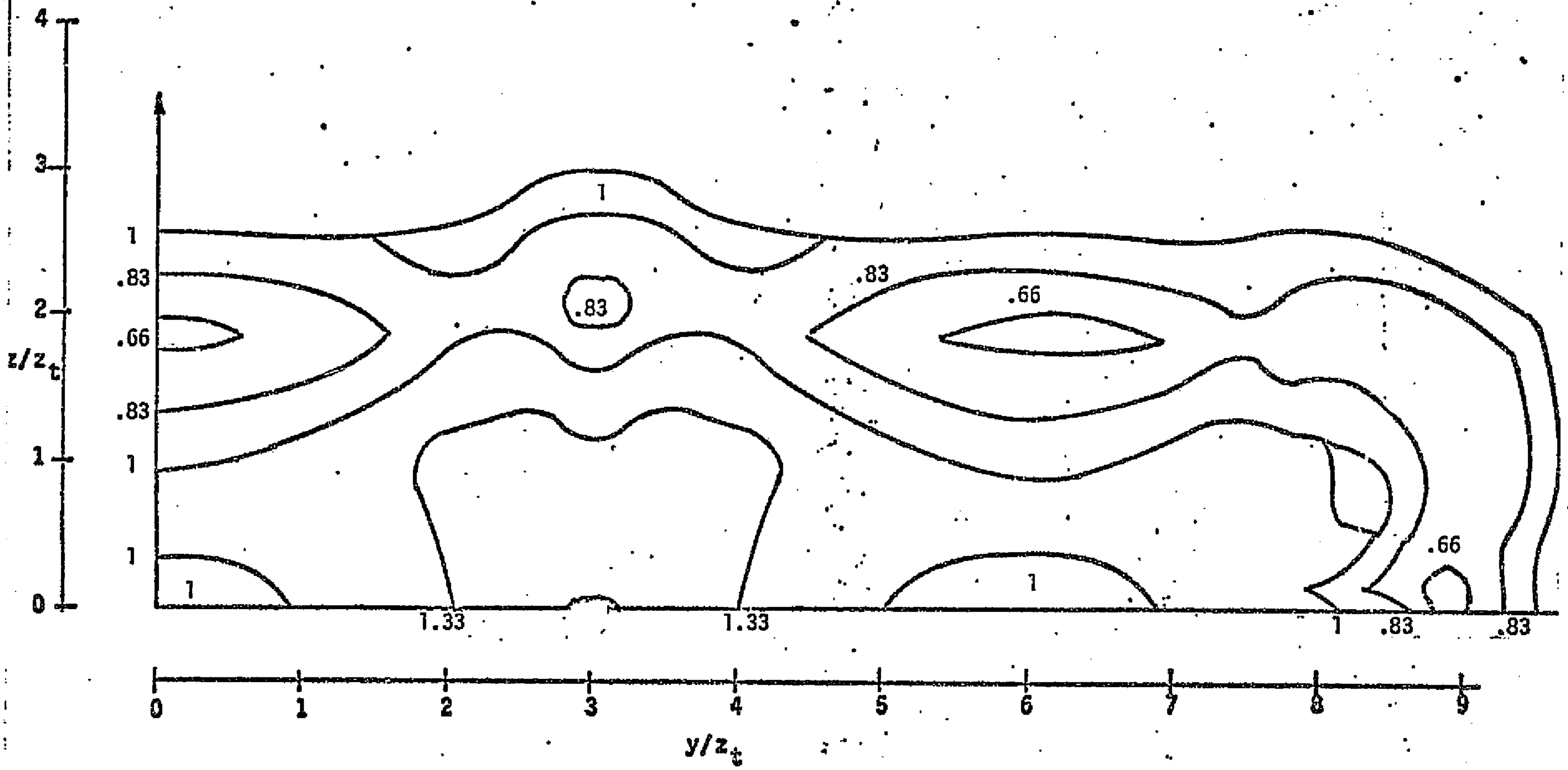

FIGURE 69. PRESSURE CONTOURS AT x/Z_t = 6.14, DOUBLE MODULE CASE

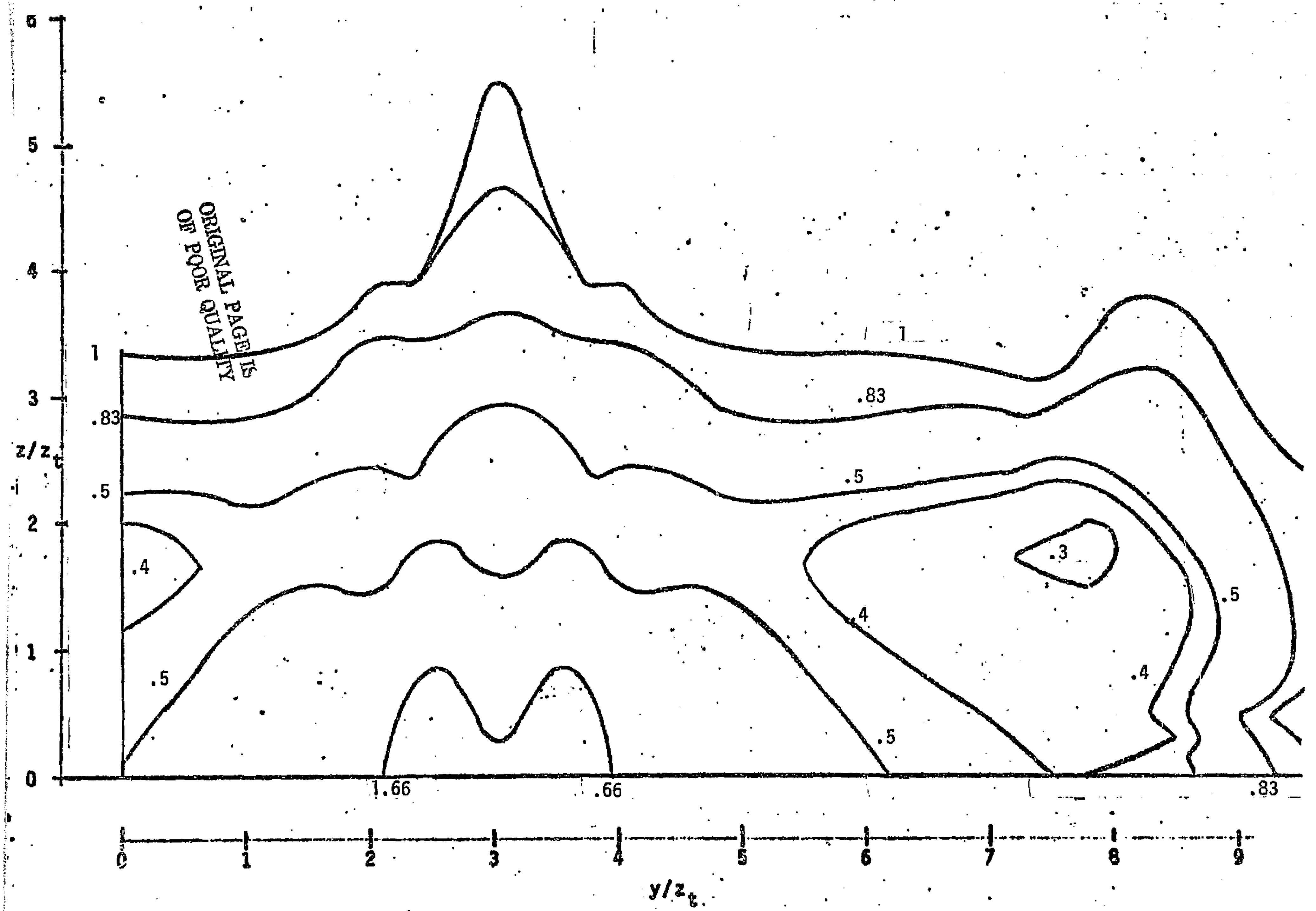

FIGURE 70. PRESSURE CONTOURS AT x/Z_t = 9.99, DOUBLE MODULE CASE

V. CONCLUDING REMARKS

Programs BIGMAC and CHAR3D have been developed to provide predictive computational tools for the analysis of supersonic three-dimensional nozzle-exhaust flowfields. Preliminary applications of these codes to a variety of two and three-dimensional situations indicates that the performance level is quite satisfactory for this purpose. Both codes have demonstrated the ability to capture shock waves in the reference plane and to predict the shocks propagation pattern even after multiple wall and shock interactions. Program BIGMAC has demonstrated this ability in complex three-dimensional situations wherein the interaction of shock waves from mutually perpendicular boundaries has been calculated.

A comparison of these two codes indicates that BIGMAC provides non-preferential treatment of general three-dimensional flows while CHAR3D is better catered to flows with wave systems propagating predominantly in the reference planes. Difficulties have been encountered with CHAR3D in attempts to analyze flows with strong shock systems travelling normal to the reference planes. This is attributable to the basic reference plane characteristic approach wherein cross flow derivatives are treated as forcing functions in the integration step. If these forcing function terms are large and changing rapidly along the streamlines (as is the case for cross flow shocks), the approach tends to breakdown. For such flows, BIGMAC is clearly the preferable code

The effectiveness of these codes is largely attributed to the treatment of the boundaries. All boundary points are analyzed by a characteristic procedure in reference planes which attempts to include the local boundary normal. For corner flows, a redundant approach employing two perpendicular sets of reference planes has proven quite effective.

Initial attempts at analyzing the flowfields downstream of the cowl exit plane has led to the requirement for several modifications to the current approach. In particular, complex conical interactions occur at the juncture of mutually perpendicular trailing edges. It is suggested that these localized interaction flowfields be individually solved by subroutines built into these codes. The converged solutions may then be incorporated into the overall numerical grid system, thus eliminating the requirement for an overly refined grid network in these interaction regions. In addition, a "floating" cylindrical origin appears necessary for the wraparound network in the vicinity of the end module exhaust, and additional grid control techniques are required in the region downstream of the intermodule wedge trailing edges.

The success obtained in the preliminary calculations performed to date clearly supports useage of these codes in future studies. The models developed are by no means limited to the calculation of nozzle-exhaust flows. Program SUPFAN (Reference 17) is a revised edition of Program BIGNAC which calculates the three-dimensional flowfield equations in a supersonic fan stage. Similar modifications can extend the applicability of these models to more generalized three-dimensional situations.

REFERENCES

1. Sedney, R., "The Method of Characteristics. Nonequilibrium Flows, Part II," Marcel Dekker, Inc., New York, (1970).

2. Abett, M. J., "Boundary Conditions Calculational Procedures for Inviscid Supersonic Flowfields," AIAA Computational Fluid Dynamics Conference Proceedings, July 1973.

3. Dash, S. and Del Guidice, "Three-Dimensional Nozzle Exhaust Flowfield Analysis by a Reference Plane Technique," AIAA Paper No. 72-704, June 1972.

4. Dash, S. and Del Guidice, P., "Analysis and Design of Three-Dimensional Supersonic Nozzles, Vol. I," NASA CR-132350, (1972).

5. Edwards, C. L. W., Small, W. J. and Weidner, J. P., "Studies of Scramjet/Airframe Integration Techniques for Hypersonic Aircraft," AIAA Paper No. 75-58, January 1975.

6. Small, W. J., Weidner, J. P. and Johnston, P. J., "Scramjet Nozzle Design and Analysis as Applied to a Highly Integrated Research Airplane," NASA TM X-71972, (1974).

7. Guy, R., et.al., "Thermal Design and Analysis of a Hydrogen Burning Wind Tunnel Model of an Airframe Integrated Scramjet," NASA TM X-73931, (1976).

8. Rakich, J. V., "Three-Dimensional Flow Calculation by the Method of Characteristics," AIAA J., Vol. 5, No. 10, (1967).

9. Katskova, O. N. and Chuskin, P. L., "Three-Dimensional Supersonic Equilibrium Flow of Gas Around Bodies at Angle of Attack," NASA TT F-9790, (1965).

10. Rakich, J. V. and Kutler, P., "Comparison of Characteristics and Shock Capturing Methods with Application to the Space Shuttle Vehicle," AIAA Paper No. 72-191, January 1972.

11. Dash, S. and Kalben, P., "Three-Dimensional Surface Representation and Interpolation Procedure Employing Cubic Spline Functions," ATL TR-193, January 1974.

12. Dash, S. and Del Guidice, P., "Numerical Methods for the Calculation of Three-Dimensional Nozzle Exhaust Flowfields," Paper in Aerodynamic Analysis Requiring Advanced Computers, NASA SP-347, March 1975.

13. Barnes, B., McIntyre, R. W. and Sims, J. A., "Properties of Air Combustion Products with Kerosine and Hydrogen Fuels," Published by Bristol Siddley Engines Ltd. on behalf of Group for Aerospace R&D, (1967).

14. MacCormack, R. W., "The Effect of Viscosity in Hypervelocity Impact Cratering," AIAA Paper No. 69-354, (1969).

15. Kutler, P., Lomax, and Warming, "Computation of Space Shuttle Flow-Fields Using Non-Centered Finite Difference Schemes," AIAA Paper No. 69-354, 1972.

16. Kutler, P. and Shankar, V., "Internal and External Corner Flows," Paper in Aerodynamic Analyses Requiring Advanced Computers, NASA SP-347, March 1975.

17. Ranlet, J., "Description of FØRTRAN Program SUPFAN for the Analysis of the Steady, Inviscid Three-Dimensional Flow in a Supersonic Fan Stage, ATL TM 199, April 1977.

18. Salas, M., "Shock Fitting Method for Complicated Two-Dimensional Supersonic Flows," AIAA J., Vol. 14, No. 5, May 1976.

19. Shankar, V. S. V., "Numerical Solutions for Inviscid Supersonic Corner Flows,: AIAA Paper No. 75-221, January 1975.

20. Nangia, P. K., "Three-Dimensional Wave Interactions in Supersonic Intakes," 2nd Inter'l Symposium on Air Breathing Engines, Sheffield, England, March 1974.

21. Charwat, A. F. and Redekeopp, L. G., "Supersonic Interference Flow along the Corner of Intersecting Wedges," AIAA J., Vol. 5, No. 3, March 1974.

22. Rudman, S., "Multinozzle Plume Flow Fields - Structure and Numerical Calculation," AIAA Paper No. 77-710, June 1977.

APPENDIX A

CURVE FITS FOR Γ, h and ρ

The variation of Γ (the equilibrium value of γ) as a function of temperature (T), pressure (P) and equivalence ratio (Φ) is presented graphically in Figures (A1, A2, & A3), from values tabulated in Reference (4). In Figure (A1) it can be seen that Γ is a strong function of T over the temperature range of interest, while the effect of varying composition is small by comparison. Moreover, Figure (A1) indicates that Γ is moderately sensitive to pressure and the degree of sensitivity increases substantially as the temperature level increases and dissociation effects become important.

As a result of these observations, temperature is the primary independent variable, while pressure is the secondary independent variable and composition acts as a perturbation variable. Thus, we can fit the function Γ (T,P,Φ) with a polynomial in T and add on a temperature dependent correction term for the effect of pressure and a temperature independent correction term for the effect of Φ.

An examination of Figure (A1) suggest that the function Γ (T) can best be curve fit by breaking up the temperature range into three intervals such that the function can be represented by a parabola in each range. Choosing $p = 10^5$ pascal and $\phi = 1$ as our base we, therefore, find three functions

$$\Gamma_1(T,10^5,1) = -1.833\times10^{-7}\,T^2 + 7.5\times10^{-5}\,T + 1.367 \tag{1}$$

$$\Gamma_2(T,10^5,1) = 2.0\times10^{-8}\,T^2 - 1.38\times10^{-4}\,T + 1.423 \tag{2}$$

$$\Gamma_3(T,10^5,1) = 7.27\times10^{-8}\,T^2 - 4.57\times10^{-4}\,T + 1.85 \tag{3}$$

and define the basic temperature function as

$$\Gamma(T,10^5,1) = \begin{Bmatrix} \Gamma_1(T,10^5,1) \\ \Gamma_2(T,10^5,1) \\ \Gamma_3(T,10^5,1) \end{Bmatrix} \quad \text{for} \quad \begin{Bmatrix} T \le 500^\circ K \\ 500 \le T \le 2000^\circ K \\ T \ge 2000^\circ K \end{Bmatrix} \tag{4}$$

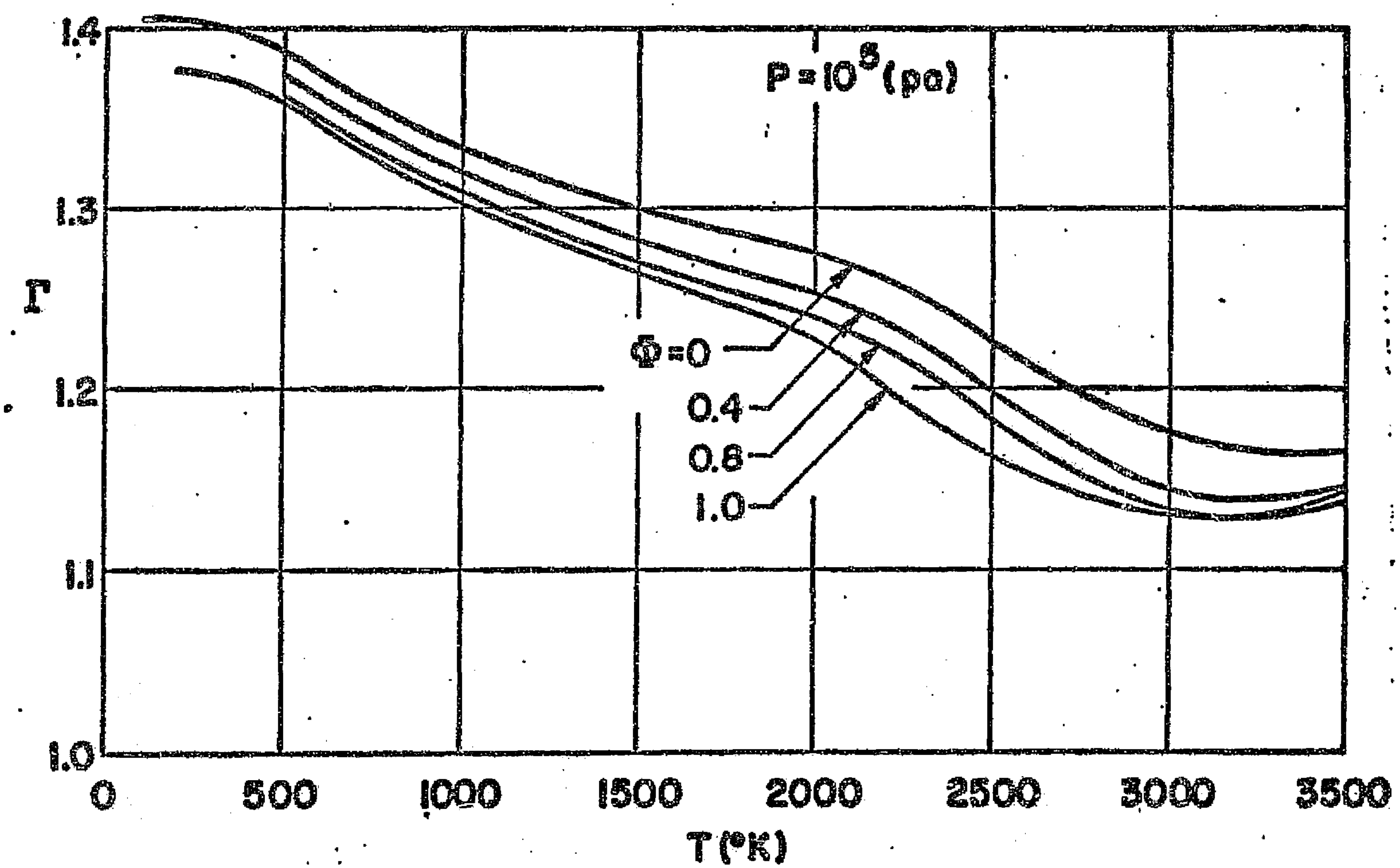

FIGURE A1. Γ VARIATION WITH TEMPERATURE

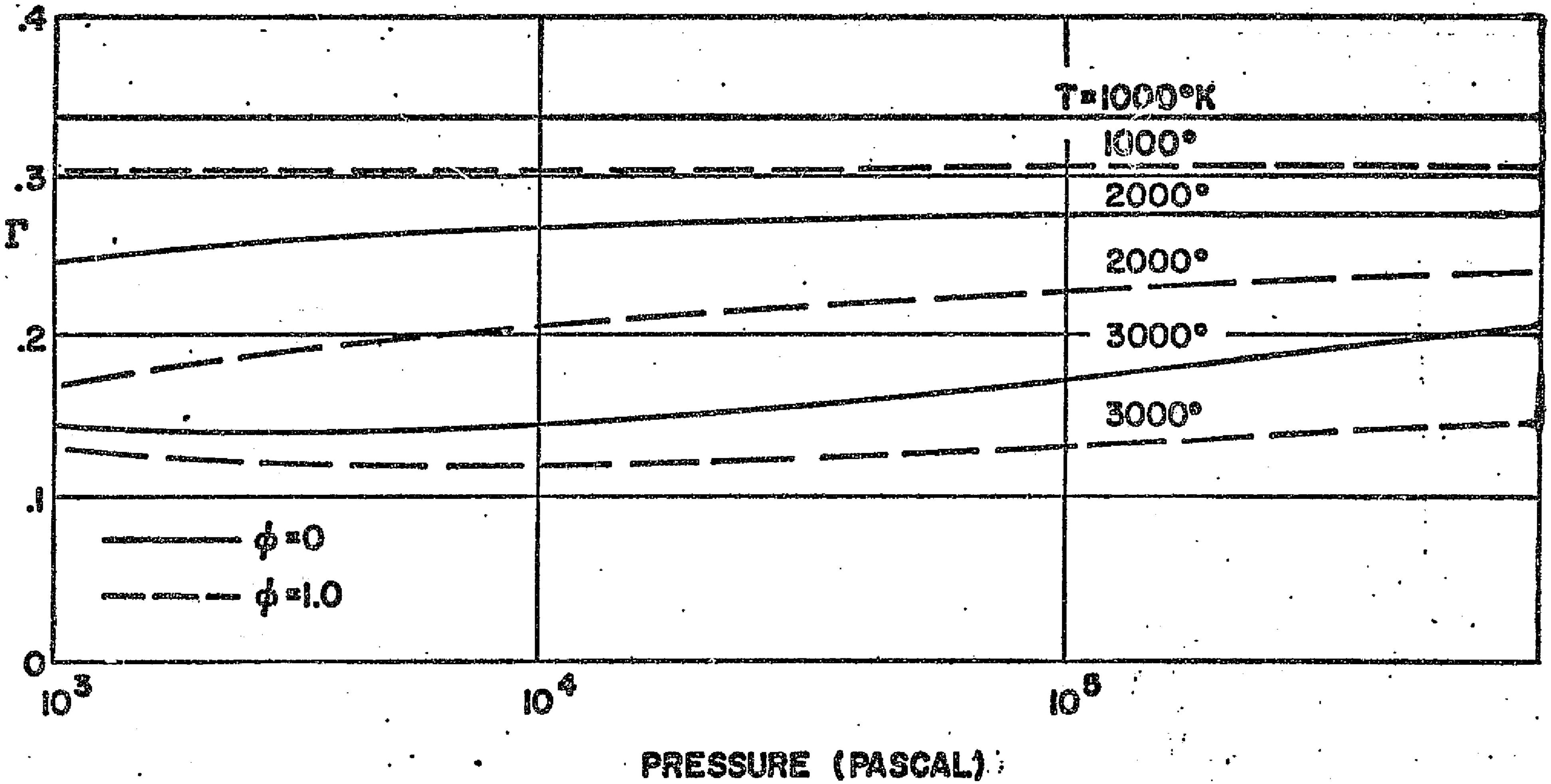

FIGURE A2. Γ VARIATION WITH PRESSURE

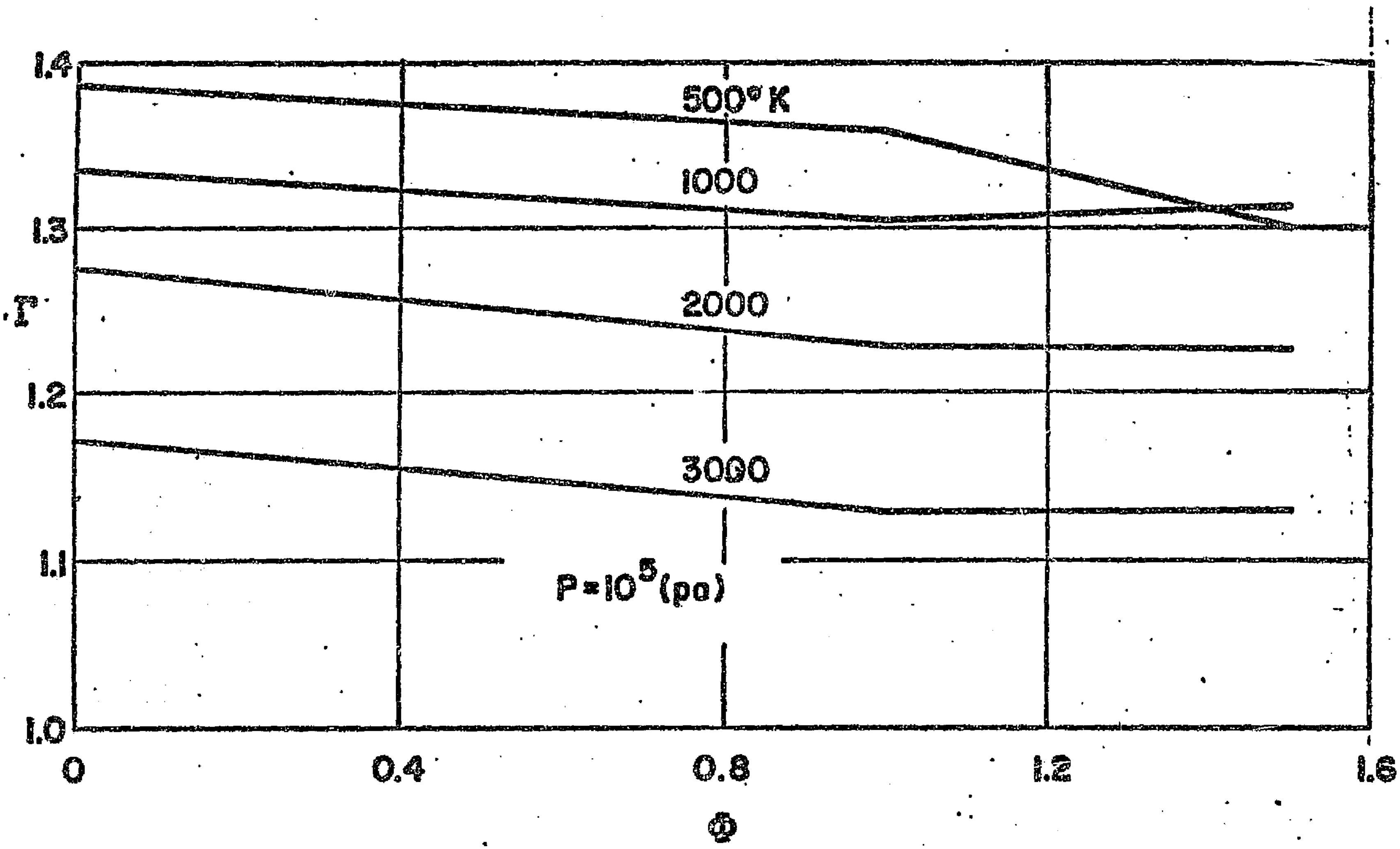

FIGURE A3. Γ VARIATION WITH Φ

Figure (A3) indicates that $\frac{\partial \Gamma}{\partial \Phi}$ is constant in the two ranges $\Phi < 1$ and $\Phi > 1$, but is a function of T. Fitting the function $\frac{\partial \Gamma}{\partial \Phi}$ in each of the ranges of ϕ we obtain

$$\frac{\partial \Gamma}{\partial \Phi} = \begin{bmatrix} n_1(T) \\ n_2(T) \end{bmatrix} \text{ for } \begin{bmatrix} \Phi \leq 1 \\ \Phi \geq 1 \end{bmatrix} \tag{5}$$

where

$$n_1(T) = 4\times10^{-9}\, T^2 - 2\times10^{-5}\, T - 0.019 \tag{6}$$

$$n_2(T) = 3.39\times10^{-2}\, T^{0.5} - 3.91\times10^{-4}\, T - 0.681 \tag{7}$$

This now defines Γ as a function of both temperature and Φ by means of the equation

$$\Gamma(T,10^5,\Phi) = \Gamma(T,10^5,1) + (\Phi - 1)\,\frac{\partial \Gamma}{\partial \Phi} \tag{8}$$

Finally, the effect of pressure must be included. From Figure (18) we observe that Γ may be approximated as

$$\Gamma(T,P,\Phi) = \Gamma(T,10^5,\Phi) + m\,[\log_{10}(p\times10^5) - 5] \tag{9}$$

where m is a function of T. Deriving m, we find

$$m = \begin{Bmatrix} 0 \\ -2.15\times10^{-8}\, T^2 + 0.91\times10^{-4}\, T - 0.0695 \end{Bmatrix} \text{ for } \begin{Bmatrix} T < 1000^oK \\ T \geq 1000^oK \end{Bmatrix} \tag{10}$$

Summarizing, the final function obtained is

$$\Gamma(T,P,\Phi) = \Gamma(T,10^5,1) + m\left(\frac{\ln p}{2.3} - 5\right) + \frac{\partial \Gamma}{\partial \Phi}\,(\Phi - 1) \tag{11}$$

where the functions $\Gamma(T,10^5,1)$, $\frac{\partial \Gamma}{\partial \Phi}$ and m are given by Equations (4), (5) and (10) respectively.

The curve fit for enthalpy is derived in a similar way. Figures (A4) & (A5) present the variation of h with temperature, pressure and equivalence ratio. As

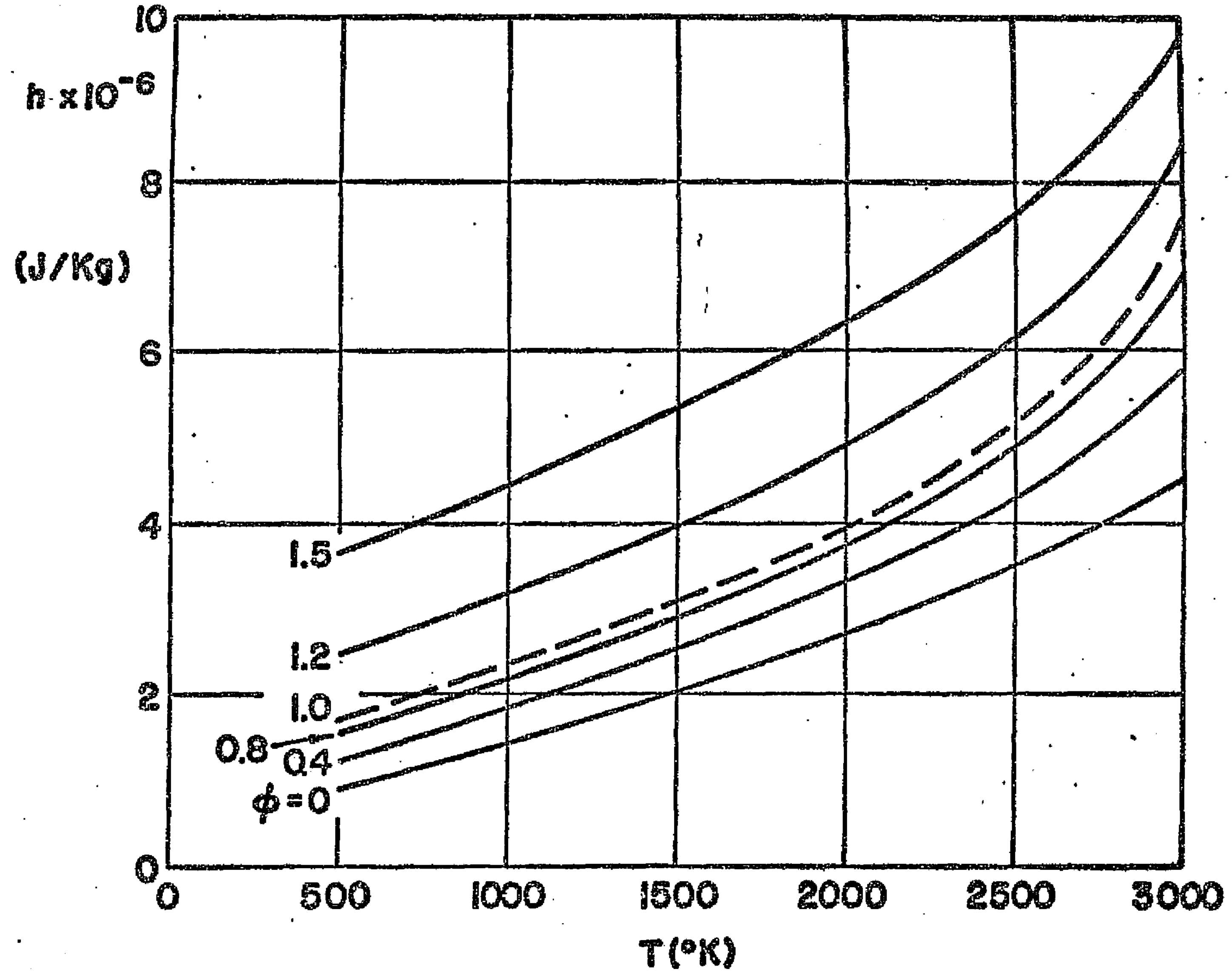

FIGURE A4. ENTHALPY AS A FUNCTION OF TEMPERATURE ($p=10^5$pa.)

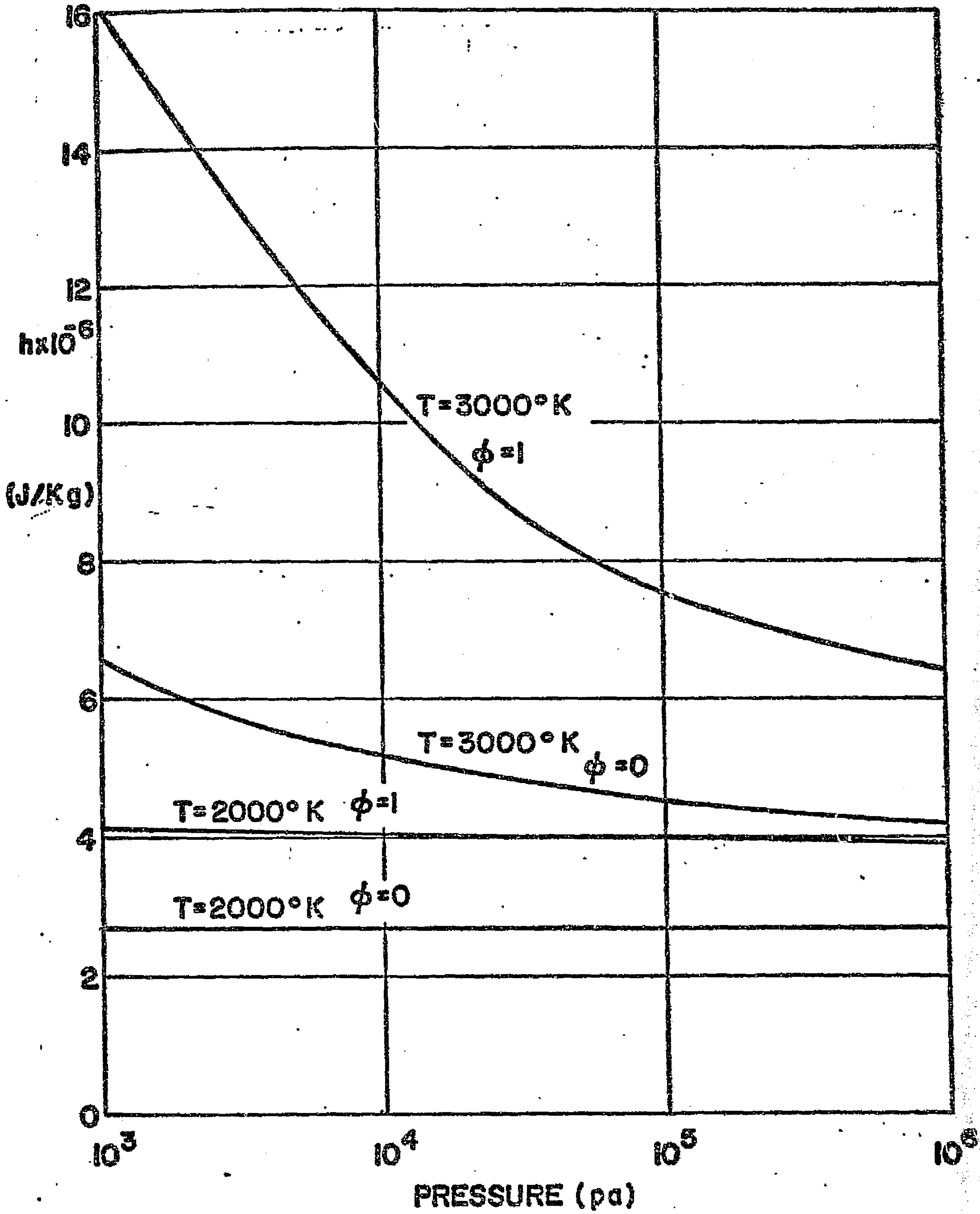

FIGURE A5. ENTHALPY AS A FUNCTION OF PRESSURE.

was the case for T, the function $h(T,\phi,p)$ is fit by a quadratic function of T, the coefficients of which are functions of ϕ and an additive terms for the effects of pressure. The resulting curve fit is summarized below.

$$h(T,\phi,p) = \begin{Bmatrix} h(T,\phi,10^5) \\ h(T,\phi,p) \end{Bmatrix} \quad \text{for} \quad \begin{Bmatrix} T \leq 2000^\circ K \\ T > 2000^\circ K \end{Bmatrix} \tag{12}$$

where $h(T,\phi,p) = h(T,\phi,10^5)\ 1 +$

$$\left[\frac{(1+\phi)\ (T-2000)}{2000} \left(.125\ \left(\frac{\ln p}{2.3} - 5\right)^2 - .275\ \left(\frac{\ln p}{2.3} - 5\right)\right)\right] \tag{13}$$

The basic function $h(T,\phi,10^5)$ is defined as

$$h(T,\phi,10^5) = 10^6(a_1T^2 + b_1T + c_1) \tag{14}$$

with the coefficients a_1, b_1 and c_1 defined below:

for $T \leq 2000^\circ K$ and $\phi \leq 1$

$$a_1 = 10^{-7}(-.1042\phi^2 + .8242\phi + .987)$$

$$b_1 = 10^{-3}(.01167\phi^2 + .1503\phi + .938) \tag{15}$$

$$c_1 = -.0284\phi^2 + .6731\phi + .4293$$

for $T \leq 2000^\circ K$ and $\phi > 1$

$$a_1 = 10^{-7}(1.787\phi^2 - 5.48\phi + 5.4)$$

$$b_1 = 10^{-3}(-.1867\phi^2 + 1.11\phi + .176) \tag{16}$$

$$c_1 = -.0933\phi^2 + 3.975\phi - 2.808$$

for $T > 2000^{\circ}K$ and $\phi \leq 1$

$$\left.\begin{aligned} a_1 &= 10^{-6}(1.792\phi^2 + .3983\phi + .310) \\ b_1 &= 10^{-3}(-9.05\phi^2 - .07917\phi + .245) \\ c_1 &= 10.86\phi^2 - .1183\phi + .970 \end{aligned}\right. \tag{17}$$

for $T > 2000^{\circ}K$ and $\phi > 1$

$$\left.\begin{aligned} a_1 &= 10^{-6}(4.81\phi^2 - 13.9\phi + 11.59) \\ b_1 &= 10^{-3}(-23.08\phi^2 + 66.82\phi - 52.61) \\ c_1 &= 27.05\phi^2 - 73.73\phi + 58.39 \end{aligned}\right. \tag{18}$$

When the inverse function $T(h,\phi,p)$ is required, it is obtained by an iterative solution of Equations (12) through (18).

The density is found by obtaining a curve fit for the mixture molecular weight and using the equation of state

$$\rho = \frac{pm}{\bar{R}T} \tag{19}$$

where $\bar{R}$ is the universal gas constant and m is the molecular weight.

The behavior of m with T, p and ϕ is illustrated in Figures (A6) & (A7). We see that for temperatures less than $2000^{\circ}K$, m is essentially independent of temperature. The discontinuity in slope of $m(\phi)$ shown in Figure (A7) requires that the equivalence ratio range be split in two. Thus,

for $T \leq 2000^{\circ}K$

$$m(\phi) = \begin{Bmatrix} 1.53\phi^2 - 5.895\phi + 28.955 \\ 1.60\phi^2 - 10.6\phi + 33.6 \end{Bmatrix} \quad \text{for} \begin{Bmatrix} \phi \leq 1 \\ \phi > 1 \end{Bmatrix} \tag{20}$$

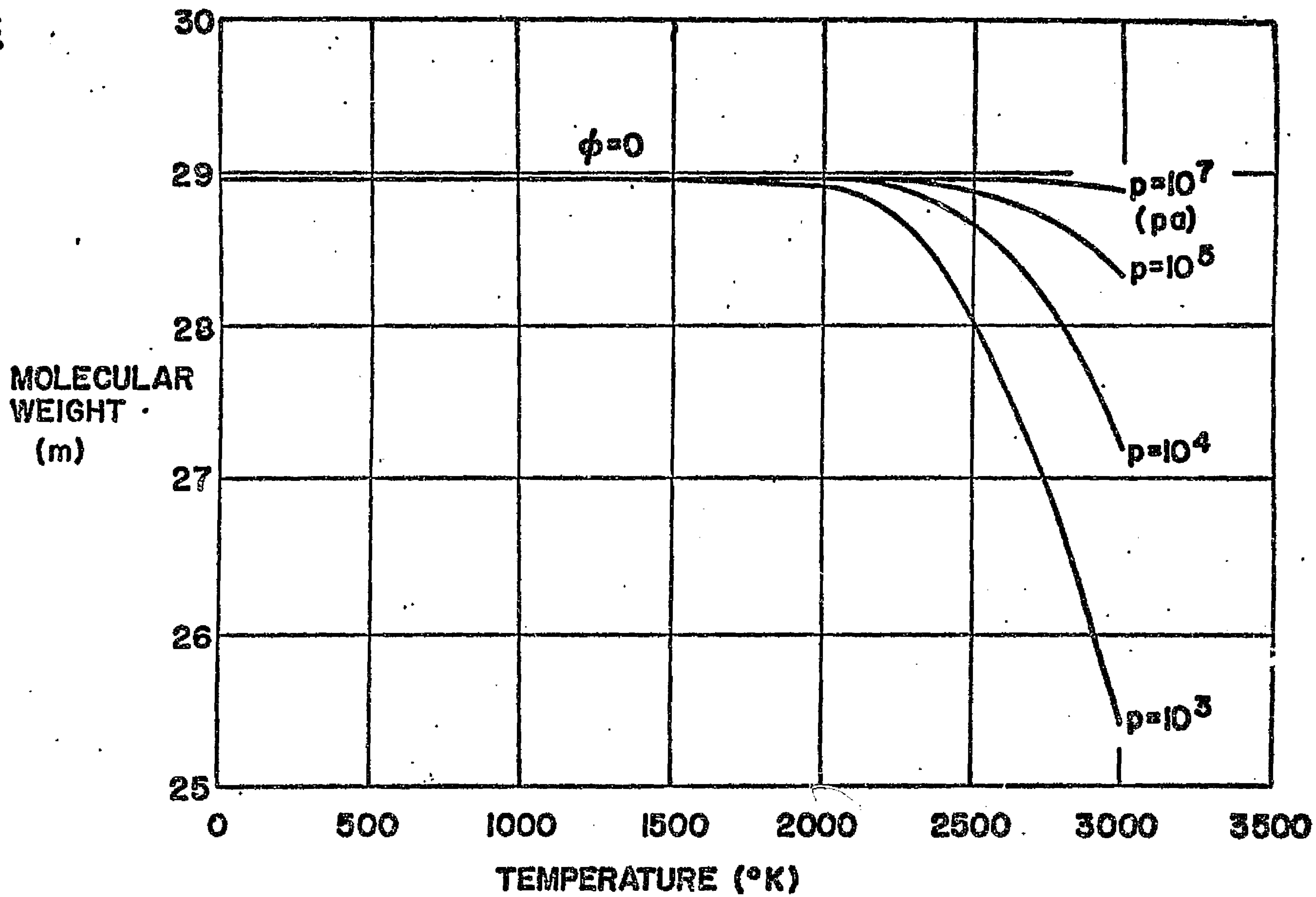

FIGURE A6. MOLECULAR WEIGHT AS A FUNCTION OF TEMPERATURE AND PRESSURE.

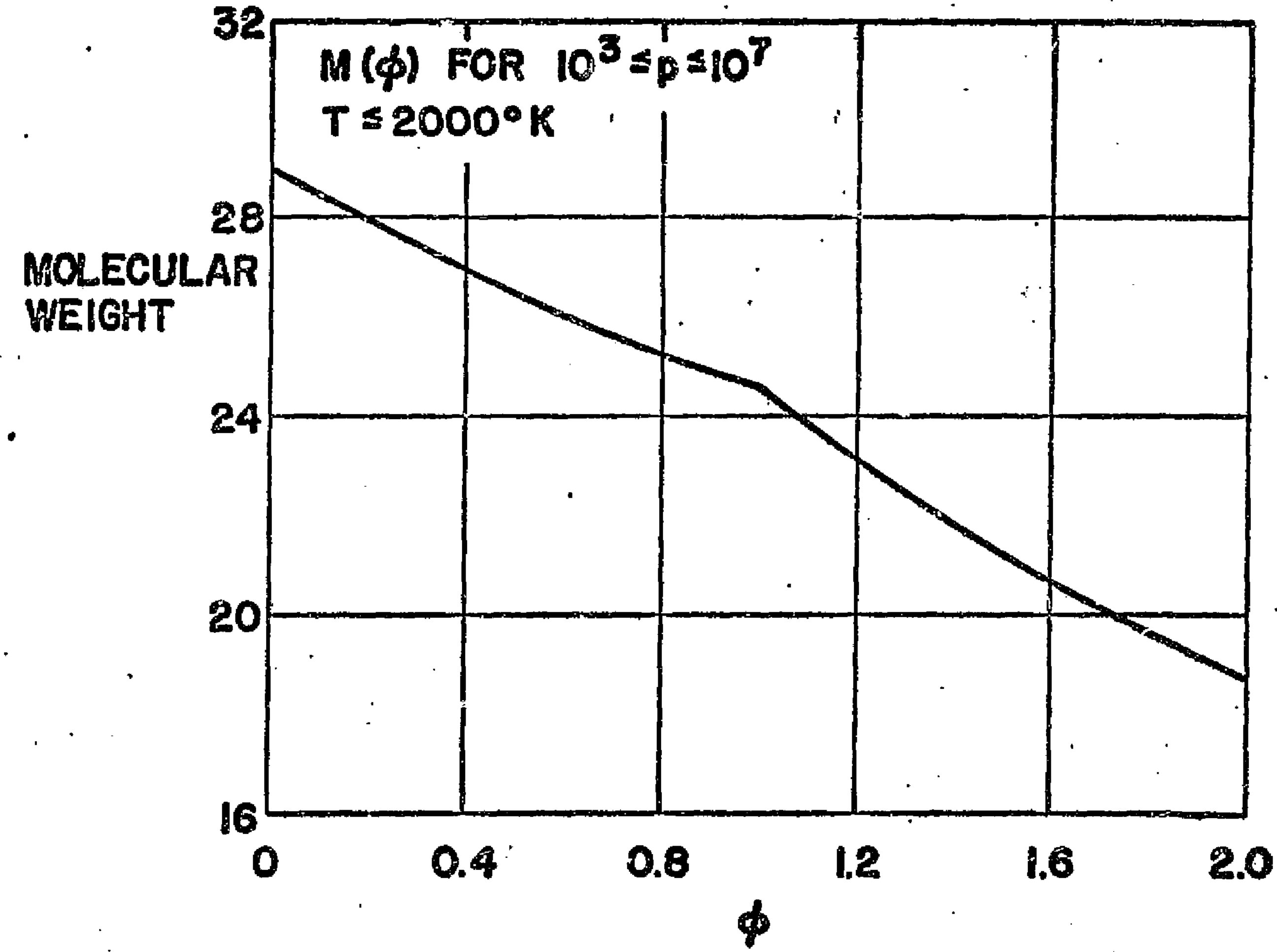

FIGURE A7. MOLECULAR WEIGHT AS A FUNCTION OF EQUIVALENCE RATIO FOR $T \le 2000^\circ K$.

For the higher temperature range, it is convenient to employ the form

$$m = m(\phi) - \delta(p,\phi,T) \tag{21}$$

where

$$\delta = d_2(p,\phi) \left(\frac{T-2000}{1000}\right)^{n_2(\phi)} \tag{22}$$

and

$$d_2 = a_2 \left(\frac{\ln p}{2.3}\right)^{1.5} + b_2 \left(\frac{\ln p}{2.3}\right) + c_2 \tag{23}$$

for

$$0 \leq \phi \leq 1 \qquad \begin{aligned} a_2 &= -2.3\phi^2 + 4.01\phi + 1.736 \\ b_2 &= 8.61\phi^2 - 15.42\phi - 6.66 \\ c_2 &= -16.88\phi^2 + 33.21\phi + 14.58 \\ n_2 &= .4375\phi^2 + .0625\phi + 2.08 \end{aligned} \tag{24}$$

and, for

$$1 \leq \phi < 2 \qquad \begin{aligned} a_2 &= -.822\phi^2 + 2.363\phi + 1.905 \\ b_2 &= 2.76\phi^2 - 7.56\phi - 8.68 \\ c_2 &= 3.6\phi^2 + 7.36\phi + 27.15 \\ n_2 &= .47\phi^2 + 1.825\phi + .350 \end{aligned} \tag{25}$$

APPENDIX B

THREE DIMENSIONAL SURFACE REPRESENTATION AND INTERPOLATION PROCEDURES

Consider the three-dimensional continuously differentiable surface $z = f(x,y)$ depicted in Figure (B1), prescribed by contour data in the form $(y_j,z_j)_i$ at discrete values of x_i. Prescription of the data in this form is generally obtainable for most aerodynamic bodies and greatly simplifies the chore of numerically fitting the surface by reducing the problem to the determination of one-dimensional partial cubic splines in two coordinate directions.

Assume that there are J(i) contour data pairs $(y_j,z_j)_i$, $(1 \leq j \leq J(i))$ at I contour stations x_i, $(1 \leq i \leq I)$. The number of contour pairs used to determine the surface and their relative spacing is arbitrary, as is the spacing between contour stations. We seek to determine a surface fit $z = F(x,y)$ that will yield accurate values of the unit surface normal

$$\hat{N} = \frac{i_z - (F_x)_y\, i_x - (F_y)_x \cdot i_y}{(1+(F_x)_y^2 + (F_y)_x^2)^{\frac{1}{2}}} \tag{1}$$

In addition to prescribing the discrete contour data, and conditions must be specified at the bounding surface curves, A, B, C and D. AT boundaries A & B, one would generally stipulate:

$$\left(\frac{\partial z}{\partial y}\right)_x \quad \text{at } j = 1 \text{ or } J(i) \text{ for } i = 1,2, ---, I \tag{2}$$

or partial second derivative ratios

$$\frac{\left(\dfrac{\partial^2 z}{\partial y^2}\right)^x_{i,j=1}}{\left(\dfrac{\partial^2 z}{\partial y^2}\right)^x_{i,j=2}} \quad , \quad \frac{\left(\dfrac{\partial^2 z}{\partial y^2}\right)^x_{i,j(i)}}{\left(\dfrac{\partial^2 z}{\partial y^2}\right)^x_{i,J(i)-1}} \tag{3}$$

At boundaries C & D, one would generally stipulate:

$$\left(\frac{\partial z}{\partial x}\right)_y \quad \text{at } i = 1 \text{ or } I \text{ for } j = 1, 2, ---J(i) \tag{4}$$

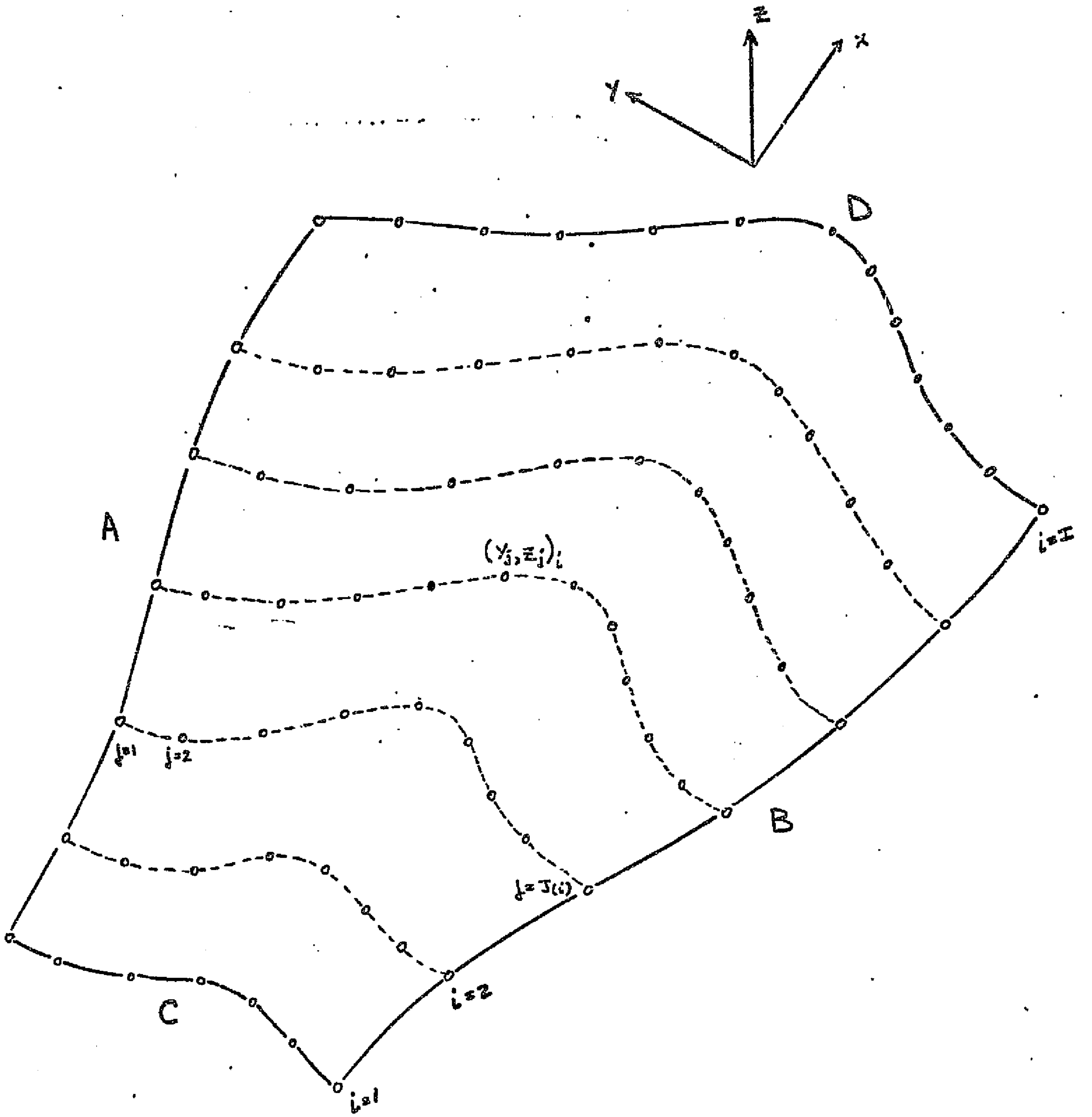

FIGURE B1. THREE-DIMENSIONAL SURFACE DESCRIBED BY DISCRETE CONTOUR DATA or partial second derivative ratios

$$\left(\frac{\partial^2 z}{\partial x^2}\right)_{1,j} y \quad \left(\frac{\partial^2 z}{\partial x^2}\right)_{2,j} y \; , \left(\frac{\partial^2 z}{\partial x^2}\right)_{i,j} y \quad \left(\frac{\partial^2 z}{\partial x^2}\right)_{i-1,j} y \tag{5}$$

It is advantageous to map the surface onto one having rectangular boundaries when projected onto a plane of constant z. This is accomplished by the transformation

$$\begin{aligned} x &= x \\ \eta &= \frac{y-y_{A(x)}}{y_{B(x)}-y_{A(x)}} \\ z &= z \end{aligned} \tag{6}$$

Then, in (x,η,z) coordinates, the surface is bounded by $\eta=o$ (A), $\eta=1$ (B), $x = x_1$ (C) and $x=x_I$ (D). The analysis may be extended to sweptback surfaces as depicted in Figure (B2) which are mapped onto rectangular boundaries when projected onto a plane of constant Z by the transformation

$$\begin{aligned} \xi &= \frac{x-x_{C(y)}}{x_{D(y)}-x_{C(y)}} \\ \eta &= \frac{y-y_{A(x)}}{y_{B(x)}-y_{A(x)}} \\ z &= z \end{aligned} \tag{7}$$

Such a surface fit requires specification of contour data on sweptback contours ξ = constant as shown in Figure (B2) (or alternately on η = constant if this proves more practicable as would be the case for the wing surface of Figure (B3).

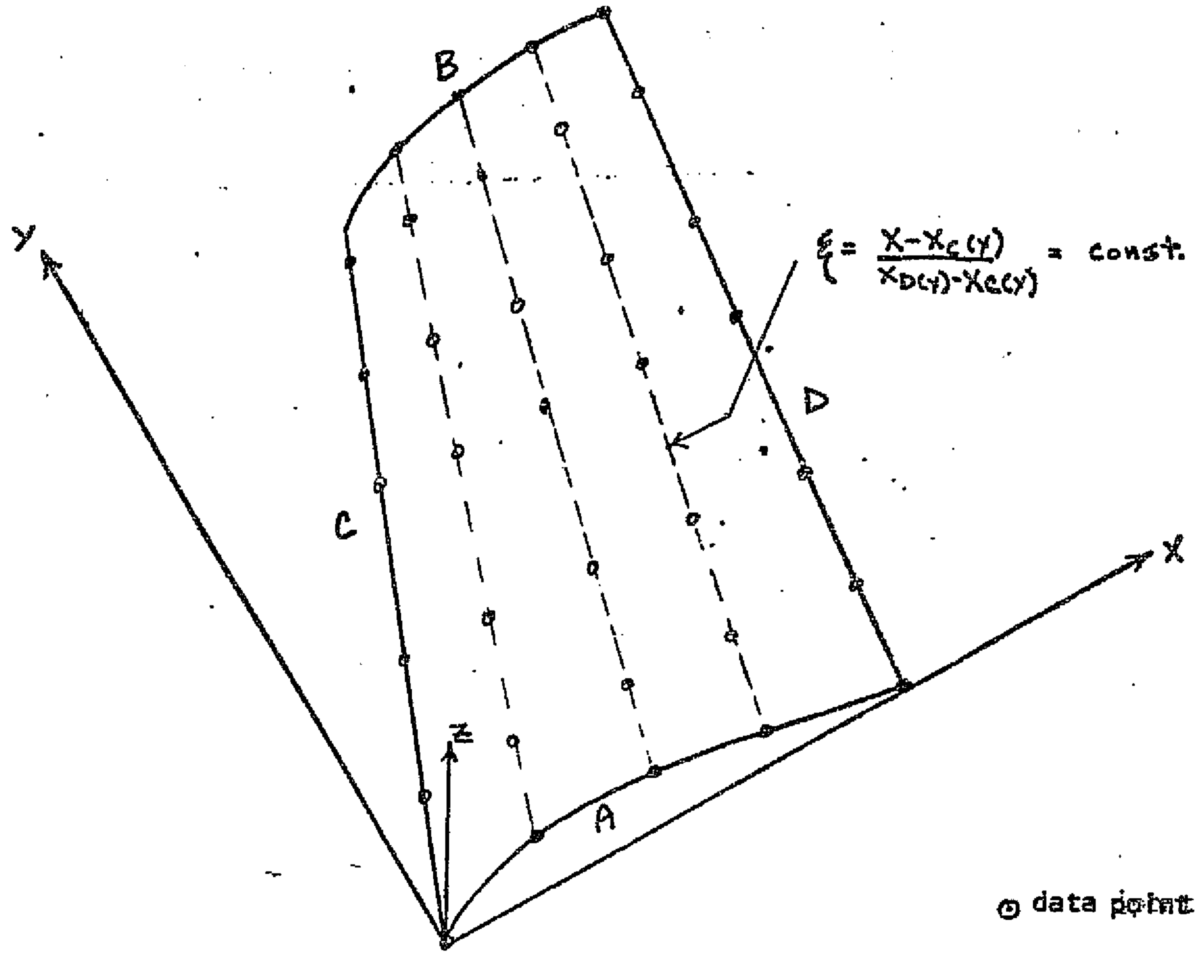

FIGURE B2. SWEPTBACK SURFACE INPUT ARRAY

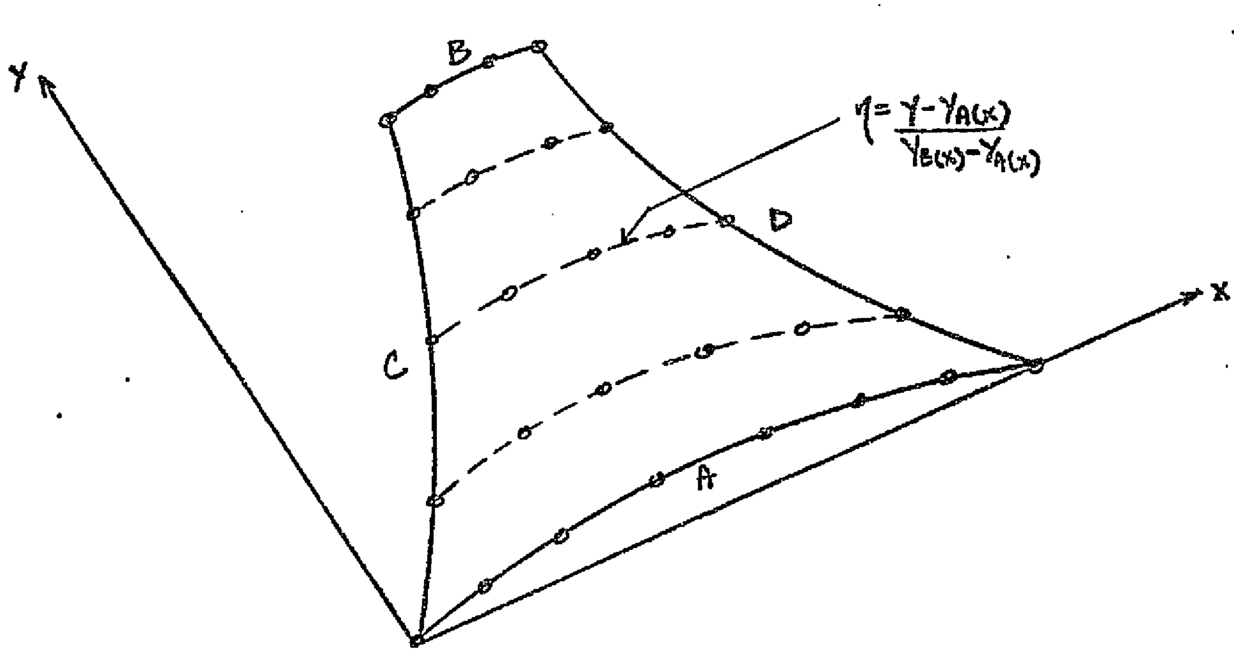

FIGURE B3. ALTERNATE INPUT ARRAY FOR SWEPTBACK SURFACE

For simplicity, we will assume that contour data is prescribed at stations x = constant and we are working in the x,η,z coordinate system given by Equation (6). We require an ordered array of coefficients (which will consist of partial second derivatives) to fit the surface $z = F(x,y)$, analagous to the coefficients M_j of Section II used to fit the curve $y(x)$.

The numerical procedures entailed in obtaining these coefficients are as follows:

(a) We require spline fits for the boundary curves A & B in the form $y_{A(x)}$ and $Y_{B(x)}$ using discrete data pairs $(x_i, y_{(i,1)})$ for A and $(x_i, y_{(i,J(i))})$ for B and a stipulations of end conditions. We obtain these fits employing the procedure outlined in Section II, obtaining coefficients M_{A_i} and M_{B_i} where

$$M_{A_i} = y''_A(x_i) \text{ and } M_{B_i} = y''_B(x_i) \tag{8}$$

(b) We obtain fits of $z(\eta)$ at all contour stations x_i for $(i=1,2,---,I)$ using the contour pairs $(y_{i,j}, z_{i,j})$. This is done as follows for a given station x_i

(1) Obtain the contour pairs in the transformed system, namely $(\eta_{i,j}, z_{i,j})$ employing the transformation given by Equation (6).

(2) Transform the end conditons at A & B. If first derivatives were stipulated, then we would require $(\partial z/\partial\eta)_x$ which is simply

$$\left(\frac{\partial z}{\partial \eta}\right)_{i,j} = \left(\frac{\partial z}{\partial y}\right)_{i,j} \left(y_{B(x_i)} - y_{A(x_i)}\right) \tag{9}$$

$(i=1 \text{ or } I)$

If a ratio of second derivatives was stipulated at the end points, this ratio remains unchanged in the transformed system.

(3) We obtain the coefficients $M\eta_{i,j}$ employing the one-dimensional method of Section II where

$$M\eta_{i,j} = \left(\frac{\partial^2 z}{\partial \eta^2}\right)_{i,j}^{x} \tag{32}$$

(c) We now wish to obtain values of the coefficients M_η on a new grid spacing such that the spacing in the variable is the same for every contour (independent of i) as shown in Figure (B4) although not necessarily evenly spaced. Let η_k denote the specified η grid for k=1,2——K. Then, values of the dependent variable z are obtained using the relation

$$z_{i,k} = M_{\eta_{i,j-1}} \frac{(\eta_{i,j}-\eta_{k,K})^3}{6\Delta\eta_{i,j}} + M\eta_{i,j} \frac{(\eta_k-\eta_{i,j-1})^3}{6\Delta\eta_{i,j}}$$

$$+ \left(z_{i,j-1} - M_{\eta_{i,j-1}} \frac{\Delta\eta^2_{i,j}}{6}\right) \left(\frac{\eta_{i,j}-\eta_k}{\Delta\eta_{i,j}}\right)$$

$$+ \left(z_{i,j-1} - M_{\eta_{i,j-1}} \frac{\Delta\eta^2}{6}{}_{i,j}\right) \left(\frac{\eta_{i,j}-\eta_k}{\Delta\eta_{i,j}}\right) \tag{33}$$

where $\eta_{i,j-1} < \eta_k < \eta_{i,j}$ and $\Delta\eta_{i,j} = \eta_{i,j} - \eta_{i,j-1}$

The coefficients M on the i,n grid are given by

$$M_{\eta_{i,k}} = M_{\eta_{i,j-1}} \left(\frac{\eta_{ij}-\eta_k}{\Delta\eta_{i,j}}\right) + M_{\eta_{i,j}} \left(\frac{\eta_k-\eta_{i,j-1}}{\Delta\eta_{i,j}}\right) \tag{34}$$

ORIGINAL PAGE IS
OF POOR QUALITY

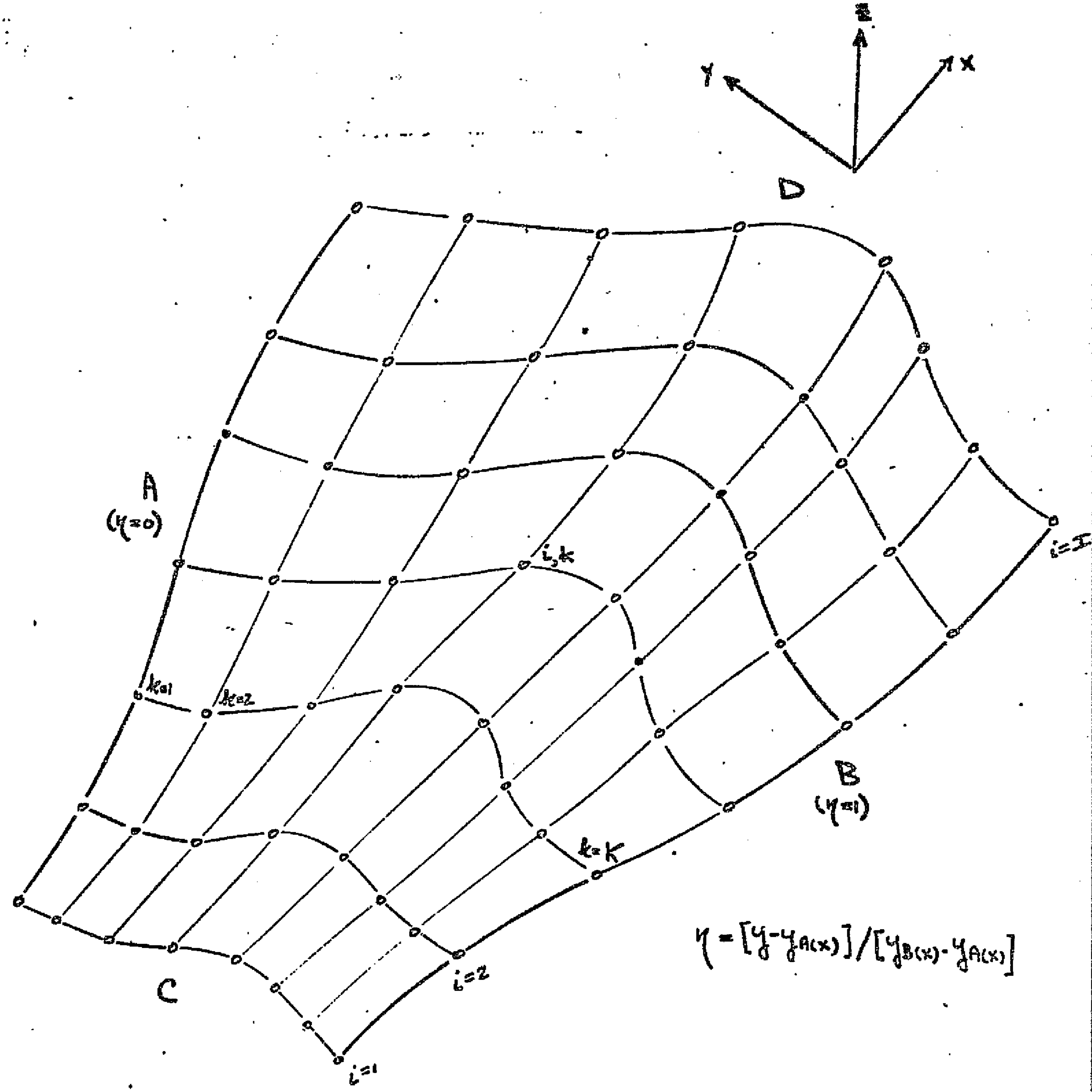

FIGURE B4. ORDERLY GRID ARRAY

(d) We now obtain fits of $Z(x)$ along the lines η_k = constant for ($k = 1,2$ - ——, K) using the contour pairs $(x_i, z_{i,k})$. For η_k = constant this is done as follows:

(1) Transform the end conditions at C and D. If first derivatives were specified, then the derivative $(z_x)_\eta$ is required under which obtained employing the relation:

$$\left(\frac{\partial z}{\partial x}\right)_{\eta_{i,k}} = \left(\frac{\partial z}{\partial x}\right)_{y_{i,k}} + \left(\frac{\partial z}{\partial \eta}\right)_{x_{i,k}} \cdot \frac{(1-\eta_k)Y'_{A(x)} + \eta_k Y'_{B(x)}}{Y_{B(x)} - Y_{A(x)}} \tag{13}$$

where $\left(\frac{\partial z}{\partial x}\right)_y$ is specified at i = 1or I and $\left(\frac{\partial z}{\partial \eta}\right)_x$ is obtained from the previous spline fit $z(\eta)$ at x = const. using the relation

$$\left(\frac{\partial z}{\partial \eta}\right)_{x_{i,k}} = M_{\eta_{i,k}} \frac{\Delta\eta_k}{2} + \left(\frac{z_{i,k} - z_{i,k-1}}{\Delta\eta_k}\right) - (M_{\eta_{i,k}} - M_{\eta_{i,k-1}}) \frac{\Delta\eta_k}{6} \tag{14}$$

where $\Delta\eta_k = \eta_k - \eta_{k-1}$

If a ratio of second derivatives was stipulated at the end points, it is assumed not to change in the transformation.

(2) We obtain the coefficients $M_{x_{i,k}}$ employing the methods outlined in Section II where

$$M_{x_{i,k}} = \left(\frac{\partial^2 z}{\partial x^2}\right)_{\eta_{i,k}} \tag{15}$$

The techniques outlined for obtaining the coefficients $M_{\eta_{i,k}}$ and $M_{x_{i,k}}$ on an ordered i,k array are readily extended to surface fits in cylindrical coordinates where it is desired to approximate the surface

$$r = G(x,\theta) \tag{16}$$

Assuming that contour data is given in cartesian coordinates as data pairs of the form $(y_j, z_j)_i$ at discrete stations x_i as depicted in Figure (B5). We or course assume that the axis of the cylindrical system is parallel to the x axis of the cartesian system (the axis of the cylindrical system is given by $y = y^*$, $x = z^*$). Then, the input contour data is converted to cylindrical coordinates by the transformations

$$
\begin{aligned}
x &= x \\
r &= ((y-y^*)^2 + (z-z^*)^2)^{\frac{1}{2}} \\
\theta &= \tan^{-1}((z-z^*)/(y-y^*))
\end{aligned}
\tag{17}
$$

Then, we perform the transformation

$$
\begin{aligned}
x &= x \\
\eta &= (\theta-\theta_{A(x)})/(\theta_{B(x)}-\theta_{A(x)}) \\
r &= r
\end{aligned}
\tag{18}
$$

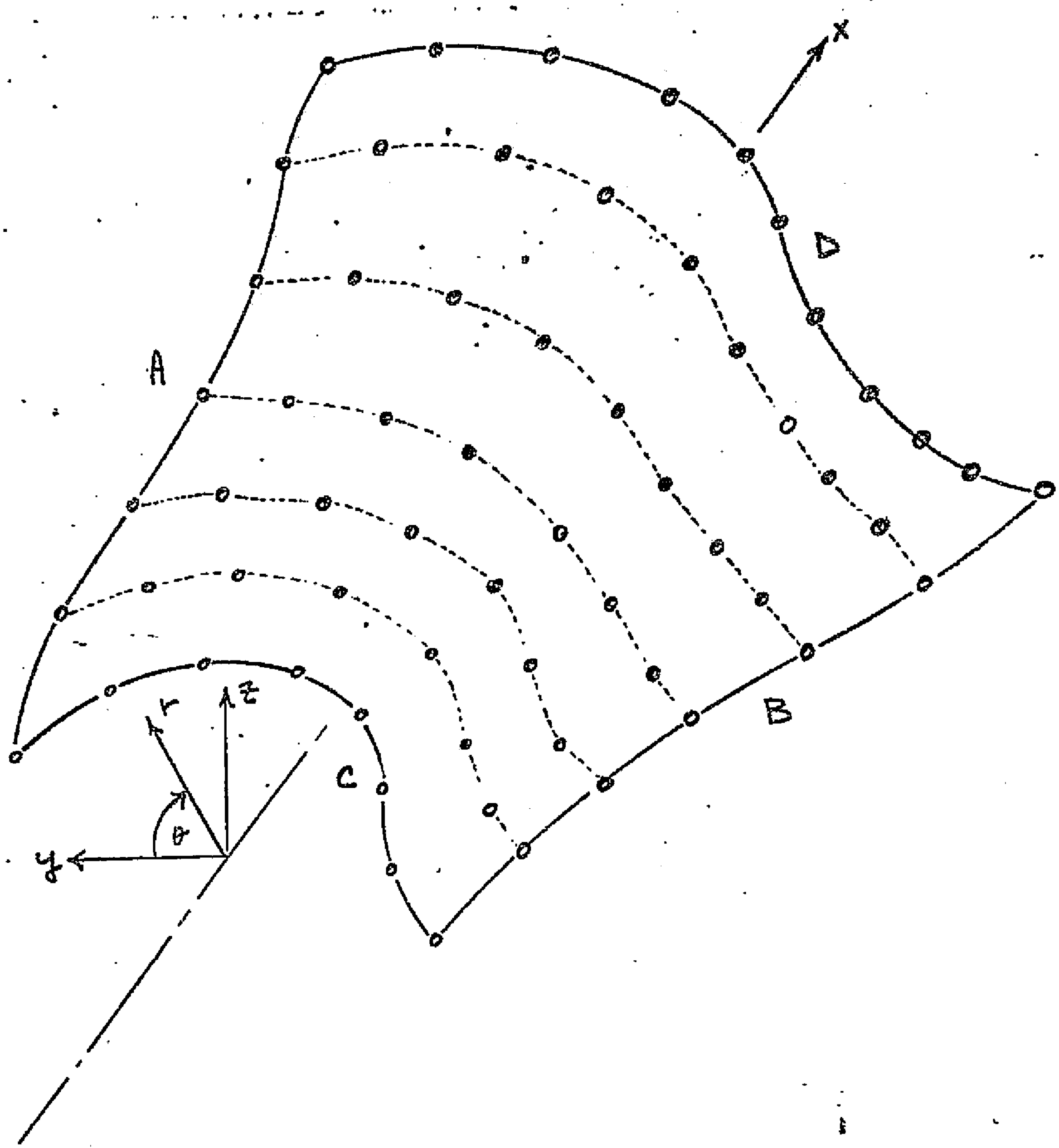

FIGURE B5. SURFACE REPRESENTATION IN CYLINDRICAL COORDINATES

Referring to Figure (4), the surface $z = F(x,y)$ is numerically represented by the arrays $z_{i,k}$, $M_{\eta_{i,k}}$, $M_{x_{i,k}}$, x_i, η_k for $i = 1,2$ --, 1 and $k = 1,2,$ ——, K as well as the arrays Y_{A_i}, Y_{B_i}, M_{A_i}, M_{B_i} for $i = 1,2$ —— -, 1. The arrays are determined by the procedure outlined in Section III. Now we are given arrays and values of the independent variables x and y and seek to determine the independent variable z as well as the partial first derivatives $(zk)_y$ and $(zy)_x$, which suffice in determining the surface unit normal. The details of this procedure are as follows:

(a) Determine $Y_{A(x)}$, $Y_{B(x)}$, $Y'_{A(x)}$, $Y'_{B(x)}$ employing the relations

$$
\begin{aligned}
Y_{\substack{A\\B}}(x) = {} & M_{\substack{A\\B}i-1} \frac{(x_i - x)^3}{6\Delta x_i} + M_{\substack{A\\B}i} \frac{(x - x_{i-1})^3}{6\Delta x_i} \\
& + \left(Y_{\substack{A\\B}i} - M_{\substack{A\\B}i} \frac{\Delta x_i^3}{6}\right)\left(\frac{x - x_{i-1}}{\Delta x_i}\right) \\
& + \left(Y_{\substack{A\\B}i-1} - M_{\substack{A\\B}i-1} \frac{\Delta x_i^2}{6}\right)\left(\frac{x_i - x}{\Delta x_i}\right)
\end{aligned}
\tag{19}
$$

and

$$
\begin{aligned}
Y_{\substack{A\\B}}(x) = {} & - M_{\substack{A\\B}i-1} \frac{(x_i - x)^2}{2\Delta x_i} + M_{\substack{A\\B}i} \frac{(x - x_{i-1})^2}{2\Delta x_i} \\
& + \left(Y_{\substack{A\\B}i} \; Y_{\substack{A\\B}i-1}\right) \frac{1}{\Delta x_i} - \left(M_{\substack{A\\B}i} - M_{\substack{A\\B}i-1}\right) \frac{\Delta x_i}{6}
\end{aligned}
\tag{20}
$$

where $x_{i-1} \leq x \leq x_i$ and $\Delta x_i = x_i - x_{i-1}$

(b) Evaluate $\eta(x,y)$ employing Equation (6).

(c) Ascertain the local grid in which the point x,η falls

$$
\begin{aligned}
&x_{i-1} \leq x \leq x_i \\
&\eta_{k-1} \leq \eta \leq \eta_k
\end{aligned}
\tag{21}
$$

as depicted in Figure (B6).

(d) Determine z_a, $(z_{\eta\eta})_a x$; z_b, $(z_{\eta\eta})_b x$;
z_c, $(z_{xx})_c \eta$; z_d, $(z_{xx})_d \eta$

employing the relations:

$$
\begin{aligned}
z_{\substack{a\\b}} = {} & M_{x_{i-1},\, \substack{k-1\\k}} \frac{(x_i - x)^3}{6\Delta x_i} + M_{x_i,\, \substack{k-1\\k}} \frac{(x - x_{i-1})^3}{6\Delta x_i} \\
& + \left(z_{i-1,\, \substack{k-1\\k}} - M_{x_{i-1},\, \substack{k-1\\k}} \frac{\Delta x_i^2}{6} \right) \frac{(x_i - x)}{\Delta x_i} \\
& + \left(z_{i,\, \substack{k-1\\k}} - M_{x_i,\, \substack{k-1\\k}} \frac{\Delta x_i^2}{6} \right) \frac{(x - x_{i-1})}{\Delta x_i}
\end{aligned}
\tag{22}
$$

$$
\begin{aligned}
z_{\substack{c\\d}} = {} & M_{\eta_{\substack{i-1\\i},\, k-1}} \frac{(\eta_k - \eta)^3}{6\Delta\eta_k} + M_{\eta_{\substack{i-1\\i},\, k}} \frac{(\eta - \eta_{k-1})^3}{6\Delta\eta_k} \\
& + \left(z_{\substack{i-1\\i},\, k} - M_{\eta_{\substack{i-1\\i},\, k-1}} \frac{\Delta\eta_k^2}{6} \right) \frac{(\eta_k - \eta)}{\Delta\eta_k} \\
& + \left(z_{\substack{i-1\\i},\, k} - M_{\eta_{\substack{i-1\\i},\, k}} \frac{\Delta\eta_k^2}{6} \right) \frac{(\eta - \eta_{k-1})}{\Delta\eta_k}
\end{aligned}
\tag{23}
$$

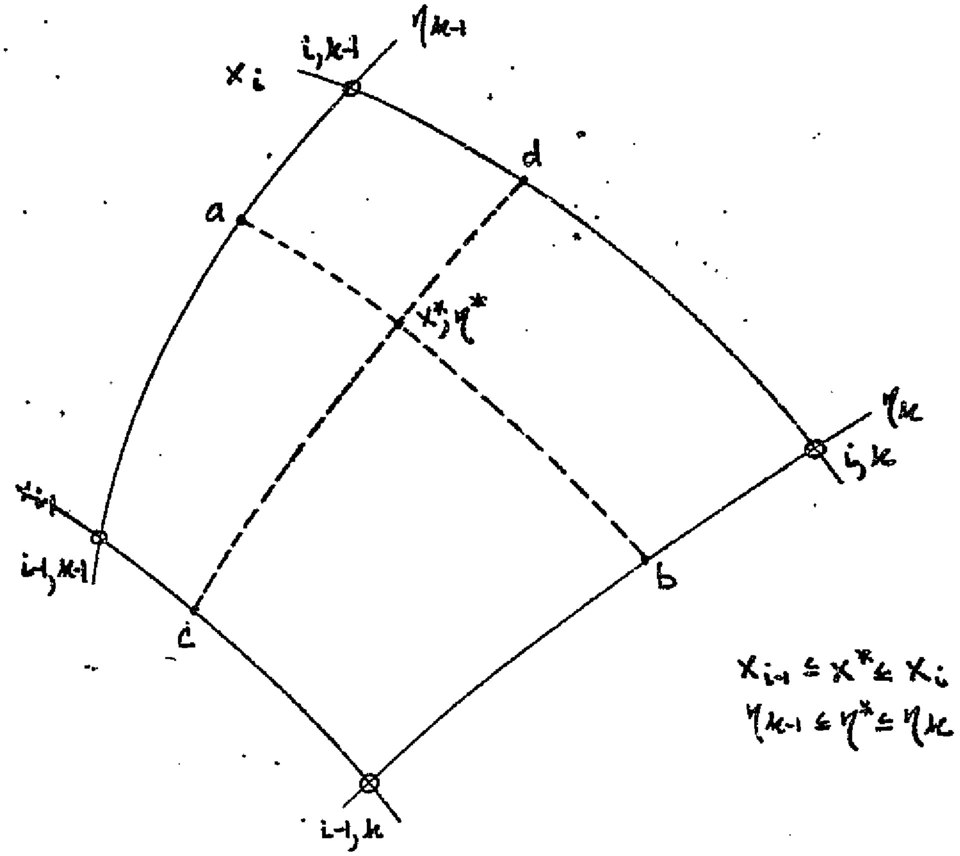

$$x_{i-1} \leq x^* \leq x_i$$

$$\eta_{k-1} \leq \eta^* \leq \eta_k$$

FIGURE B6. LOCAL GRID FOR INTERPOLATION

$$(z_{\eta\eta})_{\substack{a\\b \\ x=\text{const}}} = M_{\eta_{i-1,\ \substack{k-1\\k}}} \frac{(x_i - x)}{\Delta x_i} + M_{\eta_{i,\ \substack{k-1\\k}}} \frac{(x - x_{i-1})}{\Delta x_i} \tag{24}$$

$$(z_{xx})_{\substack{c\\d \\ \eta=\text{const}}} = M_{x_{\substack{i-1\\i},\ k-1}} \frac{(\eta_k - \eta)}{\Delta \eta_k} + M_{x_{\substack{i-1\\i},\ k}} \frac{(\eta - \eta_{k-1})}{\Delta \eta_k} \tag{25}$$

where $\Delta x_i = x_i - x_{i-1}$

$\Delta \eta_k = \eta_k - \eta_{k-1}$

(e) Determine $z(x,y)$

$$\begin{aligned}
z(x,y) = \frac{1}{2} \Bigg[& z_{\eta\eta_a} \frac{(\eta_k - \eta)^3}{6\Delta\eta_k} + z_{\eta\eta_b} \frac{(\eta - \eta_{k-1})}{6\Delta\eta_k} \\
& + \left(z_a - z_{\eta\eta_a} \frac{\Delta\eta_k^2}{6}\right) \frac{(\eta_k - \eta)}{\Delta\eta_k} \\
& + \left(z_b - z_{\eta\eta_b} \frac{\Delta\eta_k^2}{6}\right) \frac{(\eta - \eta_{k-1})}{\Delta\eta_k} \Bigg] \\
+ \frac{1}{2} \Bigg[& z_{xx_c} \frac{(x_i - x)^3}{6\Delta x_i} + z_{xx_d} \frac{(x - x_i)^3}{6\Delta x_i} \\
& + \left(z_c - z_{xx_c} \frac{\Delta x_i^2}{6}\right) \frac{(x_i - x)}{\Delta x_i} \\
& + \left(z_d - z_{xx_d} \frac{\Delta x_i^2}{6}\right) \frac{(x - x_{i-1})}{\Delta x_i} \Bigg]
\end{aligned} \tag{26}$$

ORIGINAL PAGE IS
OF POOR QUALITY

(f) Determine (z_η)

$$(z_\eta)_x = - z_{\eta\eta_a} \frac{(\eta_k - \eta)^2}{2\Delta\eta_k} + z_{\eta\eta_b} \frac{(\eta - \eta_{k-1})^2}{2\Delta\eta_k} + \frac{(z_b - z_a)}{\Delta\eta_k} - (z_{\eta\eta_b} - z_{\eta\eta_a}) \frac{\Delta\eta_k}{6} \tag{27}$$

(g) Determine $(z_x)_\eta$

$$(z_x)_\eta = - z_{xx_c} \frac{(x_i - x)^2}{2\Delta x_i} + z_{xx_d} \frac{(x - x_{i-1})}{2\Delta x_i} + \frac{(z_d - z_c)}{\Delta x_i} - (z_{xx_d} - z_{xx_c}) \frac{\Delta x_i}{6} \tag{28}$$

(h) Determine $(z_y)_x$

$$(z_y)_x = (z_\eta)_x / (y_{B(x)} - y_{A(x)}) \tag{29}$$

(i) Determine $(z_x)_y$

$$(z_x)_y = (z_x)_\eta - (z_y)_x \left[(1-\eta) y'_{A(x)} + \eta y'_{B(x)} \right] \tag{30}$$